Università degli studi di Bologna

Studies of the atmospheric muon flux with the ANTARES detector

Author: **Marco Bazzotti**

Advisor:

Prof. Maurizio Spurio

PhD Coordinator:

Prof. Fabio Ortolani

Bologna, Marzo 2009

Contents

CONTENTS

List of Figures

List of Tables

LIST OF TABLES

Introduction

The Cosmic Rays (CRs) are mainly high energy protons and heavier nuclei accelerated by astrophysical Galactic and extraGalactic objects. Although they come directly from the astrophysical objects of interes, it is impossible to point back to their source position in the sky because they are deflected from the galactic and extragalactic magnetic fields. Also neutral cosmic messengers have some limitations: neutrons decays after they can travel long distances while γ-ray photons interact with the electromagnetic background light limiting their travel.

In this scenario, neutrino seems to be a very interesting particle in order to study the astrophysical phenomena: it does not suffer deflection from magnetic fields cause it is neutral, it is a stable particle and it interacts only weakly.

The Cherenkov neutrino telescopes are composed by a matrix of light detectors placed inside a trasparent medium, as sea water or ice. The detection principle is based on the reconstruction of the neutrino track direction using the Cherenkov light emitted by charged particles, created by neutrino interactions. Muons produced by charge current interactions are of particular interest because the muon is the charged lepton with the longest range and it retains almost the same direction of the neutrino.

The largest backgroud source for the cosmic neutrino detection is represented by *atmospheric muons*, particles created mainly as a consequence of the decay of mesons π and K originated by the interaction of CRs with atmospheric nuclei. Although the neutrino telescopes 'look downward' in order to reject signals due to downward going atmospheric muons, they represent the most abundant signal in a Cherenkov telescope due to their high flux. They can represent a background source because they can be wrongly reconstructed as upward going particles mimicking muons from neutrino interactions. On the other hand they can be used to calibrate the detector and to check the validity of Monte Carlo simulation programs to the passage of charged particles. In

this scenario it is very important for any Cherenkov neutrino telescopes the knowledge of the underwater μ intensity in order to understand the detector response and possible systematic effects.

The aim of the thesis is the computation of the vertical component of the atmospheric muon flux as a function of the sea depth (also referred to as "Depth Intensity Relation", DIR) at the ANTARES site. ANTARES (*Astronomy with a Neutrino Telescope and Abyss environmental RESearch*) is at present the largest Cherenkov neutrino observatory in the Northern hemisphere. It consists in an array of twelve independent and flexible lines made of mechanically resistant electro-optical cables placed into the Maditerranean Sea water. The detector is able to explore the Southern sky hemisphere, which represents the most interesting area of the sky due to the presence of the Galactic Centre, where neutrino source candidates are expected.

The experimental data of the ANTARES telescope in its five lines configuration are analysed.

The measurement of the zenith angle of the event, performed by a reconstruction algorithm, is one of the most important information of this analysis. In order to improve the purity of the analyzed data set, related to the zenith angle reconstruction, some parameters (referred to as "quality parameters") of the tracking program are used to perform a cut on the reconstructed events. The survived events are used in the DIR computation.

The following quantities, necessary for the DIR computation, are then calculated through MonteCarlo simulations:
- The errors in the zenith angle reconstruction obtained by the tracking algorithm before and after quality cuts on the data set.
- The fraction of reconstructed events with respect to the number of the MonteCarlo generated events crossing a cylindrical area containing the instrumented apparatus.
- The average multiplicity of muon bundles at a fixed sea depth ($h_0 = 1890\,m$).
These informations have been implemented into a deconvolution algorithm based on a Bayesian approach to finally obtain the experimental DIR.

The systematic errors are finally estimated taking into consideration the uncertainties on several input parameters required to define the environmental and geometrical characteristics of the detector in the MonteCarlo simulation: absorption lenght of sea water, PhotoMultiplayer tube efficiency and the effect of the cuts.

The thesis is organized in the following way.

- In chapter 1 an introduction to the physics of the CRs is given. The correlation between gamma ray and neutrino astronomy is then described and some potential astrophysical sources of high energy neutrinos are presented. The physics of neutrinos and the detection principle of Cherenkov neutrino telescopes is explained, with a summary of past and present Cherenkov neutrino telescopes.

- The chapter 2 contains the description of some primary cosmic ray (PCR) models which are used as first inputs in the MonteCarlo simulations of underwater atmospheric muons. Several characteristics of the underwater muons are then discussed giving particular interest to the multi-μ events. Finally the physics process of Cherenkov light generation by muons is explained.

- In chapter 3 a brief description of the ANTARES neutrino telescope is given followed by the description of the detector layout and of the site evaluation. In the last section the data acquisition system and the time and position calibration of the detector are explained.

- In chapter 4 the MonteCarlo production chain performed for the analysis is shown and each program is described. The real and MonteCarlo data samples considered in the analysis are then defined. Finally the tracking program used to infer some physics informations from the triggered events is presented.

- In chapter 5 a selection of the reconstructed events based on some requirements of the quality parameters of the reconstruction program is defined and motivated. This selection intends to choose a data subset with a higher purity, in particular concerning the reconstruction of the zenith angle which is needed in the analysis. Some quantities necessary to the unfolding algorithm are finally defined and calculated.

- The chapter 6 describes the deconvolution procedure used to get the physics quantities from the experimental data. The final results of the DIR and of the atmospheric muon flux at a fixed sea depth as a function of the zenith angle are given. Finally the systematic uncertainties are estimated.

Chapter 1

High energy neutrino astronomy and neutrino telescopes

The weakly interacting nature of neutrino and its neutral electric charge make this particle the cosmic messenger on which the astrophysics efforts will focuse. Its small interaction probability combined with the expected fluxes, require the use of a very large volume detector and long operation times. In addiction the volume must be transparent to the light propagation in order to collect the Cherenkov radiation emitted by products of neutrinos. Naturally abundant sea-water (or ice) can be used for such a purpose. The detection of the Cherenkov radiation is made possible using arrays of photomultiplayers deployed inside the sea-water (or ice). The so-called Cherenkov neutrino telescopes cover a neutrino energy detection range between $\simeq 10^{11} - 10^{15} eV$.

In this chapter a brief introduction to the physics of the CRs is given. The correlation between gamma ray and neutrino astronomy is shown and some potential astrophysical sources of high energy neutrinos are then discussed. In the next the physics of neutrinos and the detection principle of Cherenkov neutrino telescopes is briefly described. In the last section a summary of past and present Cherenkov neutrino telescopes is given.

1.1 Cosmic Rays

Cosmic Rays (CRs) are mainly high energy protons and heavier nuclei. The energy spectrum is of non-thermal origin and follows a broken power law of the form:

$$dN_P/dE = K \cdot E^{-\gamma} \tag{1.1}$$

1. HIGH ENERGY NEUTRINO ASTRONOMY AND NEUTRINO TELESCOPES

Figure 1.1 shows the CRs flux observed at Earth.

Up to energies of 10^{14} eV, the CRs spectrum can be directly detected above the atmosphere. Stratospheric balloons or satellites have provided the most relevant informations about the composition of CRs in the Galaxy and had contributed to establish the standard model of Galactic CRs. The measurements show that $\sim 90\%$ of CRs are protons, $\sim 9\%$ are Helium nuclei and $\sim 1\%$ are heavier nuclei (Figure 1.1).

Above $\sim 10^{14}$ eV, due to the low fluxes, more extensive detectors than ones implemented in stratospheric balloons or satellites, are needed in order to get a significant statistics. Measurements are therefore only accessible from ground detection infrastructures. The showers of secondary particles created by interaction of primary CR in the atmosphere are distributed in a large area, enough to be detected by detector arrays (scintillation counters or water tanks in which charged particles emit Cherenkov light).

The measured power-law spectrum of CRs (eq. 1.1) has an index $\gamma = 2.7$ up to roughly 3×10^{15} eV. Above that energy there is a variation in the spectral index. This feature is referred to as the *knee*. Most likely, the mechanism responsible for the acceleration of particles to high energies is the Fermi mechanism [1; 2]. It explains particle acceleration by the wandering back and forth between the two sides of a shock wave. This iterative process predicts a spectrum with a power-law dependence and a typical spectral index of about 2. Supernova remnants (SNRs) in the Galaxy are the most accredited site of acceleration for CRs up to the knee [3], although this theory is not free from some difficulties [4]. The measured spectral index ($\gamma \sim 2.7$) is steeper than the source spectrum, because of the energy dependence of the CRs diffusion out of the Galaxy, as for instance the so called *leaky box* [5]. According to this model, during propagation high energy particles have larger probability to escape from the Galaxy than particles with low energy at the same value of the electric charge Ze, due to their larger gyromagnetic radii. Taking into account this energy dependence, about the same measured spectral index ~ 2.7 is got back from the theory .

Above the *knee* the index becomes $\gamma = 3.1$. This feature of the CRs spectrum is still an open question and different models have been proposed to explain it [6]. Some models invoke astrophysical reasons: due to the iterative scattering processes involved in the acceleration sites, a maximum energy for the CRs is foreseen. This maximum energy linearly depends from the nucleus charge Ze, and this leads to the prediction
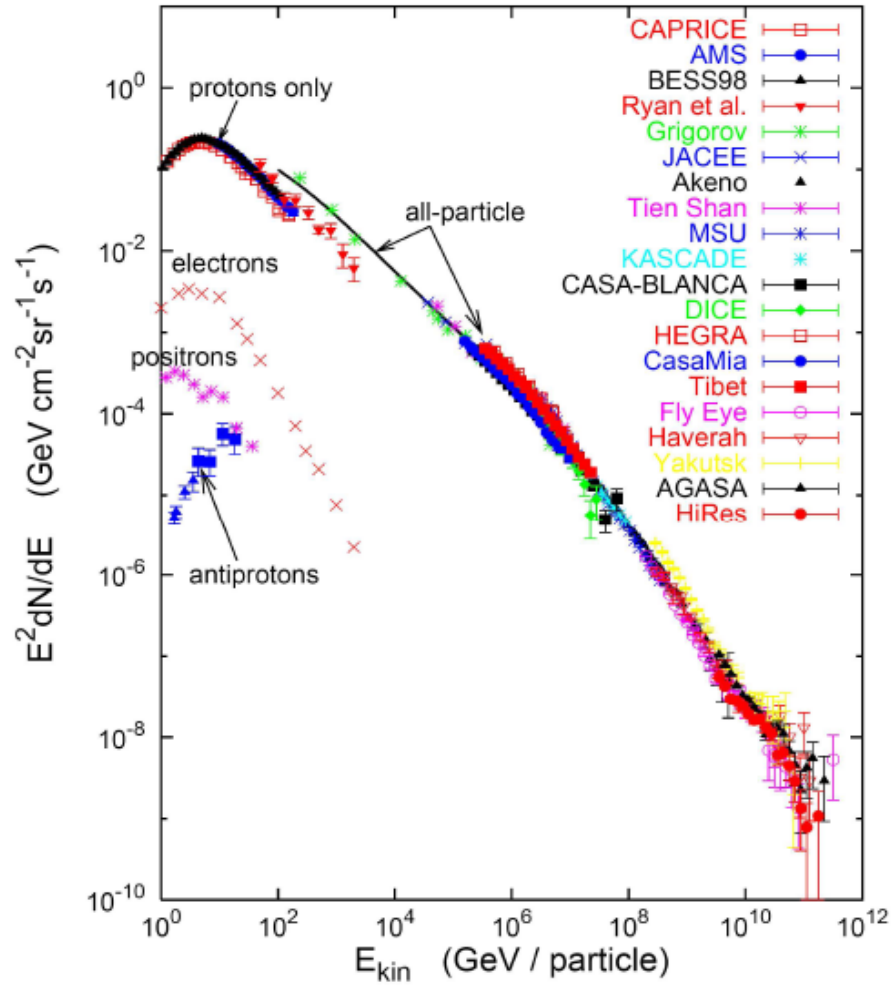
Figure 1.1: Cosmic Ray spectrum from 10^9 to 10^{21} eV as measured on Earth, from [7]. On the low-energy domain, when the measurements are available, it is reported the contribution of protons, electrons, positrons and antiprotons. Refer to [7] for the reference to the experiments.

of a cut-off to the energy spectra of every nucleus type. Hence the knee at 3 PeV follows from subsequent cut-offs for individual elements at energies $Z \times 3 \cdot 10^{15}$ eV. As a consequence, the CRs composition is expected proton-rich before, and iron-rich after the *knee*. Other models hypothesize new particle processes in the atmosphere [8] as responsible of the steepening in the CRs flux. There is no consensus on a preferred accelerator model for energies above the *knee* up to 10^{19} eV, where there is a flattening in the spectrum denoted as the *ankle*.

The flux above the *ankle*, still dominated by protons or nuclei [9], is one particle per kilometre square per year per stereoradian. It is from long time [10] assumed that such ultra high energy cosmic rays (UHECRs) have extragalactic origins. UHECRs can be detected only by very large ground-based installations [11], using grids with ~ 1 km spacing. At present, the largest experiments is the Auger Observatory [12] which combines the measurement of extensive air showers and the light fluorescence detection.

Looking for UHECRs sources, another effect has to be taken into account , the Greisen-Zatsepin-Kuzmin cutoff (GZK) [13; 14], which imposes a theoretical upper limit on the energy of cosmic rays from distant sources. Above a threshold of few 10^{19} eV, protons interact with the 2.7^o K cosmic microwave background radiation (CMB) and lose energy. Due to the GZK cutoff, protons above threshold cannot travel distances further than few tens of Mpc.

From the astrophysical point of view, this cut-off is very important because it limits the existence of UHECRs emitters to our local super-cluster of galaxies.

1.2 High energy photons and neutrinos

Charged particles are not good messengers because the influence they suffer from the galactic and extragalactic magnetic fields makes impossible to point back to their source position in the sky. Only UHECRs can be marginally influenced by magnetic fields but the GZK cutoff limits their travel distance to less than 100 Mpc. Better messengers are the electrically neutral particles such as photons or neutrinos. The neutral particles cannot be accelerated by any acceleration model and they are supposed to be the decay products of accelerated charged particles. Both electrons and protons can be accelerated by astrophysical objects. It is referred to as a *leptonic model* when electron are accelerated, and to an *hadronic model* when protons or other nuclei are accelerated.

Both models, the leptonic model and the hadronic model, should coexist [15]. While high energy photons can be produced both in leptonic (Inverse Compton process) and in hadronic models, neutrinos are emitted only in the hadronic acceleration.

Accelerated protons will interact in the surroundings of the CRs emitter with photons predominantly via the Δ^+ resonance:

$$p + \gamma \rightarrow \Delta^+ \rightarrow \pi^o + p$$
$$p + \gamma \rightarrow \Delta^+ \rightarrow \pi^+ + n \tag{1.2}$$

Protons will also interact with ambient matter (protons, neutrons and nuclei), giving rise to the production of charged and neutral mesons. The relationship between sources of γ-ray and neutrinos is the meson-decay channel. Neutral mesons decay in photons:

$$\pi^o \rightarrow \gamma\gamma \tag{1.3}$$

while charged mesons decay in neutrinos

$$\pi^+ \rightarrow \nu_\mu + \mu^+$$
$$\hookrightarrow \mu^+ \rightarrow \overline{\nu_\mu} + \nu_e + e^+$$
$$\pi^- \rightarrow \overline{\nu_\mu} + \mu^-$$
$$\hookrightarrow \mu^- \rightarrow \nu_\mu + \overline{\nu_e} + e^- \tag{1.4}$$

Candidates for neutrino sources are in general also γ-ray sources. The mechanisms that produce CRs produce also neutrinos and high-energy photons (from eq. 1.3,1.4) with power law energy spectra $E^{-\gamma}$ almost identical to the parent proton spectrum ($\gamma_{CR} \sim \gamma_\nu \sim \gamma_\gamma$) [16]. Hence the γ-ray from hadronic models have crucial information about the primary CR, and put constraints (see §1.4) to the expected neutrino flux from sources where γ-rays are observed.

This connection between CRs, neutrinos and γ-rays put upper bounds on the expected neutrino flux from extragalactic sources, since the neutrino energy generation rate will never exceed the generation rate of high energy protons.

1.3 Gamma Rays

Different processes occurring in the Universe would result in γ-ray emission, including CRs interactions with interstellar gas, supernova explosions, and interactions of energetic electrons with magnetic fields. As already mentioned γ-rays are not affected by

1. HIGH ENERGY NEUTRINO ASTRONOMY AND NEUTRINO TELESCOPES

magnetic fields and can act as messengers of distant cosmic events, allowing straight extrapolation to the source.

γ-rays up to 100 GeV are detectable directly from dedicated satellites outside the atmosphere. Photons in the MeV-GeV energy range were detected by the Energetic Gamma-ray Experiment Telescope (EGRET) [17] on board of the CGRO satellite in the 1990s and now from the Fermi satellite [18].

γ-rays above 100 GeV are only detectable in ground based apparatus, using a technique known as Imaging Air-Cherenkov Technique (IACT). These γ-rays are of particular interest, because the neutral pion decay (eq. 1.3) produces photons in this energy range.

During the past decade, several ground based γ-ray detectors were developed. The HEGRA experiment [19] has pioneered stereoscopic shower Imaging by Arrays of Cherenkov Telescopes. Other detectors are the VERITAS array [20] and the upgrade of the existing CANGAROO array [21]. At present, the two new generation ground based IACTs telescopes are the HESS telescope array [22] and the MAGIC telescope [23].

The HESS instrument is an array of 4 telescopes each one with twelve-metre diameter. Each instrument combines the stereoscopic imaging with large light collectors and highly segmented detectors with a wide field of view. The HESS telescope has been operational since 2004.

The MAGIC telescope is a seventeen-metre telescope which uses photon detectors with enhanced quantum efficiency, and image timing information. One of the particular features of MAGIC is the fast positioning to a source when alerted by a γ-ray burst trigger from satellite detectors. MAGIC started to take data in 2004. A second telescope is being built.

However high energy γ-rays (> 10 GeV) interact with the infra-red, microwave and radio background photons. As a consequence the mean free path travelled by photons is limited. This effect is shown in figure 1.2 in which you can see the absorption lenght as a function of the energy. In particular, above 10 TeV the horizon of the photons is limited to less than 10 Mpc, much less that the horizon of UHECRs. Only neutrinos can tell us something about the extreme regions of the Universe, as it is discussed in the next section.
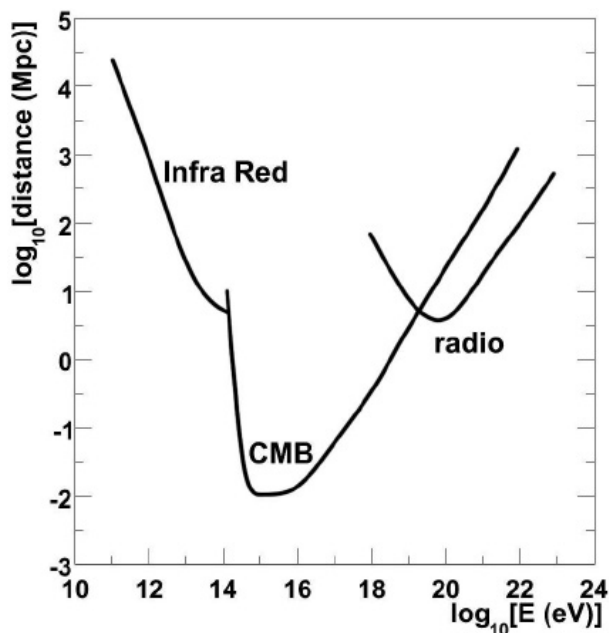
Figure 1.2: Absorption length of photons as a function of their energy.

1.4 Neutrino sources

Neutrinos are probably the best candidates in order to enhance our knowledge of the Universe. Neutrinos are not affected by any magnetic field, they are stable and they interact only weakly so they can travel very long distances coming also from very dense objects. In this section, some potential astrophysical sources of high energy neutrinos are discussed.

1.4.1 Galactic neutrinos

Sources of the CRs for energies up to the *ankle* are supposed to be galactic. These sources can be very interesting for a neutrino telescope. Their main advantage, with respect to the extra-Galactic ones, is their relatively close distance to the Earth (~ 10 kpc). In order to produce the same detectable event rate, an extra-Galactic source is required to have a luminosity orders of magnitude greater than a Galactic source. A list of the most promising Galactic sources of neutrino are presented in the following. Some of them are almost guaranteed neutrino sources in the light of the recent results from γ-ray telescopes, although their neutrino fluxes are uncertain.

1.4.1.1 Supernova remnants (SNR)

A supernova (SN) is a luminous explosion due to the core collapse of a massive star. As a result an expanding shock wave consisting of ejected as well as swept up interstellar matter is created that envelops the supernova remnant. At this shock wave, particle acceleration can occur via Fermi mechanism. If the final product of the SN is a neutron star, already accelerated particles can gain additional energy due to its strong magnetic fields. SNRs are considered to be the most likely sites of Galactic CRs acceleration, supported by recent observations from the γ-ray IACT.

Of particular interest is the supernova remnant in the Vela Jr. (RX J0852.0-4622). This SNR is one of the brightest objects in the southern TeV sky. From some calculations [24], the expected neutrino-induced muon rate leads to encouraging result for a Mediterranean detector.

1.4.1.2 Pulsar wind nebulae (PWNe)

A PWN is a nebula believed to be powered by a relativistic wind of particles and magnetic fields from a pulsar, which blows out jets of very fast-moving material into the nebula. The radio, optical and X-ray observations suggest a synchrotron origin for these emissions. The HESS telescope [22] has also detected TeV γ-ray emission from the Vela PWN, named Vela X, claiming that this emission is likely produced by the inverse Compton mechanism, but the possibility of an hadronic origin for the observed γ-ray spectrum, with the consequent flux of neutrinos, was also considered [25].

Neutrino fluxes have been calculated in [26] (considering hadronic production) for a few PWNe observed in TeV γ-rays (such as the Crab, the Vela X, the PWN around PSR1706-44 and the nebula surrounding PSR1509-58) with the conclusion that all these PWNe could be detected by a kilometre-scale neutrino telescope.

1.4.1.3 Microquasars

Microquasars are galactic X-ray binary systems composed of an accreting massive object such as a black hole or a neutron star and a companion star which provides mass to the firs one. They display relativistic radio-emitting jets, probably fed by the accretion of matter from the companion star. Microquasar resemble AGN (see §1.4.2.1), but at a much smaller scale.

The best candidates as neutrino sources are the steady microquasars SS433 and GX339-4. Assuming reasonable scenarios for TeV neutrino production, a 1 km^3-scale neutrino telescope in the Mediterranean sea could identify microquasars in a few years of data taking, with the possibility of a 5σ level detection. In case of no-observation, it would strongly constrain the neutrino production models and the source parameters.

1.4.1.4   Neutrinos from Galactic Centre (GC)

GC is specially appealing for a Mediterranean neutrino telescope since it is within the sky view of a telescope located at such latitude.

Early HESS observations of the GC region detected a point-like source at the gravitational centre of the Galaxy (HESS J1745-290 [27]) coincident with the supermassive black hole Sagittarius A* and the SNR Sgr A East. In 2004, a more sensitive campaign revealed a second source, the PWN G 0.9+0.1 [28].

The measured γ-ray spectrum in the GC region is well described by a power law with index of ~ 2.3. The photon index of the γ-rays, which closely traces back the spectral index of the CRs, indicates in the Galactic centre a local CRs spectrum that is much harder and denser than that as measured at Earth.

It is thus likely that an additional component to the CRs population is present in the Galactic Centre, above the diffuse CRs concentration which fills the whole Galaxy.

1.4.2   Extra-Galactic neutrinos

The measured CRs spectrum above the *ankle* is assumed to be the consequence of the contribution of some extra-Galactic source. Therefore if hadronic particles (protons or any other nucleus) are accelerated by extra-Galactic objects, it's reasonable to think that also a neutrino flux is created in such environment.

There is an upper bound to the expected neutrino flux coming from optical thin sources, the so-called Waxman-Bahcall limit (WB). Although this limit may be surpassed by hidden or optically thick sources for protons to $p\gamma$ or $pp(n)$ interactions as it will be described in the next, it is a reasonable limit to the predicted neutrino flux coming from different extra-Galactic sources of UHECRs.

The most plausible sources of UHECRs are Active Galactic Nuclei (AGN) and γ-ray bursts (GRBs). In this section the two astrophysical objects are reviewed togheter with a brief overview to the *hidden* CR source.

1. HIGH ENERGY NEUTRINO ASTRONOMY AND NEUTRINO TELESCOPES

In addiction to these high energy neutrino sources, there are high energy neutrinos induced by the interaction of UHECRs with photons belonging to the CMB. This produces the GZK cut-off already mentioned. The subsequent pion decay will produce a neutrino flux similar to the WB bound above 5×10^{18} eV [29], since neutrinos approximately carry 5% of the proton energy.

Anyway these sources are very far and the possibility of a individual discovery in a km^3 scale neutrino telescope is expected only in particular theoretical models.

An alternative way to prove the existence of extragalactic neutrino sources is through the measurement of the *cumulative flux* from unresolved cosmic sources in the whole sky. Since there is no directional information, the only way to detect this *diffuse flux of high energy neutrinos* is looking for an excess of high energy events in the energy spectrum over the background of the atmospheric neutrinos (neutrinos produced by interactions of cosmic rays with the Earth's atmosphere).

1.4.2.1 Active Galactic Nuclei (AGN)

Active Galactic Nuclei are the brightest sources in the Universe. In the standard model of AGN, a very massive black hole ($10^6 \div 10^9$ solar masses) accretes matter (several solar masses a year). Typically, two jets are observed, emerging at opposite sides of the accretion disc. In these jets particles can be accelerated. These particle beams can interact with the ambient matter and photons. An AGN appears especially bright when one of the jets is oriented along our line of sight. In this case the AGN is called *blazar* and it represents the best chance to be detected as individual point sources of neutrinos because a significant flux enhancement in the jet.

Blazars exhibit non-thermal continuum emission from radio to VHE frequencies and are highly variable, with fluxes varying by factors of around 10 over timescales from less than 1 hour to months.

66 blazars have been detected by EGRET and an increasing population of TeV blazars at higher redshifts is being detected by the latest generation of γ-ray IACT; currently 18 blazars have been discovered over a range of red-shifts from 0.03 to >0.2.

An important effect to take into account is that the observed γ-ray spectrum from extragalactic sources is steepened due to absorption by the Extragalactic Background Light (EBL). Neutrinos, however, are unaffected by the EBL and in the case of a distant blazar, such as 1ES1101 at z=0.186, the observed spectral index of 3 is estimated to

correspond to an intrinsic spectral index as hard as 1.5 [30]. Because of this hardening, the most distant TeV-bright blazars are expected to produce ν_μ fluxes exceeding the atmospheric neutrino background in a cubic kilometre neutrino telescope [31].

1.4.2.2 Gamma ray bursts (GRBs)

Gamma ray bursts are very bright flashes of MeV gamma rays, lasting from less than a second to a few hundred seconds. GRBs also produce X-ray, optical and radio emission subsequent to the initial gamma burst (the so called *afterglow* of the GRB).

Various models are proposed. The likely origin of GRBs with duration of tens of seconds ('long' bursts) is the collapse of massive stars, or supernovae, to a black hole [32; 33; 34]. This assumes that a *fireball* expanding with a highly relativistic velocity (Lorentz factor $\Gamma \sim 10^{2.5}$) is produced in the collapse, powered by radiation pressure. Protons accelerated in the fireball internal shocks lose energy through photo-meson interaction with ambient photons (the same process of eq. 1.2). The interaction rate between photons and protons is highly due to the high density of ambient photons and yields a significant production of pions, which decade in neutrinos carrying typically 5% of the proton energy. Hence, neutrinos with $E_\nu \sim 10^{14}$ eV are expected [35]. Other neutrinos with lower energies can also be produced in different regions or stages where GRB γ-rays are originated. Depending on models, a different contribution of neutrinos is expected at every time stage of the GRB.

Being transient sources, GRBs detection has the advantage to be practically background free, since neutrino events coming from GRB are correlated both in time and direction with γ-rays. Some calculations of the neutrino flux [36] from GRB show that a kilometre-scale neutrino telescope can be sufficient to detect it. The average energy of these neutrinos (100 TeV) corresponds to a value for which neutrino telescopes are highly efficient.

1.4.2.3 Starburst or neutrino factory

As already mentioned, the WB bound is computed assuming that CRs sources are optically thin for protons. Radio observations of starburst galaxies have suggested the possibile existence of regions of space with an abnormally high rate of star formation. Supernovae explosions are expected to enrich the dense star forming region with relativistic protons and electrons [37; 38] which would lose energy through pion production.

Part of the proton energy will, therefore, be converted into neutrinos by charged meson decays. Starbursts are considered *hidden* CRs sources or purely-neutrino accelerators since only neutrinos can escape from this dense region. A cumulative flux of GeV neutrinos from starburst galaxies was calculated in [39] as $E_\nu^2 \Phi_\nu \simeq 10^{-7}\,GeV\,cm^{-2}s^{-1}sr^{-1}$, a value which is potentially detectable by a km^3-scale neutrino detector.

1.5   Neutrino oscillations

Neutrino oscillations are a well known phenomenon that will affect the cosmic neutrino flux. Neutrino oscillations were observed in atmospheric neutrinos, in solar neutrino experiments and on Earth based accelerator and reactor experiments. A complete review about neutrino oscillations can be found in [40].

As already mentioned, high energy neutrinos are believed to be produced in astrophysical sources mainly through the decay of charged pions coming out from $p\gamma$, pp, pn interactions (eq. 1.4). Therefore, neutrino fluxes of the different flavours are expected to be at the source in the ratio:

$$\nu_e : \nu_\mu : \nu_\tau = 1\ :\ 2\ :\ 0 \tag{1.5}$$

Neutrino oscillations will induce flavour changes while neutrinos propagate through the Universe. According to neutrino oscillations parameters, the ratio of the fluxes of neutrinos changes to an observed flux ratio at Earth as

$$\nu_e : \nu_\mu : \nu_\tau = 1\ :\ 1\ :\ 1 \tag{1.6}$$

1.6   Neutrino detection principle

The idea of a cherenkov neutrino telescope based on the detection of the secondary particles produced in neutrino interactions was formulated in the 1960s by Markov [41]. The basic idea is to build a matrix of light detectors inside a transparent medium. This medium, as deep ice or water:

- offers a large volume of free target for neutrino interactions;

- provides a shield against the secondary particles produced by CRs;

- allows the transmission of Cherenkov photons emitted by relativistic particles produced by the neutrino interaction.
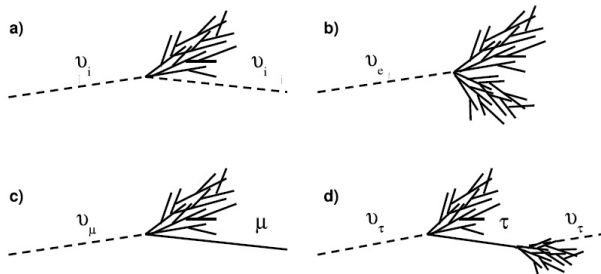
Figure 1.3: Event signature topologies for different neutrino flavours and interactions. a) NC interaction producing a hadronic shower; b) CC interaction of ν_e producing both an EM and a hadronic shower; c) CC interaction of ν_μ producing a μ and a hadronic shower; d) CC interaction of ν_τ producing a τ that decays into a ν_τ tracing the double bang event signature. Particles and anti-particles cannot be distinguish in neutrino telescopes.

The principles of the Cherenkov emission are described in §2.6.

1.6.1 Neutrino interactions

Neutrinos are neutral weakly interacting particles. At high energies the interaction with matter is dominated by the inelastic scattering of the neutrino with a target nucleon (N). This interaction can be due to the exchange of the bosons $W^\pm$ via the so called charged current (CC) weak interaction:

$$\nu_l + N \rightarrow l + X \tag{1.7}$$

or to the exchange of the neutral boson Z^0 via the so called neutral current (NC) weak interaction:

$$\nu_l + N \rightarrow \nu_l + X \tag{1.8}$$

Neutrinos can be detected when the particles released by neutrino interactions with nucleons, induce Cherenkov radiation when crossing at relativistic velocities a suitable optical medium such as ice or water. The experimental signal consists in measuring the intensity and the arrival time of the Cherenkov photons on a three-dimensional array of PhotoMultiplier Tubes (PMTs). From that some informations about the properties of the neutrino (flavour, direction, energy, kind of reaction) can be inferred (see Figure 1.3).

The most common neutrino detection is due to the CC ν_μ interactions. The muon (μ) is the charged lepton with the longest range and it can be detected also if it is created outside the instrumented volume. The muon energy loss is treated in §2.4.
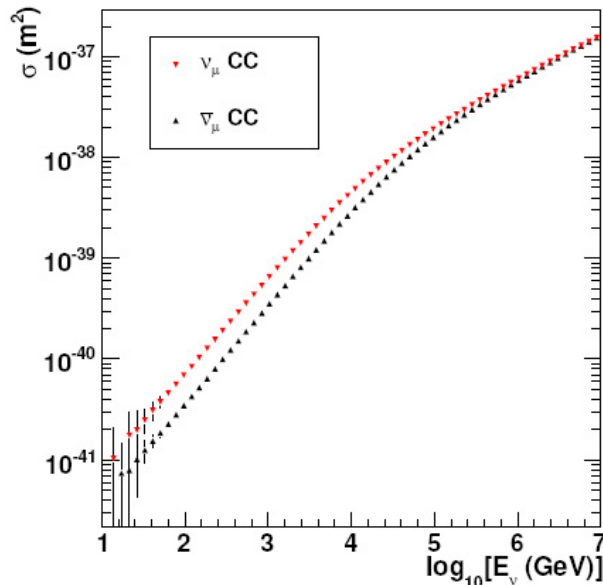
Figure 1.4: Cross section for ν_μ and $\overline{\nu_\mu}$ as a function of the neutrino energy according to CTEQ6-DIS [42] parton distributions.

The remaining CC interactions are more difficult to detect due to the shorter range of the consequent leptons. Electron produces an electromagnetic shower which propagates for few meters while τ-lepton travels some distance (depending on its energy) before it decays and produces a second shower. The Cherenkov light emitted by the charged particles in the shower can be detected only if the interaction occurs inside the instrumented volume of the detector.

In the following only muon neutrinos are discussed, which are especially interesting in searching for point sources in the energy range between ~ 100 GeV and 10^6 GeV.

At such energies the muon neutrinos interactions are deep inelastic and a large fraction of the neutrino energy goes into the hadronic shower. Figure 1.4 shows the ν_μ and $\overline{\nu}_\mu$ cross sections as a function of the neutrino energy.

The muon created in a muon neutrino interaction retains almost the same direction of the neutrino. Naming $(\theta_{\nu-\mu})$ the angle between the incident neutrino and the outgoing muon, the upper limit on this angle can be approximated by:

$$\langle \theta_{\nu-\mu} \rangle \leq \frac{1.5^o}{\sqrt{E_\nu (TeV)}} \tag{1.9}$$

where E_ν is the neutrino energy. It's clear from this formula that high energy muons

have almost the same direction of their parent neutrinos. In addiction the deviation due to the multiple scattering, to which a muon traveling through water or ice is subjected, at the energies and distances considered is smaller than that in eq. 1.9 [43]. As neutrinos are not deflected by (extra-)galactic magnetic fileds, it is possible to trace the muon back to the neutrino origin. This justifies the name *telescope* applied to this kind of detector.

1.6.2 Physical background

Air showers induced by interactions of cosmic rays with the Earth's atmosphere produce the so-called *atmospheric muons* and *atmospheric neutrinos*. Neutrino detectors must be located deeply into the sea-water or ice in order to be shielded by this background. The atmospheric muon physics will be explained in the next chapter. In Figure 1.5 you can see that the flux of down-going atmospheric muons exceeds the flux of muons induced by atmospheric neutrino interactions by many orders of magnitude, decreasing with increasing detector depth.

In order to reject signals due to down-ward atmospheric muons the neutrino telescopes, at the contrary of usual optical telescopes, 'look down-ward'. From the bottom hemisphere, the neutrino signal is almost background-free. Infact up-going muons can only be produced by interactions of (up-going) neutrinos that have traversed the Earth. Only atmospheric neutrinos represent the irreducible background for the study of cosmic neutrinos, which can be selected through dedicated cuts during the data analysis.

1.7 Past and present neutrino telescopes

The idea to use sea-water or ice as a medium in which to detect muons coming from high enegy neutrinos was first discussed about 50 years ago [44]. By that time several experiments have attempted to use that idea. The general detection principle is the same for any experiment but the experimental challenges in each case are different. In this section a brief outlook to the past, present and future Cherenkov neutrino telescopes is given. ANTARES will be reviewed in detail in the next chapter.
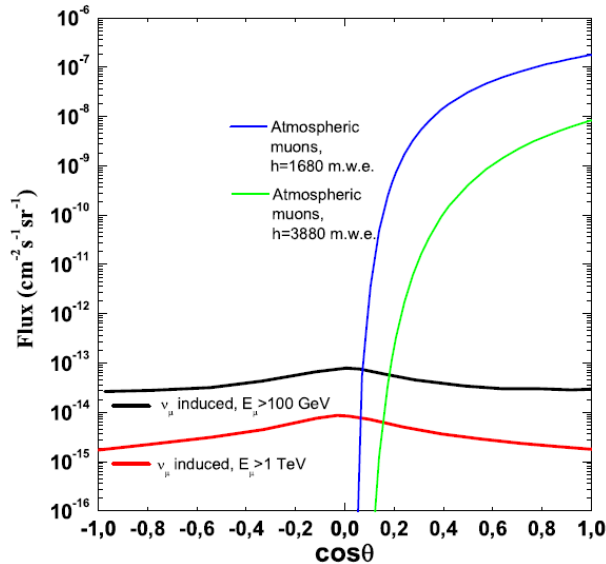
Figure 1.5: Different contributions to muon background as a function of the zenith angle. Atmospheric muons are from MUPAGE program (see §4.2) and atmospheric neutrino induced muons are from calculations by Bartol [45]. The solid lines stand for $E_\mu > 1$ TeV and the dashed lines for $E_\mu > 100$ GeV.

1.7.1 DUMAND

The DUMAND (Deep Underwater Muon And Neutrino Detector) experiment [46] was the first attempt to build an underwater neutrino telescope. It had been deployed in the Pacific Ocean near the Hawaii islands at a depth of 4800 m. Although The project was cancelled in 1996 for technical problems and lack of money, a great deal of experience gained in terms of site exploration, detector construction and deployment and simulation had passed to the next generation of experiments.

1.7.2 Baikal (NT-200)

The Baikal neutrino telescope (deployed in Lake Baikal in Siberia) has been the first detector showing the possibility to performe astronomy with an underwater neutrino telescope. Its performance is limited by the maximum depth at which it is deployed, about 1300 m, which doesn't shield so well the detector from the very high atmospheric neutrino fluxes (see Figure 1.5). In addiction the optical properties of the Baikal water are worse than those of the sea water. In winter the surface of the lake freezes, giving the advantage, over the deep sea site, that the detector can be deployed from a solid

surface.

The Baikal experiment has been running since 1993, and in 2005 it was expanded in a configuration known as the NT-200+ stage [47; 48] (192 photomultiplier at eight strings and 36 additional photomultipliers in three separated strings).

1.7.3 AMANDA and IceCube

The AMANDA [49; 50] experiment (Antarctic Muon And Neutrino Detector Array) is an array of PMTs embedded in the antarctic ice at a depth of about 2 km. Using the ice as the Cherenkov medium has some advantages and some disadvantages. Ice at a depth of several kilometers below the surface of the South Pole, has much longer absorption lenght with respect to the water of the deep ocean. A good consequence is that the individual PMTs can be placed further apart to detect the same amount of Cherenkov light and hence give a bigger overall detector. In addiction the optical background noise (radiative decays and bioluminescence) is almost absent in deep ice. Finally all the maintenance and deployment operations can be done from the solid ice platform and, with the American scientific and military facilities already present at the South Pole, a great deal of the required infrastructure is already present. Despite to these good ice properties the scattering of photons in ice is significantly more likely than in deep sea water. This affects the accuracy with which the muon direction can be reconstructed. In addiction various factors about the inhomogeneity of the ice (layers of dusts or small air bubbles) make modeling and understanding such an experiment more difficult compared to underwater ones.

A Kilometre-Scale detector, IceCube [49; 51], is being deployed around the AMANDA detector. IceCube will be considerably more sensitive than AMANDA and it will consist in 80 strings with 60 photomultipliers each. The project, whose completion is foreseen in 2010/11, also includes a surface air shower detector array, IceTop, composed of 160 tanks of frozen water with two PMTs each, which will enable correlations with the IceCube events, and therefore will enhance the physics capabilities of the deep ice detector. At present (March 2009) 50 strings were deployed.

1.7.4 KM3NeT (ANTARES+NEMO+NESTOR)

Since IceCube observes the northern sky, it cannot look into the Galactic Centre, a region of particular interest as explained in §1.4.1.4. Only neutrino telescopes in the

northern hemisphere will be able to observe this region and the Mediterranean sea seems to be the right place.

KM3NeT [52] is the Design Study that is addressing different issues linked to the construction of a cost-effective Kilometre-Scale deep-sea neutrino telescope. KM3NeT will be a European and multidisciplinary facility, with a novel working philosophy, giving open access to the neutrino telescope data, and allowing external users to ask for observation time by adapting the online trigger algorithm to specific directions in the sky.

Three mediterranean neutrino telescope projects have joined in the KM3NeT project: NEMO [53], NESTOR [54], ANTARES [55].

The NEMO collaboration has performed extensive enviromental measurments in order to find an optimal site for an underwater neutrino telescope installation and several studies on the development of different solutions to various detector components for a kilometre-scale telescope.

During 7 years and 30 sea campaigns, NEMO collaboration identified as an optimum site the one located at a depth of 3400 m about 80 km from Capo Passero near the Italian coast of Sicily. More recently, on 18 December 2006, two of the key components of the detector apparatus have been deployed at a depth of 2100 m at the Catania Underwater Test Site. A junction box and a four storey tower have been validated in real underwater conditions together with the data acquisition system. This milestone proves the full functionality of the main components of a kilometre-scale detector.

The NESTOR project, with mainly Greek participation, intends to build a Mediterranean detector with approximately the same effective volume as IceCube. Their selected site for the detector is the Ionian sea (Greece) near the West Coast of the Peloponnese at 4 km depth. On 29 March 2003 the NESTOR collaboration successfully deployed the first floor of a detector tower recording the first atmospheric muons.

ANTARES is the experiment on which this work is based and it will be discussed in detail in the chapter 3.

Neutrinos with energies above 100 PeV are difficult to detect by the Cherenkov based optical telescopes. Higher energy detection will be covered by experiments recording radio emission in terrestrial ice masses or in the moon crust, by searching for fluorescence light from neutrino-induced air showers. Since the thesis is based on the
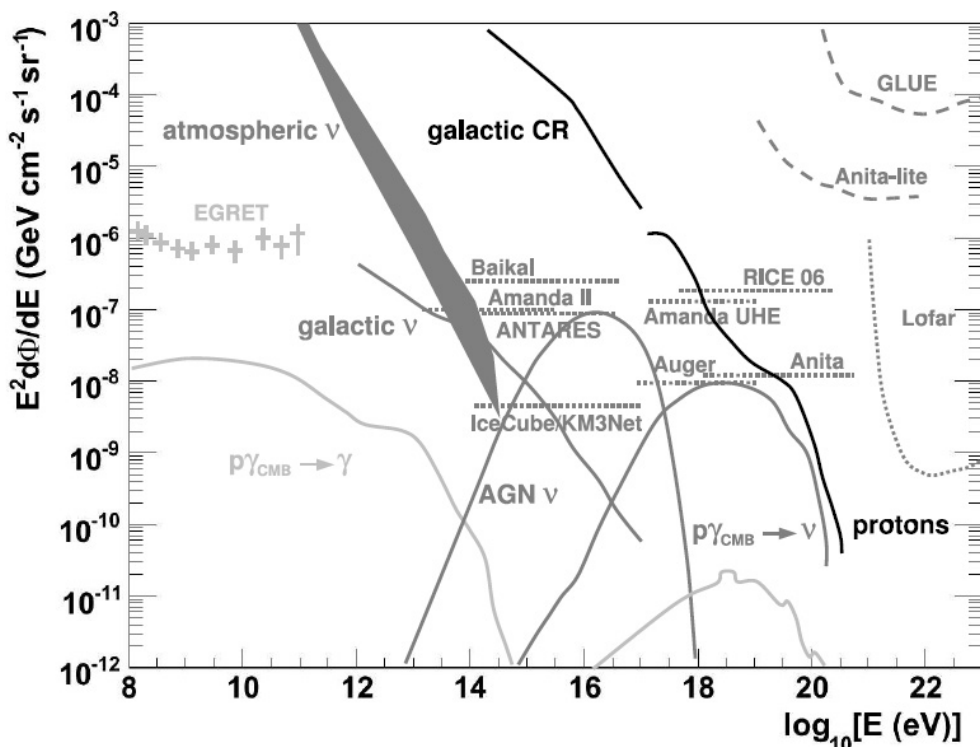
Figure 1.6: Estimated fluxes (full lines) and sensitivities for present and projected neutrino detectors (dashed lines and crosses). Cosmic rays and γ-rays fluxes are also indicated for the sake of comparison. The primary CR spectrum is shown in black. The secondary γ-ray spectrum stemming from proton interactions with the CMB is shown light grey, as well as the instrumental sensitivity for γ-ray from EGRET. In grey are indicated the estimated neutrino fluxes (cosmic and atmospheric fluxes), the present upper limits set by AMANDA-II, Baikal and the expected limits of different future neutrino detectors, like the expected 1 year limit of ANTARES.

the Cherenkov neutrino telescope ANTARES, these different ways of very high energy neutrino detection are not discussed in more details.

Figure 1.6 shows an overall picture of the present and future situation in the neutrino astronomy field. The prospective sensitivities to diffuse neutrino fluxes of future detection experiments and the limits already set by present experiments, are shown together with the estimated fluxes from different models and sources of neutrinos. These limits are referred to a diffuse neutrino fluxes (due to the combination of several unresolvable neutrino sources) and differ from the sensitivities to the point-like sources search analysis.

1. HIGH ENERGY NEUTRINO ASTRONOMY AND NEUTRINO TELESCOPES

Chapter 2

Physics of Atmospheric Muons

The atmospheric muons are the main topic of this thesis. In this chapter some primary cosmic ray (PCR) models are discussed. They are used as first inputs in the Monte-Carlo simulations of underwater atmospheric muons. Particular interest is given to the HEMAS parameterization from which the parametric formulas used in MUPAGE are derived in [56]. MUPAGE [57] is the atmospheric muons generator program used in this thesis analysis and it will be described in §4.2.

Some experimental measurements of the energy spectra of atmospheric muons at sea level are shown and a brief description of the muon energy loss in water is given.

Several characteristics of the underwater muons are then discussed. The results from the parametric formulas mentioned above, which describe the underwater fluxes, are shown for this purpose. Particular interest is given to the multi-μ events which are also the most dangerous background source for neutrino telescopes. A multi-μ event is a bundle of muons (the number of which is called *multiplicity M*) originated from a single CR in the atmosphere and reaching the detector almost at the same time in a plane perpendicular to the shower axis.

The physics process of Cherenkov light generation by muons is finally explained.

2.1 Atmospheric muons

Atmospheric muons are created mainly as a consequence of the decay of charged mesons K and π originated by the interaction of CRs with atmospheric nuclei, as for example:

$$\pi^+ \to \nu_\mu + \mu^+$$
$$\pi^- \to \overline{\nu_\mu} + \mu^-$$

$$\tag{2.1}$$

These particles play an important role in underwater/ice neutrino telescopes since although the detectors are located under a large water/ice depth, a great number of atmospheric muons reaches its active volume (see Figure 1.5). As a consequence they represent the most abundant signal and they can be used to calibrate the detector and to check the validity of Monte Carlo simulation programs to the passage of charged particles. On the other hand atmospheric muons constitute the main background source for the neutrino detection. In fact they can be wrongly reconstructed as upward going particles mimicking muons from very high energy neutrino interactions. This reconstruction error seems to be more frequent when considering muons in bundles (also referred as *multi-μ event*).

In the following an overview of the primary cosmic ray (PCR) models is given. They are the inputs of the MonteCarlo programs used in order to generate atmospheric muons. The simulation starts with the PCR interactions with the atmospheric nuclei and consequent secondary particles creation and propagation. The first step of the simulation gives muons at the sea level from which they are propagated untill the detector level.

Only the *conventional muons* are discussed, muons coming from the decay of charged mesons originated by the interaction of CRs with the atmospheric nuclei. The atmospheric muon component originated from the decay of charmed mesons and other short-lived particles produced in the interactions of CRs with the atmosphere (the so called *prompt muons*) is not considered. The energy at which the contribution of prompt muons to the sea level flux becomes equal to that of muons from π, K decays is expected to be $\sim 10 \, TeV$ to $\sim 10^3 \, TeV$, depending on the charm production model [58].

2.2   Primary Cosmic Ray (PCR) Models

The two main ingredients that enter for first in the MonteCarlo simulations of underwater atmospheric muons are the properties of the inelastic interactions of nucleons with air nuclei and the PCR energy spectrum and composition. It is customary in the MonteCarlo computations to account for 5 groups of primaries, namely H, He, $C + N + O$, $Mg + Si$, Fe. Several parameterizations have been calculated in order to

reproduce the PCR energy spectrum behaviour for individual or group elements.

In this thesis an atmospheric muon generator (MUPAGE, see §4.2) was used which takes, as input, parametric formulas [56] describing the characteristics of underwater muon events (flux, energy spectrum, multiplicity spectrum and radial distance from the bundle axis). Some of these characteristics will be show in the following sections (§2.5.1, §2.5.2, §2.5.3). Such formulas were computed via a full Monte Carlo simulation performed with HEMAS code [59] using the following PCR spectra as input.

DA RIVEDERE ... metti la tabella giusta con H e He invertiti

- **The HEMAS parameterization**: HEMAS [59] is a code developed for the simulations of the muon flux underground and it was extensively used by the MACRO experiment at Gran Sasso [60] in the study of the muon flux at 3400 m.w.e. depth and the muon bundle rate. The interaction model used was DPM-JET [61]. In this code the energy spectrum assumed to generate each group is represented by a function of the form

$$Flux(E) = K_i E^{-\gamma_i} \tag{2.2}$$

  where K_i and γ_i have different values depending on the mass group and E is the energy per particle. Furthermore, for the same nucleus, they have different value before and after the knee energy. The values of the constants calculated in [62] are reported in Tab. 2.1.

In Figure 2.2 the HEMAS and other four parameterizations, used as input of Monte Carlo codes, are shown considering all the particle groups (all-particle). The procedures and the experimental data used in their derivation are not discussed here. For more informations see the referred papers. The plots represent the differential spectra multiplied by $E^{2.7}$ as a function of energy/particle. The value 2.7 is very close to the weighted average of the spectral indexes of the elements with Z from 1 to 28 deduced by the best fits to experimental data in the study by [63]. The "theoretical" spectra will thus appear almost horizontal with a trend to increase/decrease according to their spectral indexes having values smaller/larger than the above chosen value.

The GHSL spectra is closer to the other models. However it covers an energy range smaller than the one of interest for the observations of muons at great depth. The knee

Nucleus	Z	A	K_1 [m^{2}s sr GeV]$^{-1}$	γ_1	K_2 [m^{2}s sr GeV]$^{-1}$	γ_2	E_k [GeV]
H	1	1	20100	2,74	2.1 10^6	3,12	2 10^6
He	2	4	3000	2,56	6 10^6	3.	3 10^6
CNO	7	14	600	2,5	3.7 10^7	3.24	3 10^6
Mg-Si	12	24	877	2,5	6.3 10^7	3.25	3 10^6
Fe	26	56	311	2,36	4.1 10^6	3	2,7 10^6

Figure 2.1: The constants used in the HEMAS model.
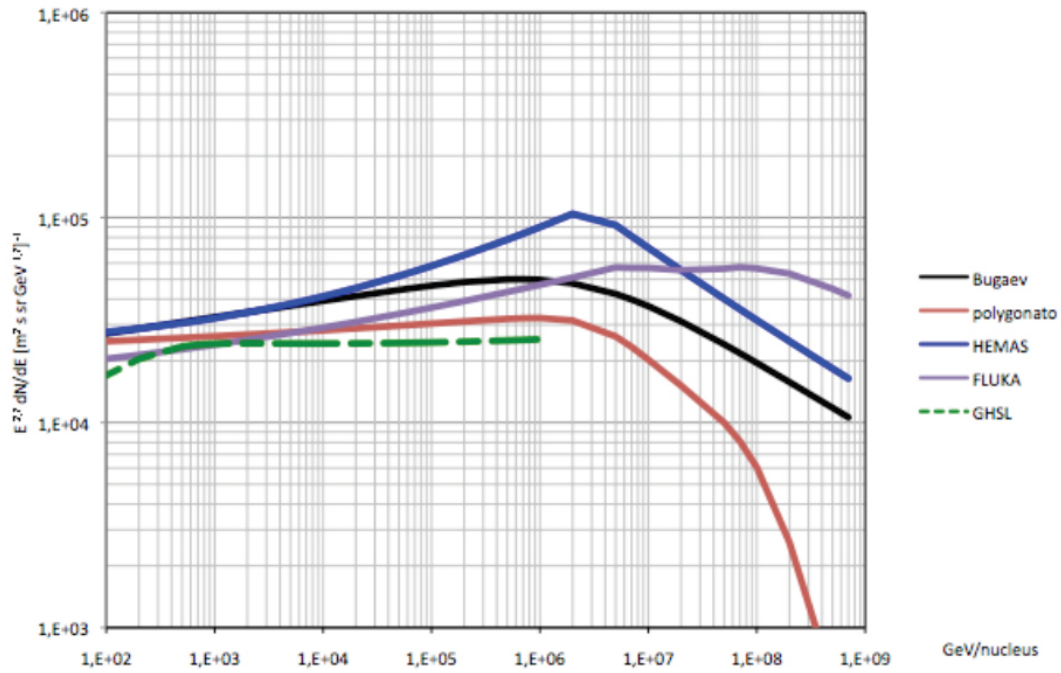
Figure 2.2: The all-particle input spectra of MonteCarlo computations cited in the legend multiplied by $E^{2.7}$. Bugaev [64], polygonato [65], HEMAS [62], FLUKA [66], GSHL [67]

28
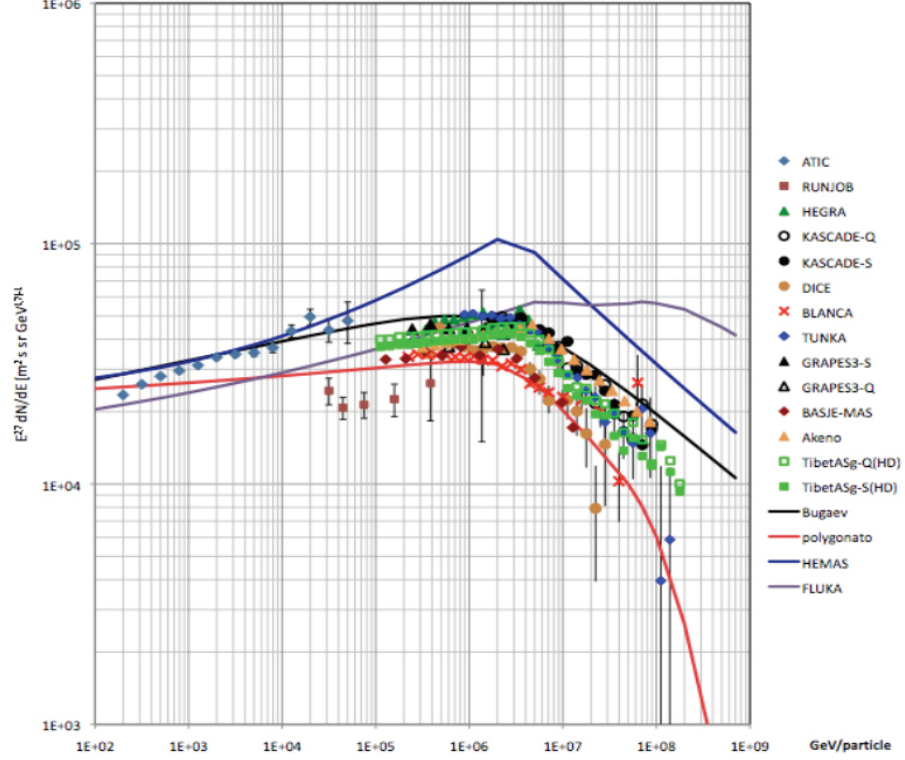
Figure 2.3: The all-particle spectra deduced by direct and indirect measurements and the parameterizations used in MC simulations. The spectra are multiplied by $E^{2.7}$. The MonteCarlo parameterization references are the same as in Figure 2.2. The experimental data references are the followings: ATIC [68], RUNJOB [69], HEGRA [19], KASKADE [70; 71], DICE [72], BLANCA [73], TUNKA [74; 75], GRAPES III [76], BASJE-MAS [77], Akeno [78], TibetASg [79].

position of HEMAS spectrum seems to coincide with that of polygonato and Bugaev parameterizations.

In Figure 2.3 the all-particle spectra as a function of energy/particle resulting from experiments by "direct" and "indirect" measurements is shown compared to the MonteCarlo model predictions. There is a substantial agreement among all the data shown and the MonteCarlo parameterizations. Although HEMAS parameterization is higher in some energy range than the whole data trand, with the chosen interaction model it reproduces correctly the underground muon fluxes as seen by MACRO experiment.
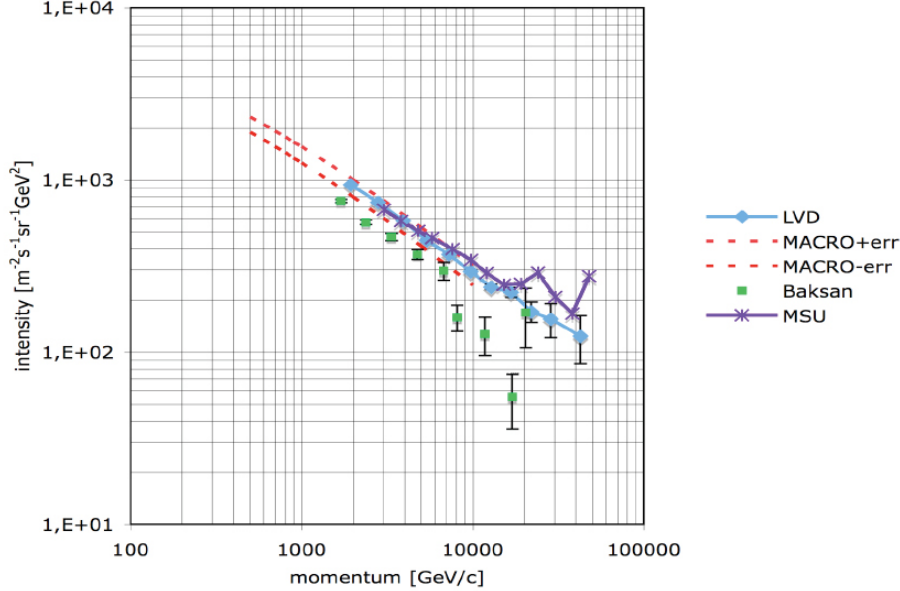
Figure 2.4: Differential energy spectra of vertical ($\theta = 0^o$) muons at sea level obtained by some underground experiments: MACRO [80], LVD [81], Baksan [82], MSU [83]. The ordinate values are multiplied by the momentum to the 3rd power. For MACRO the two lines represents the $\pm 1\,\sigma$ error of the fit.

2.3   Muons at sea level

As already mentioned the interaction of PCRs with atmospheric nuclei generates showers of particles. In the MonteCarlo codes the propagation of such particle showers is performed with several interaction and propagation models until the sea level.

In order to reach the ANTARES detector along the vertical direction, muons must have $E_{th} > 500\,GeV$ at sea level. At such energies only indirect data or underground measurements are available. Figure 2.4 shows the vertical differential spectrum of muons at sea level, obtained by some underground experiments.

From measurements and theoretical calculations the zenithal distribution of atmospheric muon flux at sea level is proportional to $sec\theta$ [84], where θ is the zenith angular direction of the muons.

From the sea level other MonteCarlo programs propagates the muons until the detector level. For the parametric formulas used by MUPAGE, this step was performed by the MUSIC [85] program (see §4.2).
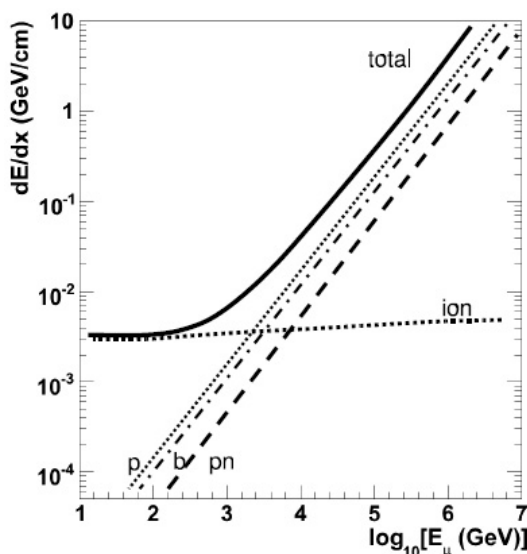
Figure 2.5: Energy loss of muon in water: p = pair production; b = bremsstrahlung; pn = photo-nuclear interactions; ion = ionization.

2.4 Muon energy loss in water

A muon can interact with matter through several processes [43]. They can be divided in two groups: ionization processes and radiative processes. In the ionization processes the muon interacts with the electric field of the electrons cloud of the atom while in the radiative processes (Bremsstrahlung, pair production and photonuclear interaction) it interacts with the nuclear electric field of the atom. The relative importance of these processes depends on the energy of the muon. Figure 2.5 shows the energy loss as a function of the muon energy due to different interactions in water.

Below approximately 1 TeV, the ionisation process dominates the energy loss while above 1 TeV the radiative processes do it. Energy loss through ionisation is approximately constant with a value of about $0.2\,GeV/m$. The radiative processes have an approximately linear dependence on the muon energy. This energy dependence of the total energy loss per unit length can be written in a parametrized formula as:

$$dE_\mu/dx = \alpha(E_\mu) + \beta(E_\mu) \cdot E_\mu \qquad (2.3)$$

where $\alpha(E_\mu)$ is the almost constant term that accounts for ionization, and $\beta(E_\mu)$ stands for the radiative losses which, in first approximation, can be considered as energy
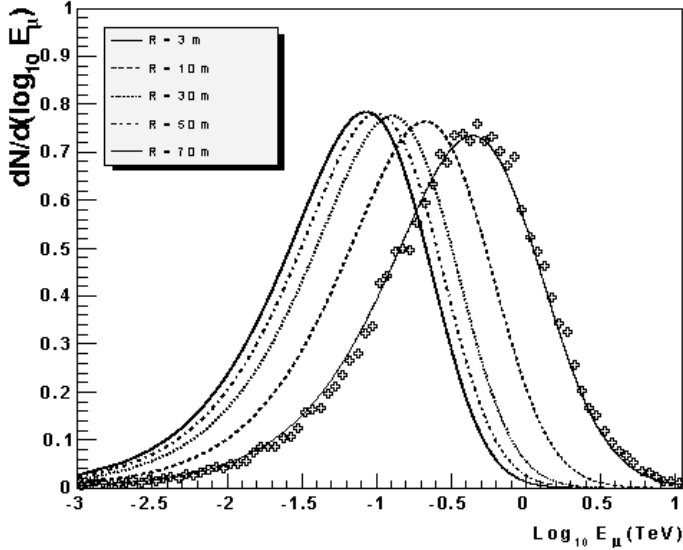
Figure 2.6: Differential energy spectra of vertical ($\theta = 0^o$) muon bundles with multiplicity M=2 at different radial distances from the shower axis (R = 3, 10, 30, 50 and 70). The different lines were computed with a Monte Carlo paramaterisation [56] assuming h=3.5 km w.e. depth. The points are the MonteCarlo data from which the fit for R=3m has been computed.

independent.

2.5 Uderwater muons

In this section some characteristics of the underwater atmospheric muons are shown: energy and multiplicity spectra, lateral spread and depth-intensity relation (DIR). The results come from the parameterizations obtained in [56] and used as imput in the MUPAGE program [57] (see §4.2). Some experimental measurements of the DIR are also shown.

2.5.1 Energy spectrum

From theoretical and experimental considerations, it results that in hadron-air interactions, particles are produced in clusters; the number of charged hadrons follows a negative binomial distribution, whose characteristics depend on the primary energy. The transverse momentum p_t of the mesons follows in part an exponential-law distri-

bution and in part a power-law distribution [86; 87]; most of the energy is concentrated in the very forward region (i.e. near the longitudinal axis). Muons produced in the decay of secondary mesons and reaching a given depth h of water follow the energy distribution of the parent mesons. As a consequence, in a muon bundle, the most energetic muons are expected to arrive closer to the axis shower. This is shown in Figure 2.6, obtained from Monte Carlo parameterizations in [56] assuming the vertical direction and the depth $h = 3.5\ km\ w.e.$

In general the energy spectrum $\frac{dN}{d(log_{10}E_\mu)}$ of muons arriving in bundles depends on the vertical depth h, on the zenith angle θ, on the muon bundle multiplicity M and on the radial distance R of the muon from the shower axis. The energy E_μ^{max}, corresponding to the maximum of the distribution, increases when the zenith angle θ, the multiplicity M and the vertical depth h increases (reaching a constant value for $h > 4.5\ km\ w.e.$) and when the distance R decreases [56] (see Figure 2.7 and Figure 2.8).

2.5.2 Lateral spread

If the muon radial distance R from the shower axis and its distribution as described in [59] are considered, the average value $\langle R \rangle$ of this distribution is found to depend mainly on the vertical depth (it decreases when h increases). Then, for a given h, $\langle R \rangle$ decreases with increasing of the muon multiplicity. Finally, $\langle R \rangle$ does not depend on the zenith angle θ up to $\sim 50°$, then it decreases with increasing θ.

Figure 2.9 shows the normalized lateral distribution of double muons for the vertical direction at different values of the vertical depth h as obtained from Monte Carlo parameterisations in [56]. The average value of the lateral distribution decreases when h increases because the surviving muons are only the most energetic ones in the bundle and as already explained they arrive closer to the shower axis.

Figure 2.10 shows the normalized lateral distribution of muons with multiplicity $M = 2, 3$ and > 3 ($M = 4$) from the vertical direction and at the depth of $3.5\ km\ w.e.$ The average value $\langle R \rangle$ of distribution decreases when M increases, because showers with large multiplicity were originated by higher energy primary CR parents.
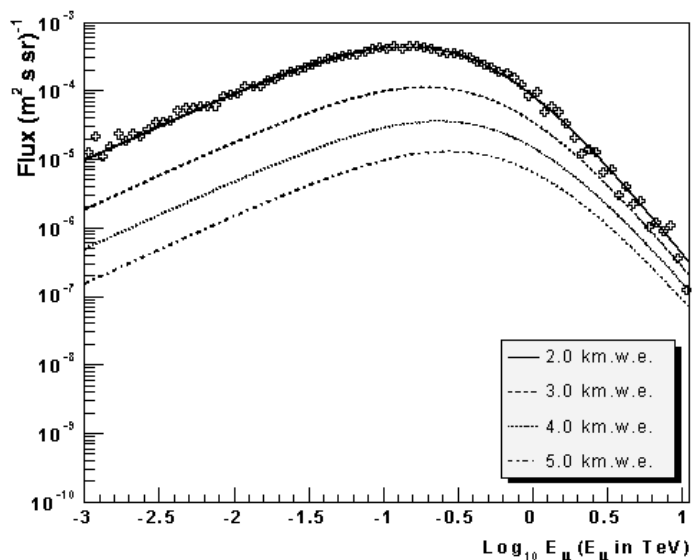
Figure 2.7: Differential energy spectra of vertical ($\theta = 0^o$) single muons at different depths (h = 2, 3, 4 and 5 km w.e.) [56]. The points are the MonteCarlo data from which the fit for h=2 km w.e. has been computed.
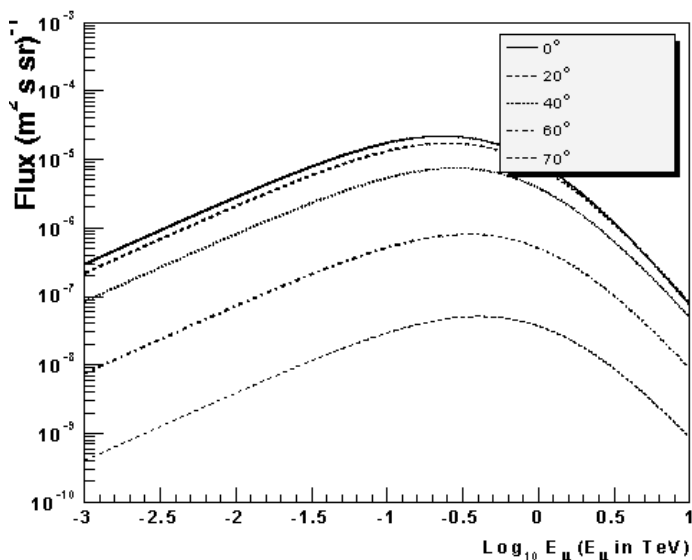
Figure 2.8: Differential energy spectra of single muons at different zenith angles ($\theta = 0^o, 20^o, 40^o, 60^o$ and 70°) assuming h=4.5 km w.e. depth [56].
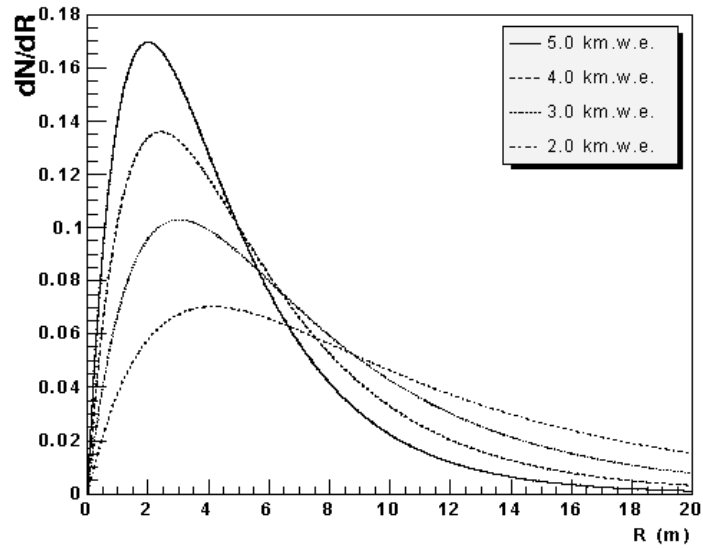
Figure 2.9: Normalized lateral distributions for vertical ($\theta = 0^o$) muon bundles with multiplicity M=2 at different depth (h = 2, 3, 4 and 5 km w.e.) [56].
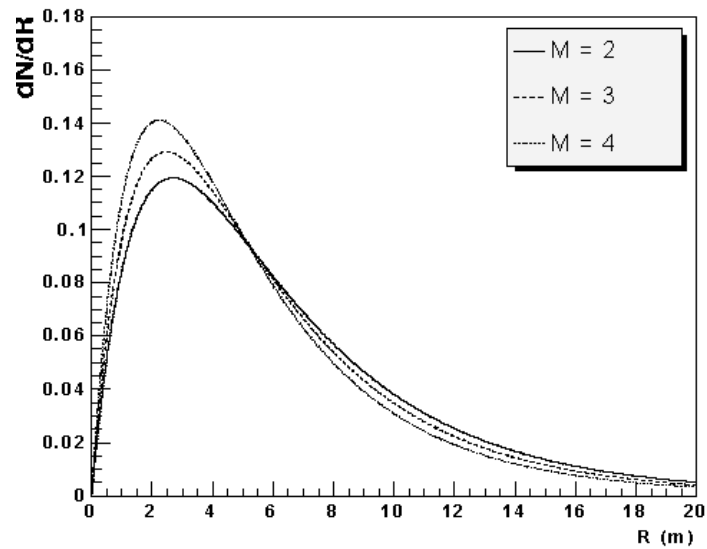
Figure 2.10: Normalized lateral distributions for vertical ($\theta = 0^o$) muon bundles with different multiplicities (M = 2, 3 and 4) at a 3.5 km w.e. depth [56].

35
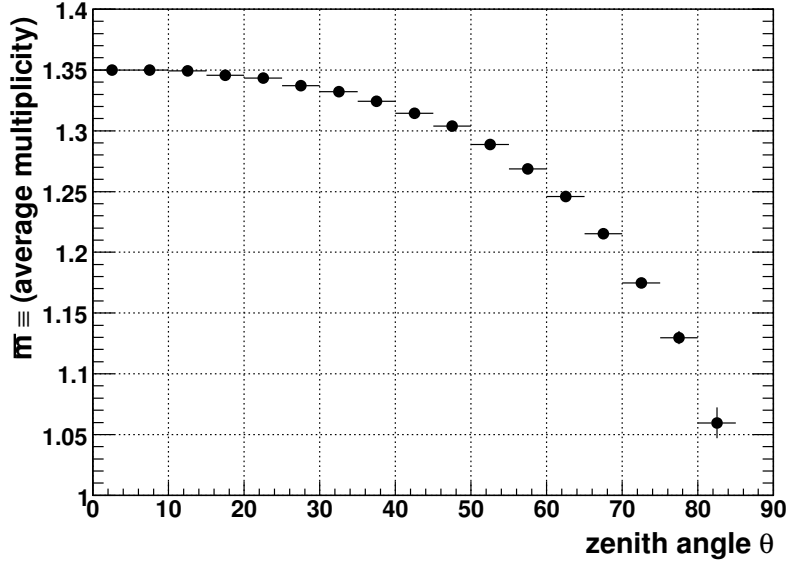
Figure 2.11: Average muon shower multiplicity as a function of the zenith angle at 1890 m of sea depth ($E_\mu > 20\,GeV$). From MonteCarlo simulation using the MUPAGE program (see §4.2).

2.5.3 Multiplicity

The distribution of the muon multiplicities in a bundle depends on the vertical depth h and on the zenith angle θ. The dependence of the multiplicity distribution on these two variables is the following: for a fixed zenith angle θ, bundles with high multiplicity are suppressed when h increases; for a fixed vertical depth h, bundles with high multiplicity are suppressed when θ increases (see Figure 2.11). In both cases the number of muons in the bundle decreases because increasing h or θ means to increase the path lenght in the water through which muons travel.

2.5.4 Depth-intensity relation

The depth-intensity relation represents the muon flux as a function of the vertical depth. In literature this function is usally given for the vertical direction only and it is called $I_\mu(\theta = 0, h)$. The qualitative behaviour of the DIR can be calculated from the knowledge of the sea level μ spectrum and the physics of μ propagation and interactions in matter [88].
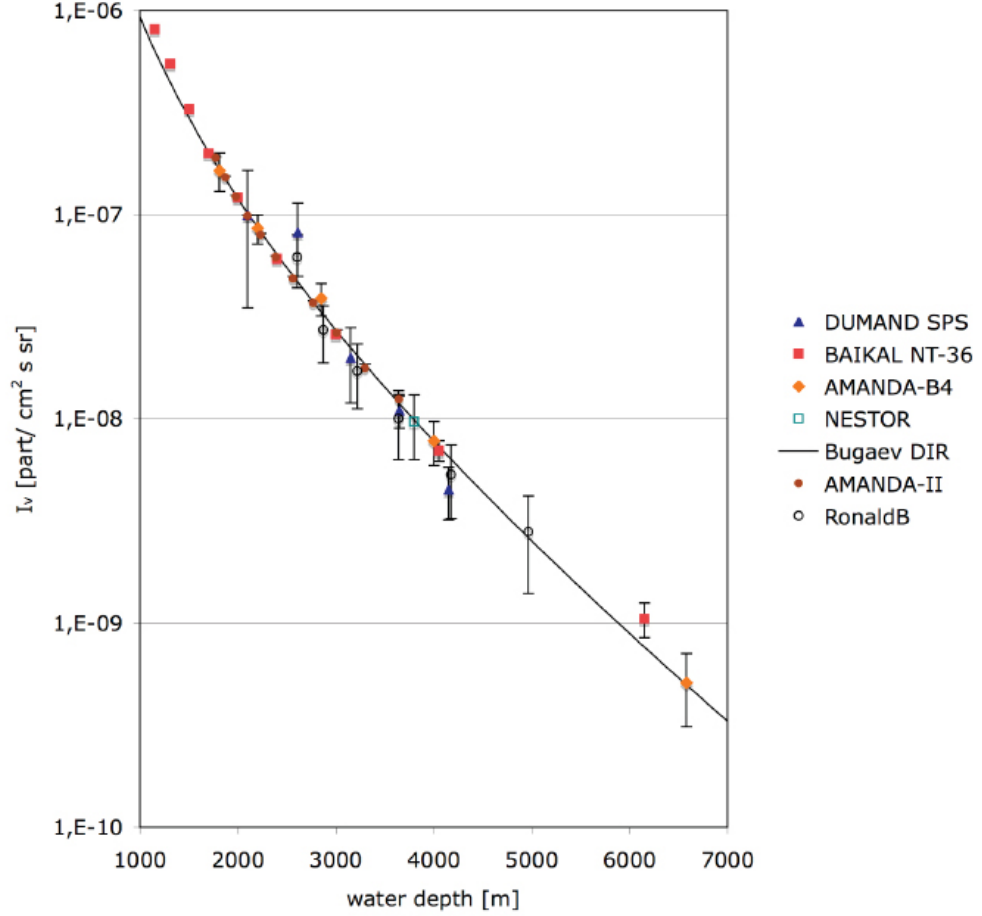
Figure 2.12: Full Line: underwater parameterization of the DIR made by Bugaev. Points: data from some neutrino underwater telescopes, DUMAND SPS [90], Baikal NT-36 [91; 92], AMANDA B-4 [93], NESTOR [94], AMANDA-II [95] and ANTARES 1 line configuration (RonaldB)[96].

Figure 2.12 shows some underwater measurements and a parameterization calculated by Bugaev [89] for the range of interest of the ANTARES depths. The percentage deviations of these values from the predicted Bugaevs DIR are shown in Figure 2.13.

In [56] is shown that the ratio between the number of bundles with multiple muons with respect to single muon events decreases with increasing of the vertical depth ($\sim$ 20% at a vertical depth of 2.0 km w.e and $\sim$ 11% at vertical depths larger than 4.0 km w.e.).

In order to compute the depth-intensity relation for vertical muons from the data,
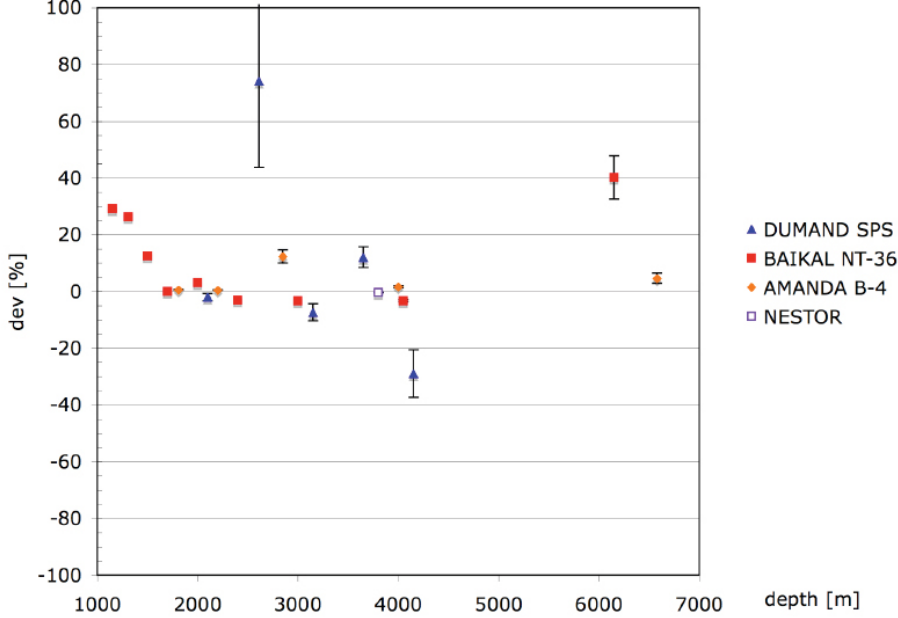
Figure 2.13: Percentage deviations of underwater neutrino telescope measurements from the predicted Bugaev's DIR. Experimental points as in Figure 2.12

it is necessary to know the trigger efficiencies of the detector and the smearing effects due to the used reconstruction algorithm. This is the main topic of the present thesis and it will be described in details in chapter 6.

2.6 Cherenkov radiation

A neutrino telescope is basically a three-dimensional set of arrays of photomultipliers designed to collect the Cherenkov light emitted by neutrino interaction product. The information provided by the number of photons detected and their arrival times is used to infer the neutrino track direction and energy.

Cherenkov radiation is due to a charged particle crossing an insulator medium with speed greater than the speed of light in that medium [97]. In this case the charged particle infers a polarization to the molecules along its trajectory. When the insulators electrons restore themselves to equilibrium after the disruption has passed, a coherent radiation is emitted in a cone (see Figure 2.14) with a characteristic angle θ_C given by

$$cos\theta_C = \frac{c/n}{\beta c} = \frac{1}{\beta n} \tag{2.4}$$
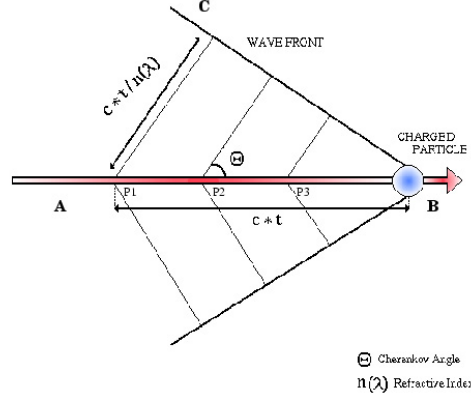
Figure 2.14: Schematic view of the production of Cherenkov radiation by a relativistic charged particle.

where n is the refractive index of the medium and β is the particle speed in units of c. For relativistic particles ($\beta \simeq 1$) and for refractive index of sea water ($n \simeq 1.364$) the Cherenkov angle is $\theta_C \simeq 43^o$.

The number of Cherenkov photons, N_γ, emitted per unit wavelength interval, $d\lambda$ and unit distance travelled, dx, by a charged particle of charge e is given by

$$\frac{d^2N}{dxd\lambda} = 2\pi\alpha\frac{1}{\lambda^2}(1 - \frac{1}{n^2\beta^2})$$

(2.5)

where λ is the wavelength of the light radiation. From this formula it can be seen that shorter wavelengths contribute more significantly to the Cherenkov radiation. For underwater neutrino telescopes, the light absorption by water and the photomultiplier response will strongly suppress some wavelengths. The number of Cherenkov photons emitted per meter in the typical wavelenght range in which the PMTs have their maximum efficiency (300-600 nm) is about 3.5×10^4.

Chapter 3

The ANTARES neutrino telescope

ANTARES (*Astronomy with a Neutrino Telescope and Abyss environmental RESearch*) is at present the largest cherenkov neutrino observatory in the Northern hemisphere. It is a project which involves today about 180 physicists, engineers and sea-science experts from 24 institutes of 7 European countries. The detector is able to explore the Southern sky hemisphere, which represents the most interesting area of the sky due to the presence of the Galactic Centre, where neutrino source candidates are expected. ANTARES will contribute in the search for astrophysical neutrinos with a sensitivity much better than any other previous experiment.

Brief history

The ANTARES project [98] has been set up in 1996. Extensive Research and Developement (R&D) studies have been carried out during the first years (1996÷1999) to prove the feasability of the detector concept [99]. Part of these studies was the deployment of several autonomous lines devoted to the characterization of the ANTARES site and the validation of the sea operation procedures. In particular several site properties have been extensively studied: the optical properties of the surrounding water, the biofouling on optical surfaces of the devices, the optical backgrounds due to bioluminescence and to the decay of the radioactive salts present in the sea water, the geological characteristics of the ground. According to these studies the site selection was located at a distance of about 40 km from La Seyne-sur-Mer (France) at 2475 m depth (see §3.5). The acoustic positioning system was tested with a demonstrator line ("LINE5")
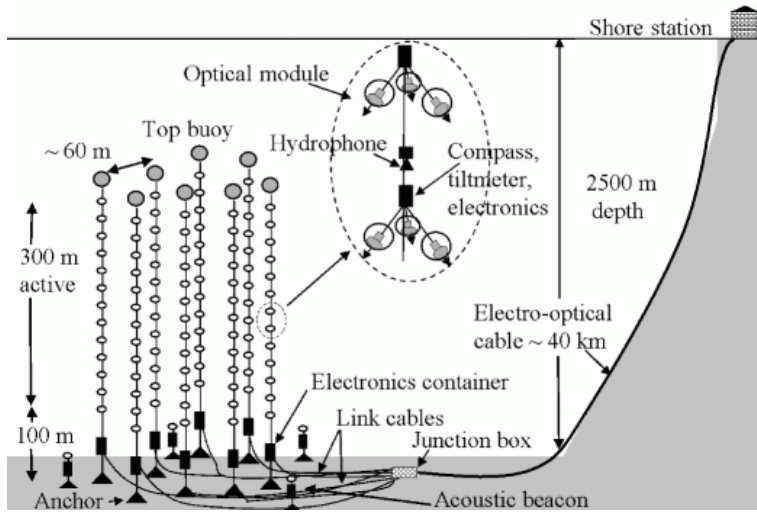
Figure 3.1: Schematic view of the ANTARES detector.

immersed from november 1999 to June 2000, which also allowed to measure the atmospheric muon zenith distribution. The first complete line of the neutrino telescope was deployed on 14th February, 2006 and connected to the Junction Box by means of an underwater Remote Operated Vehicle (ROV). Since that moment line by line the detector has been completely deployed and two years after the first line deployment the detector was completed on 30th May, 2008.

3.1 Detector layout

The detector consists of an array of twelve independent and flexible lines made of mechanically resistant electro-optical cables, separated by a distance of $\simeq 74$ m. These lines are anchored to the seabed and are tensioned with a buoy located on the their top. Each line has 25 storeys holding a triplet of photomultiplier tubes (PMTs) used to collect the Cherenkov light induced by the relativistic charged particles crossing the sea water, coming from neutrino interactions in the surrounding vicinities of the detector. Figure 3.1 is a schematic view showing the principal componentes of the detector. The detector is operated from a control room, the *shore station*, located in La Seyne sur Mer. In the next the main components of the ANTARES detector are reviewed.
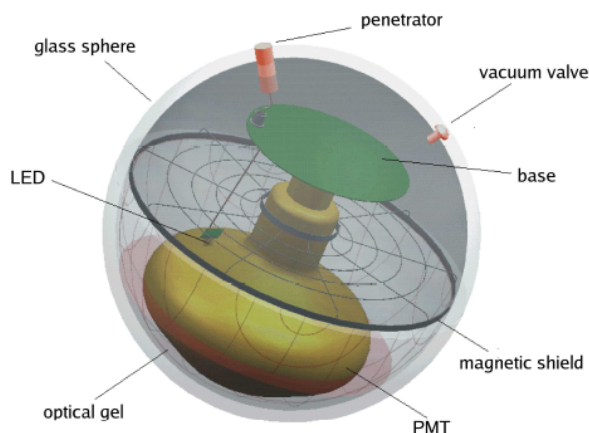
Figure 3.2: Schematic view of the OM of ANTARES.

3.1.1 Optical Module (OM)

The 900 optical modules [101] are the basic elements of the ANTARES detector. They consist in a glass sphere with a diameter of 43 cm, a thickness of 1.5 cm and a transmission better than 95%, capable to withstand the water pressure up to 700 bars. The sphere houses the enclosed PMT and the associated electronics. A black paint in the lower hemisphere reduces inner reflextion. This makes up the basic optical unit of ANTARES called the Optical Module (OM). Figure 3.2 shows a schematic view of the OM. The studies performed by the collaboration during the R&D phase to find a suitable PMT led to the selection of the 14-stage, 10 Hamamatsu R7081-20 model [100]. In order to ensure a good optical coupling between the sphere and the PMT photocathode, a silicon gel is used (SilGel 612 A/B) that ensures the proper optical coupling (ngel $\simeq 1.40$, nglass $\simeq 1.48$, nwater $\simeq 1.35$). Among the associated electronics, there is an internal LED system used for the transit time calibration (see §3.4). Finally a μ-metal cage, an iron and nickel alloy of high magnetic permeability, shields the PMT from the Earth's magnetic field which is expected to be uniform and pointing downward at 23° from the vertical and with an intensity $\simeq 0.5$ G.

3.1.2 The storey and the Local Control Module (LCM)

The OMs are grouped in triplets in a *storey* and mechanically fixed to the lines. The three OMs of each storey are equally spaced in the azimuth angle at 120° and they are

Figure 3.3: Picture of a storey of ANTARES. You can see the three OMs around the LCM titanium cylinder placed in the centre of the storey.

arranged with the axis of the PMT 45° below the horizontal. The electronic componentes are housed in a titanium cylinder, the so called *Local Control Module* (LCM), linked to the OMs through a cable penetrator (see Figure 3.3). Five storeys form a *sector*, which is an indipendent unit concerning the power distribution and the data acquisition system (DAQ). One out of the five storeys of a sector houses a *Master Local Control Module* (MLCM), which contains, in addiction to the standard LCM electronic components, all the electronic boards for all the funcionalities at the sector level: an Ethernet switch, a bidirectional concentrator and a Dense Wavelenght Division Multiplexing (DWDM) which multiplexes the data signal from the five storeys onto one optical fibre at the particular wavelenght characteristic of that storey.

3.1.3 The line

A line is made by a mechanically resistant electro-optical cable 448 meters long, along which 25 storeys are installed at a relative distance of 14.5 m. The first 100 m above the seabed are not instrumented in order to avoid the possible spread of sea mud
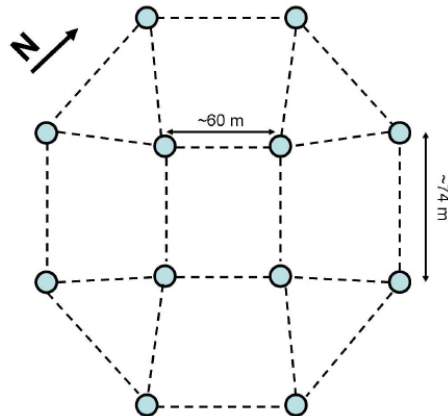
Figure 3.4: Layout of the detector shape. Each dot represents a line which are placed in an octagonal shape.

and dirt due to underwater currents. The study of the detector layout can be found in [102]. In the final configuration the distance between the 12 lines is $\simeq 74$ m and they follow an octagonal shape (see Figure 3.4), which ensures the flat response of the detector in azimuth angles. The line is held vertical by a buoy located on its top and are anchored to the seabed by a dead weight located in the so called *Bottom String Socket* (BSS). Lines can be recovered by releasing this weight from the BSS by issuing an acoustic command from a ship on the surface. Each string is also instrumented with an electronics container in the base called *String Control Module* (SCM).

In addition to the 12 standard lines, there is also an additional line called *Instrumentations Line* (IL) equipped with different instrumentation devices to perform detailed oceanographic and water properties measurements.

3.1.4 The Junction Box and the electro-optical cable

The *Junction box* (JB) is connected with each SCM to which it provides power, clock, control signals and by which it gets data. The internal elements of the JB are protected by the water pressure and by the corrosion by a titanium egg-shape structure which is housed in a parallelepiped frame in order to provide stability on the seabed. This frame is equipped with two front panels with the 16 connectors for the 12 lines, the instrumentation line and the spares. The JB receives power from the power hut placed on the shore station through the 40 km long *Main Electro-Optical Cable* (MEOC).
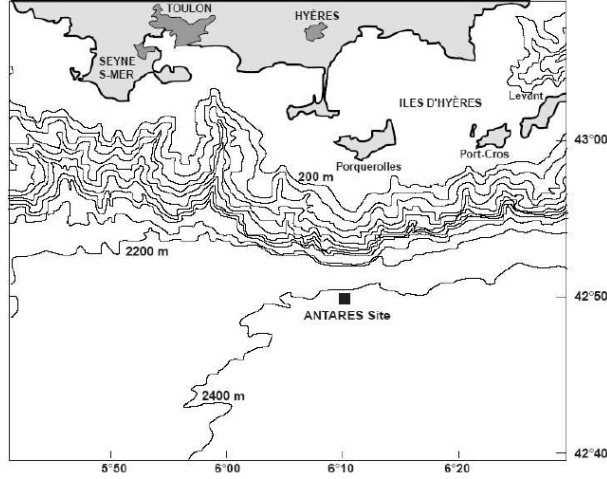
Figure 3.5: Map of the place in which the ANTARES detector is located. 2475 m depth, 40 km away from the shore station.

Through the same cable the data are sent to shore. The MEOC contains an internal steel tube and 48 monomode optical fibres. It is a standard telecommunication cable and is protected and insulated by a set of external layers of copper and steel with a total diameter of 58 mm. Thanks to its building properties finalized to withstand the external water pressure and to resist the corrosion, it is expected to last for at least 10 years.

3.2 Site evaluation

The place in which the ANTARES detector has been deployed is near the French southern coast at 2475 m deep under the Mediterranean Sea at coordinates $42^o50'$ N, $6^o10'$ E (see Figure 3.5). The distance to the shore station, placed in La Seyne sur Mer, is about 40 km. The sky coverage is $3.5\pi sr$ with view on the Galactic Centre during 67% of the time. During the R&D phase of the experiment an extensive measurement program on the detector site has been carried out in order to evaluate some environment parameters and the optical water properties. This section reviews the most relevant results concerning the water optical properties, the biofouling, the sedimentation and the optical background.
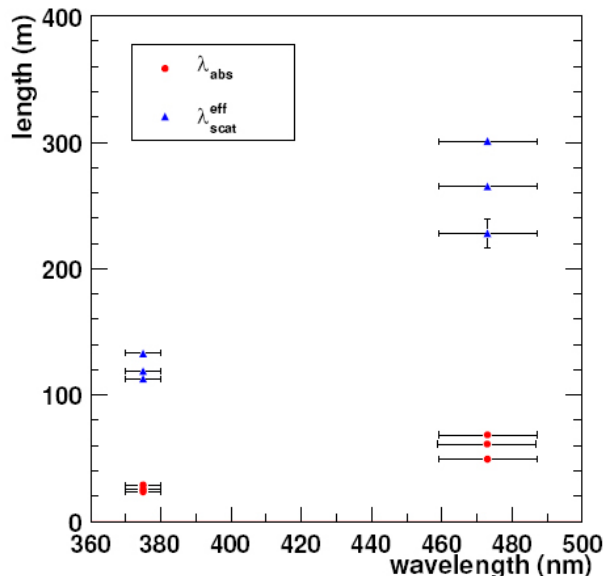
Figure 3.6: Absorption and effective scattering lenghts of water measured at ANTARES site at different periods of the year for two different light wavelenghts (UV, Blue) [103]. The horizontal bars come from the source spectral resolution.

3.2.1 Water optical properties

The knowledge of the photon propagation in the sea water is very important for a Cherenkov neutrino telescope as ANTARES. The propagation is defined by the optical properties of water such as the absorption and the scattering of light in water and the group velocity of light. The absorption and scattering are described respectively by the following two quantities: absorption lenght λ_{abs} and scattering lenght λ_{scat}.

These quantities have been studied during several sea capaigns from 1997 to 2000 using different autonomous lines [103]. Their combination gives the definition of the effective attenuation lenght (λ_{att}^{eff}):

$$\frac{1}{\lambda_{att}^{eff}} = \frac{1}{\lambda_{abs}} + \frac{1}{\lambda_{scat}^{eff}} \tag{3.1}$$

where λ_{scat}^{eff} is defined as $\lambda_{scat}/(1 - \langle cos\theta \rangle)$ with $\langle cos\theta \rangle$ the average cosine of the total scattering angular distribution. The effective attenuation lenght gives an indication of the fraction of photons detected at a distance D from the source with respect to those emitted. Considering an isotropic source of light, the intensity of the emitted radiation at a distance D from the source $I(D)$ is related to the emitted intensity $I(0)$ through

the λ_{att}^{eff} as follows

$$I(D) = I(0)/D^2 \times exp(-D/\lambda_{att}^{eff}) \tag{3.2}$$

The effective attenuation lenght was measured with an experimental setup using a collimated and a continuous LED source located at different distances from the optical module. The measured value for wavelenght $\lambda = 466nm$ is:

$$\lambda_{att}^{eff}(collimated) = 41 \pm 1_{stat} \pm 1_{syst}m. \tag{3.3}$$

The absorption and scattering lengths were measured separately using different experimental setups. A set of measurements were recorded at different periods of the year and are shown in Figure 3.6.

3.2.2 Biofouling and sedimentation

The detector elements are exposed to particles sedimentation and adherence of bacteria (biofouling) which reduce the light transmission through the glass sphere of the OMs. These effects on the ANTARES optical modules have been studied [103]

The experimental setup consisted in two resistant glass spheres similar to those used for the OMs. One of them was equipped with five photodetectors glued to the inner surface of the sphere at different inclinations (zenith angles θ) which were illuminated by two blue light LEDs contained in the second sphere. The measurements went on during immersions of several months and extrapolated to longer periods of time. In Figure 3.7 is shown the light transmission as a function of immersion time for the the five photo-diodes. As can be expected there is a tendency in the fouling to decrease when the zenith angle on the glass sphere increases. After 8 months of operation, the loss of transparency in the equatorial region of the OM dropped only $\simeq 2.7\%$ and then it seems to saturate. Extrapolations indicate a global loss after 1 year of $\simeq 2\%$ (taking into account the two glass spheres used in the setup). Taking into account that the PMTs of ANTARES point 45° downward (zenith angle of 135°), the biofouling and the sedimentation don't represent a major problem for the experiment.

3.2.3 Optical background

The optical background has an environmental origin and it is responsible of the constant count rate in the PMTs [99]. As you can see from Figure 3.8 the count rate of PMTs can be decomposed in a continuous component, the baseline rate, which stands from
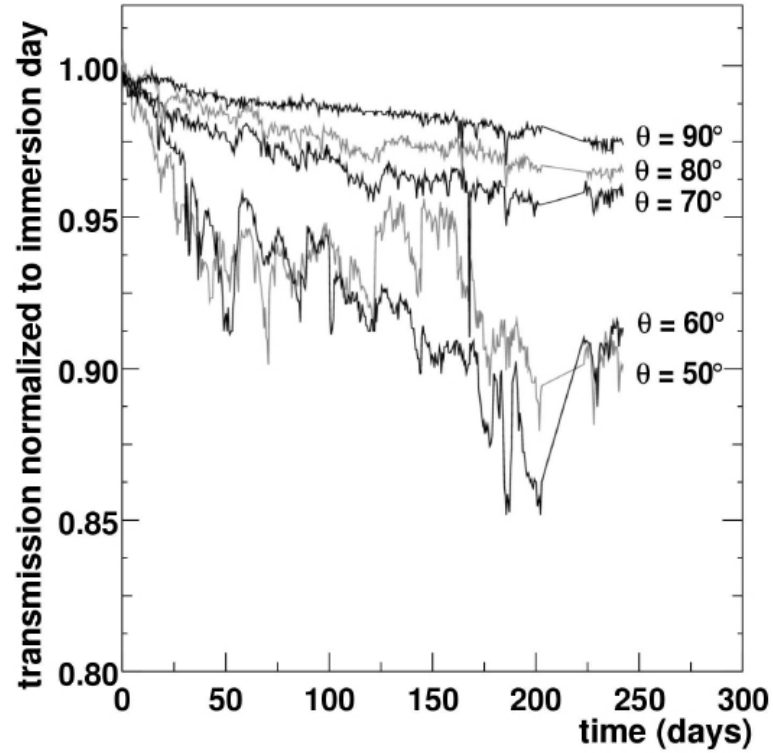
Figure 3.7: Light transmission of ANTARES OM as a function of the time since the immersion day. The different curves refers to the different photodetectors oriented at different zenith angle θ. From [103].
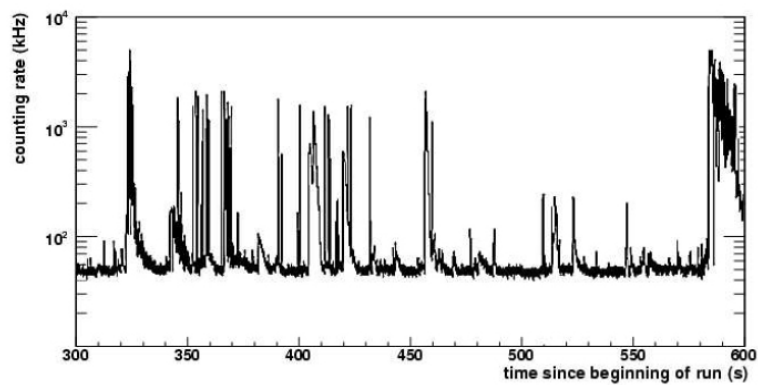
Figure 3.8: Hit rate has seen by a PMT of ANTARES. There is a continuous base line rate and burst rate. Both the baseline and the burst rates depend from the period of takink data.

49
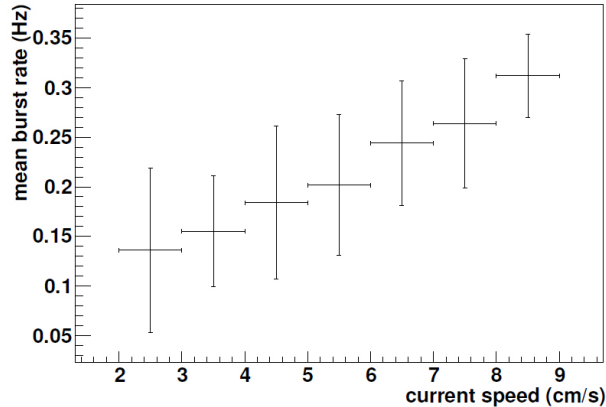
Figure 3.9: Mean burst rate as a function of the sea current speed from [104]. The positive correlation of the two quantities is evident.

60 kHz to 90 kHz depending from the period of the year, and some picks due to rapid ($\simeq 1s$) bursts of several MHz.

The first component, the baseline rate, is mainly due to two different processes: decay of radioactive salts and bioluminescense from bacteria. The radioactive decay involves the ^{40}K, a salt present in the sea water which yields either an electron or a high energy photon:

$$\beta - decay \qquad ^{40}K \rightarrow ^{40}Ca + e^- + \bar{\nu}_e \quad BR = 89.3\% \qquad (3.4)$$

$$e - capture \quad ^{40}K \rightarrow ^{40}Ar^* + \nu_e \rightarrow ^{40}Ar + \gamma \quad BR = 10.5\% \qquad (3.5)$$
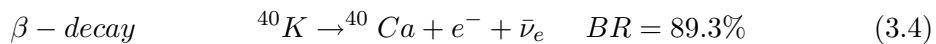
The electron in the β decay process has a maximum energy of 1.3 MeV and the energy of the γ is 1.5 MeV. The γ ray scatters to produce Compton electrons. In both cases the electrons have enough energy to induce Cherenkov radiation in water. Taking into account the salinity in the ANTARES site (S = 38.47 per mil), this produces a continuous and random optical signal which yields a counting rate of $\simeq$ 30 kHz.

The second component of the baseline rate is due to the light emitted by bacteria. They emit light continuously and without any external stimulation. Large baseline variations observed during sea campaigns are due to variation in bioluminescent bacteria activity, which are not correlated to the water current speed.

The discontinuous component is due to multi-cellular organisms which emit light in short flashes. This contribution to the whole count rate is positively correlated to the water current speed (see Figure 3.9).
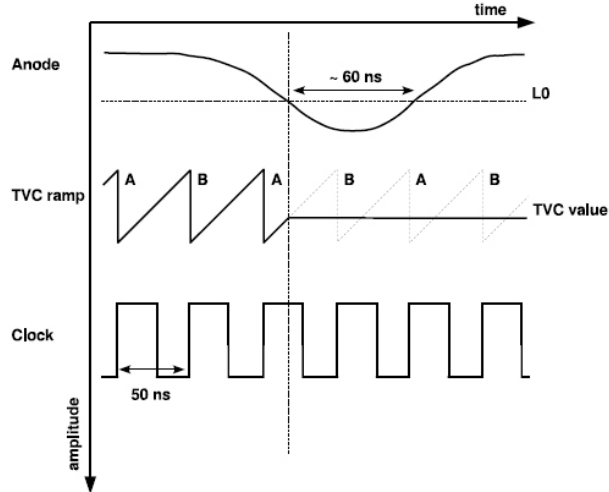
Figure 3.10: Schematic representation of how the Time-to-Voltage converter works in order to interpolate between two clock signals. Two indipendent ramps, **A** and **B**, are used to avoid dead times.

3.3 Data acquisition system

The design of the data acquisition (DAQ) system of the ANTARES telescope is briefly explained. For further information refer to [105] where the DAQ is extensively described.

The PMT signal is processed by an ASIC card (the Analogue Ring Sampler, ARS) which measures the arrival time and charge of the pulse. The distortion and attenuation of the analogical signal provided by the PMT through the 40 km long cable led the collaboration to the decision to digitize the signals before sending them to shore. The digitization of the signal is triggered when the voltage crosses a certain threshold L0 set to a fraction of the single photo-electron average amplitude (typically 0.3 p.e.). The charge is then integrated during a time window of 35 ns and digitized by a 8-bit ADC Analog-to-Voltage Converter (AVC). After the integration time, the ARS chip is idle for about 200 ns. To limit the dead-time in the data acquisition, two ARSs that work in flip-flop mode are connected to each PMT.

During the digitization, the signal is time-stamped assigning the time with respect to the master clock at which the L0 threshold is crossed. To measure the L0 time within the 50 ns interval between two subsequent clock pulses, a linear voltage ramp

is generated and stopped by the L0 signal. This Time-to-Voltage Converter (TVC) provides a voltage which is digitized with an eight-bit analogue-to-digital converter. The TVC procedure is illustrated in Figure 3.10.

After the signal digitization, the result of the ARS is buffered in a 64 MB SDRAM and separated in frames covering a certain period of time. The length of this time window can be set to values between 10 and 100 ms. Each frame is sent as a single packet to shore. A set of PCs in the shore station handles all the sent raw data. All frames that belong to the same time window are processed by the same PC. This collection of frames belonging to the same time window is called a time slice. A time slice contains all data digitized by all ARS in the detector in a given time window. Depending on the PMT signal rate, the fraction of frames sent to shore (sampling mode) has to be adapted in order to not saturate the DAQ system.

The basic unit in the DAQ system is the group of 5 LCMs that constitutes a sector. In each sector there is an MLCM containing an Ethernet switch that merges the links from the five storeys into a single Gb/s Ethernet link. The MLCMs of all sectors transfer the signals to the SCM. Both MCLM and SCM include a Dense Wavelength Division Multiplexing (DWDM) system used for data transmission in order to merge several 1Gb/s Ethernet channels on the same pair of optical fibres, using different laser wavelengths. The SCM is also used for the slow control of the electrical power and calibration systems and also for the clock signal distribution and has an additional 100 Mb/s link to shore. The SCMs of the lines are linked to the junction box by electro-optical cables which are connected using a unmanned submarine. Finally the MEOC (see §3.1.4) links the junction box with the shore station where the data are filtered and recorded. A schematic picture of the DAQ system is shown in Figure 3.11.

Except for the L0 threshold selection in the ARSs, no further filtering of the PMT signal is done offshore. All hits are sent to shore, feature of the DAQ which is commonly referred to as *all-data-to-shore* implementation. This implementation of all raw data is the main challenge of the ANTARES DAQ system, because of the high background rates. About 99% of the signals are essentially due to optical background with a charge corresponding to one photo-electron. As a consequence the amount of raw data sent to shore is too large to be fully stored, so it is first analysed by the so-called DataFilter program. For triggering purpose a subset of L0 fulfilling particular conditions (Level 1
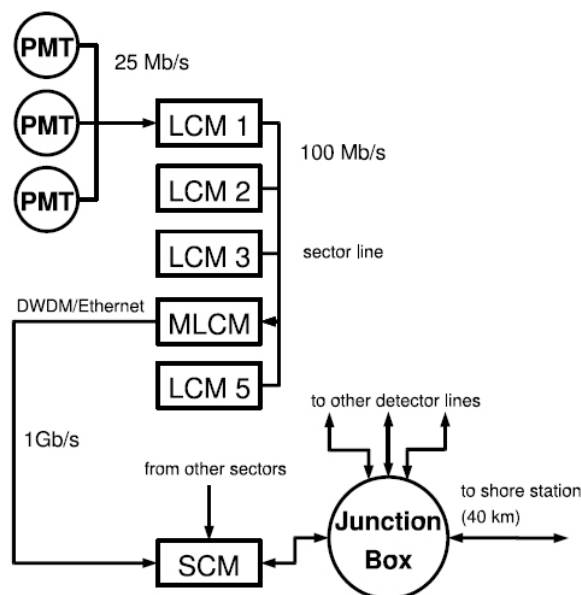
Figure 3.11: Shematic representation of the ANTARES DAQ system. The flux of the data is shown.

hits, L1) is defined. This subset corresponds either to coincidences of L0 on the same triplet of OM of a storey hits within 20ns, or a single high amplitude L0 (typically > 3 p.e.). The DataFilter processes all data online and look for a physics event by searching a set of correlated L1 hits on the full detector on a $\sim 4~\mu s$ window. In case of an event is found, all L0 hits of the full detector during the time window are written on disk, otherwise the hits are thrown away. Each DataFilter program running on the PC has to be finished with processing a time slice of $\sim$ 100ms before it receives the next. This imposes an optimisation of the DataFilter programs in terms of processing speed, and it determines the number of PCs required for online data processing and the specifications of these PCs.

3.4 Time and position calibration

One of the most important characteristic for a neutrino telescope is the capability to reconstruct the direction of the muons trajectory with a good angular resolution. ANTARES is expected to achieve very good angular resolution ($< 0.3^o$ for muon events above 10 TeV). This pointing accuracy is closely related to the precision in the deter-

mination of the arrival time of the Cherenkov photons at the PMTs and of the spatial positioning and orientation of the OMs. These requirements need different calibration systems for timing and positioning.

Due to the underwater sea current the ANTARES lines move slowly. The positions of the OMs are measured on real-time, typically once every few minutes, with a system of acoustic transponders and receivers on the lines and on the sea bed which, measuring the travel times of acoustic pulses, make possible a three dimesional reconstruction of the detector elements. For such a positioning system the knowledge of the sound speed in the water is needed. This speed is dependent on pressure, salinity and temperature. Therefore the detector is equipped with sound velocimeters and with indipendent pressure, salinity and temperature devices. In addition to the acoustic system, each LCM is equipped with a bi-axial tilt meter and compass in order to measure pitch, roll and heading.

The absolute time is provided by clocks placed inside each (M)LCM. These clocks are synchronized by a common clock signal generated on-shore and synchronized with GPS time to an accuracy of 100 ns. Anyway, though the absolute time resolution is needed in order to correlate the tracks with astrophysical events, it doesn't affect the reconstruction quality, which is affected by the relative time resolution between OMs. This relative time is limited by the transit time spread of the signal in the PMTs (about 1.3 ns) and by the scattering and chromatic dispersion of light in sea water (about 1.5 ns for a light propagation of 40 m) [103; 106]. The electronics of the ANTARES detector is designed to contribute less than 0.5 ns to the overall time resolution.

Several systems are implemented to perform time calibration measurements. The internal Optical Module LEDs inside each OM is used to measure the relative variation of the PMT transit time using data from dedicated runs. For the measurement of the relative times between different OMs and the influence of light propagation, a system of optical beacons [107] is in place. They allows the relative time calibration of different OMs by means of independent and well controlled pulsed light sources distributed throughout the detector.

Chapter 4

Analysis data sample and programs

In this chapter an introduction to the MonteCarlo production chain is given and the programs used in the present analysis are described. The real and MonteCarlo data samples considered are defined. Finally the reconstruction program is discussed.

4.1 MonteCarlo programs

The main steps in the Monte Carlo simulation are performed by the programs listed below. They are usually referred to as the *"MonteCarlo programs chain"* beacause they run in a step-by-step manner with the output of one program being used as the input to the next. The whole Monte Carlo chain is schematically shown in Figure 4.1.

- PHYSICS GENERATOR: it generates the kinematics of the particles (usually muons or neutrinos) on the surface of the *CAN*. The CAN is a virtual volume which extends about two and an half absorption lenghts, both in radius and in vertical lenght, over the instrumented volume (see Figure 4.2). The particles that don't cross the CAN surface are not stored in the ascii output file because it is very unlike that such particles can produce Cherenkov radiation visible to the PMTs.

- TRACKING AND CHERENKOV LIGHT GENERATION: it propagates the track of the particles inside the CAN volume and it generates the Cherenkov light. The number of photo electrons generated in each PMT per event are added in the ascii output file together with the previous informations.
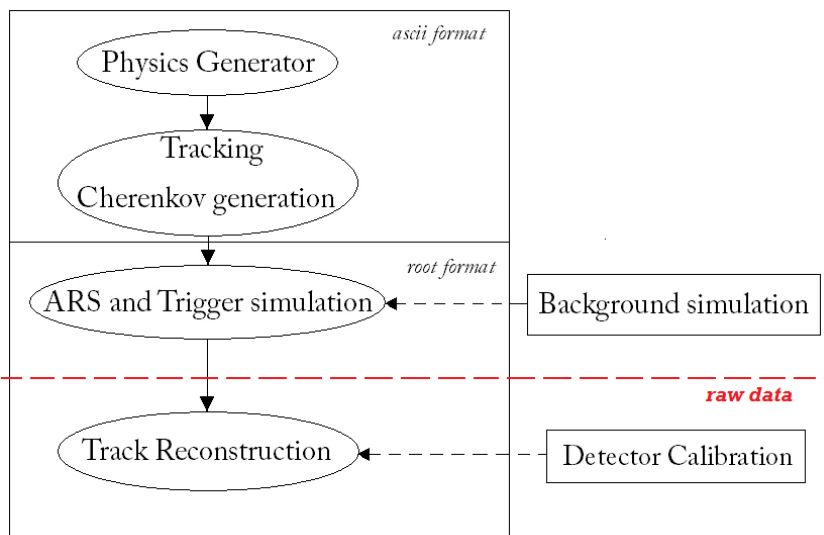
Figure 4.1: Scheme of a general MonteCarlo production chain. After the trigger program the data are in the same form than the real ones: the *raw data*
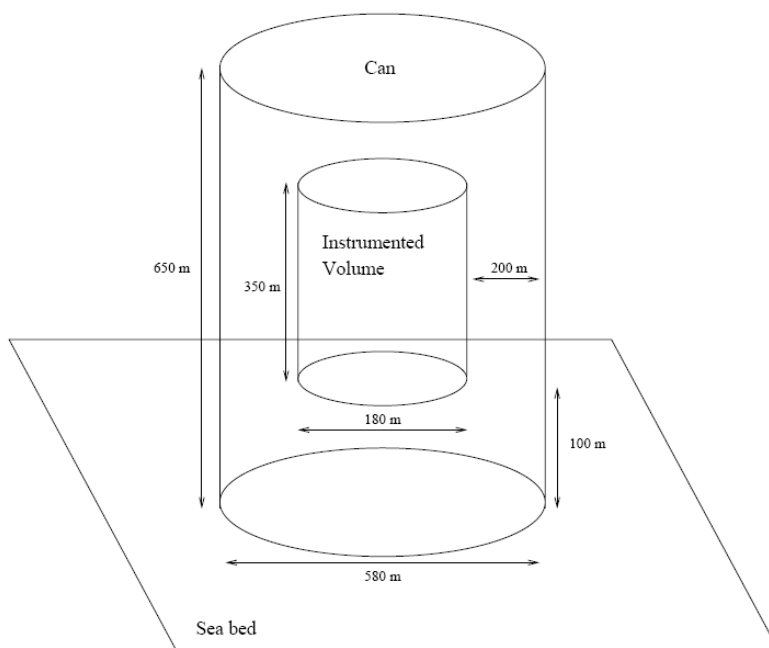
Figure 4.2: Schematic view of the ANTARES CAN. The CAN extends about two and an half absorption lenghts, both in radius and in vertical lenght, over the instrumented volume.

- DATA FORMAT CONVERSION (ASCII → ROOT): the next programs manage both input and ouput files in the ROOT [108] format. The needed conversion is performed at this point of the MonteCarlo chain.

- BACKGROUND SIMULATION: the background rate can be generated and added to the MonteCarlo events in the following two ways:
  - a fixed background rate is specified by the user, which is added to the data according to a Poisson distribution;
  - a real run is specified by the user and the corresponding PMTs counting rates are added in the simulation.

  In the first case only the noise due to the radioactive salt decay is added. This can be performed by the Cherenkov generation program directly. In the second case also the biological activity is taken into consideration. This is performed by a dedicated program which takes a real run as input and gives a ROOT file as output which is merged to the MonteCarlo file in the following program.

- ARS and TRIGGER SIMULATION: it simulates the ARS electronic and it selects the data according to a particular user specified trigger algorithm. The trigger works as a filter: it keeps only events whose hits are likely generated by Cherenkov light discarding the remainings. Finally only the events which survive the trigger are stored into the output file.

The MonteCarlo data at this point are in the same form than the real ones: the *raw data*. From the raw data some physical informations can be inferred with a reconstruction program:

- TRACK RECONSTRUCTION: it performes a track reconstruction algorithm to the events stored in the input file. For the real data analysis the program read the position, time and charge calibrations from a database. For the MonteCarlo data analysis the PMT positions are read from the detector file used in the simulation. If the reconstructed track is considered acceptable, its direction, time and other related informations are stored in the output file.

4.2 Physics generator of atmospheric muons

ANTARES uses two different Monte Carlo physics generators for atmospheric muons. The first one is a full MonteCarlo based on *Corsika*. The second one is based on a parameterization of the underwater muon flux [56] (*MUPAGE*). The full simulation has to be performed choosing a simple $E^{-\gamma}$ primary flux spectrum for all nuclei. It is then possible to reweight with any other user preferred flux model. On the contrary in using the parameterized simulation the user cannot change the primary CR composition because it is fixed and the events cannot be reweighted. The main advantage of the parameterized simulation is its computational speed, much faster than that of the full simulation. For example the generation of a data set with a livetime equivalent to one month requires about 300 hours of CPU time on a 2xIntel Xeon Quad core, 2.33 GHz with MUPAGE. In the following the two generator programs are briefly described. For a more detailed description refer to the referred papers.

4.2.1 Full simulation

The full Monte Carlo simulation [109] is based on Corsika v.6.2. It starts with the simulation of the primary cosmic rays interactions with the atmospheric nuclei and consequent secondary particles creation and propagation. The primary cosmic rays are originated inside the zenith range $0^o - 85^o$ and with an energy range per nucleon from 1 TeV to 100 PeV. QGSJET package [110] is used as generator of the development of hadronic interactions. The first step of the simulation gives the muons at the sea level from which they are propagated untill the CAN surface through the MUSIC (MUon SImulation Code) program [85].

4.2.2 Parameterized simulation

The parameterized simulation is based on parametric formulas [56] describing the characteristics of underwater muon events (flux, energy spectrum, multiplicity spectrum and radial distance from the bundle axis) in the range $(1.5 \div 5.0)$ km w.e. and up to 85° for the zenith angle. The formulas have been computed via a full Monte Carlo simulation, starting from CR interactions, using the HEMAS code [59] with DPMJET package [61] for the development of the hadronic showers. The used primary CR flux is described in §2.2. It is a model which reproduces the flux and the energy spectrum

MUPAGE generation parameters		
	Min	Max
Shower Multiplicity	1	100
Shower Energy (TeV)	0.02	500
Zenith angle (degrees)	95	180
Generation CAN features		
(referred to 5 lines detector)		
R_{CAN} (m)	511	
H_{CAN} (m)	585	
h_0 (m)	1890	

Table 4.1: Generation parameters set in the MUPAGE simulation and generation CAN features. R_{CAN} is the CAN ray, H_{CAN} the CAN height and h_0 the depth of the CAN upper surface.

of single and multiple muons as seen by the MACRO experiment [62]. The muons on the sea surface have been propagated with MUSIC down to 5.0 km w.e. For a more detailed description see chapter 2 where some results are shown. Using these parametric formulas an event generator (MUPAGE) has been developed [57] in order to generate underwater muon bundles on the CAN surface.

MUPAGE program was used as muon generator in the present thesis. The parameters of the atmospheric muon generation and the CAN features, referred to the considered 5 lines detector, are written in Tab. 4.1.

4.3 Tracking and Cherenkov light generation: *KM3*

KM3 is actually a suite of three different FORTRAN-90 programs designed to fulfill independent tasks. These programs are designed to be run in a step-by-step manner, with the output of one program being used as an input to the next, these programs are

- GEN : GEN is a program which simulates the generation of Cherenkov light by a particle in a given medium (ice, water), including light from any secondary particles. A complete GEANT [111] simulation is used at this step. GEN tracks the Cherenkov photons through space with wavelength-dependent absorption and scattering taken into account, recording the position, direction and arrival time of photons at spherical shells of various radii centered on the origin.

- HIT : This program creates the OM hit distributions for muon track segments
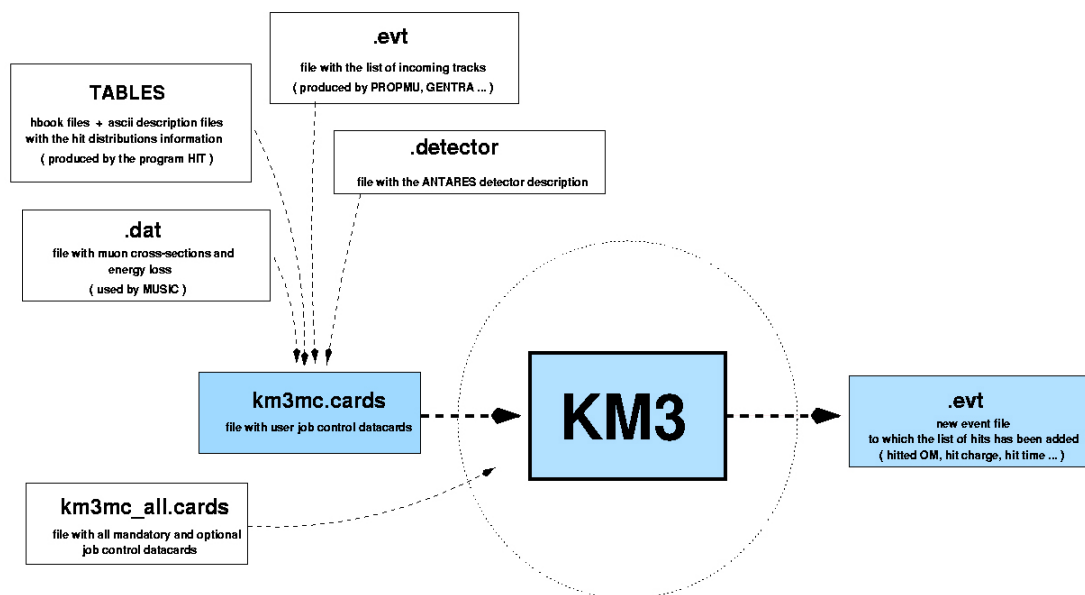
Figure 4.3: KM3MC program. Input/Output scheme.

and for electron showers. It uses the photon fields created by the GEN program. The outup of HIT is intended to be read and processed by KM3MC.

- KM3MC : It is a detector simulation program which uses the hit probability distributions generated in HIT along with a geometrical description of the detector to simulate events in the ANTARES detector. A special version of MUSIC [85] is used for muon tracking.

Both the GEN and HIT programs are run once only to generate the relevant tables of Optical Module hit probabilities. These tables are then stored on disk for subsequent use by KM3MC which is the program the end-user is most likely to use. Figure 4.3 shows a schematic view of the KM3MC program with its input and output data. The objects in the picture have the following meanings:

- .detector : A detector description file (*.detector), where the location and orientation of the strings, clusters and OMs is listed according to the ANTARES format [112].

- .evt : A file containing the list of muon tracks (*.evt) created by a generator program as Corsika or MUPAGE.

- .dat : Three files (*.dat) which are needed when running KM3MC using MUSIC. They contain the informations about the muon energy loss, angular deviation and cross sec-

tion in water.

- DATACARDS : datacards with which the user can set some parameter about the simulation.

- TABLES : These files are the output from HIT program.

The KM3MC output file is written in ascii format. This file contains all tags already present in the generator input plus some additional tags created by KM3MC.

4.4   Background simulation: SummaryTimeSliceWriter

As mentioned in §3.2.3 the (random) background in the ANTARES experiment is due to decays of radioactive isotopes in the sea water and bioluminescence. The radioactive decay can be simulated in a straight forward way as the decay rate can safely be assumed constant. The bioluminescence, however, results in rather erratic behaviour of the PMT count rate. Hits coming from the radioactive decay can be added to the MonteCarlo hits by the KM3 program also, neglecting the biological light sources. In order to take into account also the bioluminescence contribution to the background, the SummaryTimeSliceWriter program was used in the present analysis. The program takes the single rates of an ANTARES line from a user specified real run and it generates the count rates of all PMTs of the considered geometry. The Golden run (see §4.6) 28712 from July 2007 was chosen in the analysis. The output files of SummaryTimeSliceWriter is merged to the MonteCarlo data in the next program.

4.5   Trigger program: *TriggerEfficiency*

TriggerEfficiency simulates the ARS electronics, merges the background (from SummaryTimeSliceWriter program) to the MonteCarlo data and finally processes the data through the ANTARES software trigger (simultaneous triggers can be chosen). In order to do that, the ascii output of KM3 must be previously converted in ROOT format by the *MonteCarloEventWriter* program.

The MonteCarlo data are triggered in the same manner than the real ones (see §3.3). The data with a charge greater than a low threshold (tipically 0.3 pe) are called level 0 (L0) hits. The first level trigger, the so-called L1 trigger, is built up of coincidence hits in the same storey within a 20 ns time window, and optionally hits with a large

amplitude, defined as hits with a charge larger than a "*high threshold*" tuneable from 2.5 photo-electrons (p.e.) to 10 p.e. A trigger logic algorithm, which behaves like a level 2 trigger, is then applied to data and operates on level 1 hits. The main physics triggers are the majority logic trigger **3D** and the 3D-directional scan logic trigger **3N**. The majority logic trigger 3D processes all data and declares an event as soon as a minimum number [1] of (L1) hits are found within a 2.2 ms time interval. In addition, each pair of (L1) hits should verify the causality relation:

$$\Delta t_{ij} \leq \frac{d_{ij}}{c/n} + 20\,ns \tag{4.1}$$

where Δt_{ij} and d_{ij} are the time difference and the spatial distance between $(hit)_i$ and $(hit)_j$ respectively, c is the speed of light and n the index of refraction of the sea water. The trigger 3N applies the same logic trigger than 3D but with an extra scan of directions for which a 1D standard trigger [113] is applied. The 1D trigger implements a standard 1 dimensional trigger looking for time correlated hits from a muon in the given direction.

The generated output of TriggerEfficiency has the same characteristics than real raw data.

The real data sample analyzed in this thesis corresponds to a period in which the following trigger features were performed:
- High threshold = 3 p.e.;
- Trigger 3N.
TriggerEfficiency was used with the same characteristics for MonteCarlo data analysis.

4.6 Data samples

Atmospheric muons were simulated for the 5 lines ANTARES detector. The equivalent livetime corresponds to $687.5\,h$. The MonteCarlo programs used are the following: MUPAGE (see Tab. 4.1), KM3, MonteCarloEventWriter, SummaryTimeSliceWriter (background from run 28712), TriggerEfficiency (high threshold = 3 p.e., 3N trigger), BBbatch (see next section).

The real data sample is the Au selection [2] of June and July 2007. In the considered

---

[1] The minimum number of triggered hits is specified with a user selected option, usually set to 5.

[2] The Au selection (also named Golden Run Selection) is a sample of run with mainly the following characteristics: more than $4000\,s$ long, no missing informations in the file, lost time at runstart and runstop less than $100\,s$, muon rate more than 0.01 Hz and less than 10 Hz.

period a bug was found in the core of the trigger processor. The main effect can be summarised as a 20% loss of data. Considering the dead-time of the whole detector and the trigger bug, the livetime of the real data sample corresponds to $724\,h$.

4.7 Track reconstruction program: *BBbatch*

The BBfit strategy [114], implemented in the BBbatch track reconstruction program, is inspired by the MRECO reconstruction code [115]. The software version 3.2 is used in the analysis. The processing steps of the algorithm are described in the following:

- Hit grouping: a merging of hits in the same storey is done if their time difference $dt < 20\,ns$. The time of the earliest hit is taken into account and the charge signals are summed. In addition if the hit coincidence is in different OMs, a bonus charge of 1 photo electron (pe) is added.

- T3 selection: a selection of the previous hits is performed if the charge amplitude is $< 2.5\,pe$. Starting from the bottom of the line, the algorithm looks at next two storeys and a T3 cluster is considered if an hit is found in next floor within $\pm 80\,ns$ or in next-to-next floor within $\pm 160\,ns$. Only the first T3 hit for each storey is considered (i.e. maximum 1 per storey). The algorithm strategy requires at least 1 T3 cluster on one line to be used in the fit. The search of N T3 clusters is done in an exclusive way, so that one hit cannot belong to 2 triggered T3 clusters, which implies that a 2 T3 trigger requires 4 hits.

- Hit selection: Only lines containing T3s are considered. The hit selection starts from a search on the lowest storey containing a T3. Moving up and down to consecutive floors the earliest hit within time window $\pm(n * 80\,ns)$ within the considered floor and the nth floor (n^{th} with respect to the starting floor) is accepted. If a T3 hit is found in one of these floors, it is accepted. If a gap of two or more storeys is found the search is abandoned.

- Fitting: different fits are applied. Firstly a linear rough fit, whose extracted parameters are used as starting point for the next refined fits. The next fits are a track fit, which looks for a muon track and a bright point fit which looks for a point light source. The fits are based on a chi square minimization approach.

4. ANALYSIS DATA SAMPLE AND PROGRAMS

In the BBfit version 3.2 the detector geometry is not taken into account. This means that neither the orientation of storeys nor the line deviation is considered. Hit positions are thus set as the centre of the storey in the horizontal plane whereas their altitude corresponds to the optical modules altitude, by regarding the line as vertical.

Particular interest in the analysis is given to the quality parameters of the program. The quality parameters are quantities associated to any fitted track which can be used to select a subset of data with better fit conditions. The quality parameters used in the analysis are the next:

- *Nlines*: number of lines containing hits used in the fit algorithm;

- *Nstoreys*: number of storeys containing hits used in the fit algorithm;

- χ_t^2: normalized chi square relative to the track fit;

- χ_b^2: normalized chi square relative to the bright point fit.

Only the χ_t^2 of the track fit is here defined:

$$\chi_t^2 = \chi^2 / N_{dof} \tag{4.2}$$

where N_{dof} is the number of degrees of freedom of the fit and χ^2 is the chi square related to the track fit and defined as

$$\chi^2 = \sum_{i=1}^{N\,hit} \left[\frac{1}{\sigma^2} \left(t_{fit} - t_i \right)^2 + \frac{q_i\,d_{fit}}{q_0} \right] \tag{4.3}$$

$(t_{fit} - t_i)$ is the time difference between the hit time t_{fit}, as expected by the fitted track and the hit time t_i. $\sigma = 10\,ns$ and $q_0 = 50\,m\,p.e.$ are the free parameters of the fit and are tuned to the specified values. q_i represents the charge amplitude of the hit and d_{fit} is the travel distance of a direct Chernekov photon from the fitted track to the optical module.

Chapter 5

Data selection and study of the reconstruction algorithm

The reconstruction program represents a necessary tool for the analysis of the data. Some quality parameters provided by the reconstruction algorithm can be used to improve the purity of the data sample. In any case the unfolding algorithm, presented in the next chapter, takes into account the reconstruction errors. The smearing effects related to the track reconstruction must be studied in order to perform the unfolding of the data. In this chapter the ANTARES effective area for atmospheric muons as a function of the zenith angle is computed. This quantity is derived from the MonteCarlo simulations only. In the following a sequence of cuts on the reconstructed events, based on the reconstruction program, are defined. The cuts intend to select a data set with a higher purity, in particular concerning the reconstruction of the zenith angle. Finally some quantities needed in the unfolding analysis are defined and calculated.

5.1 ANTARES effective area for atmospheric muons

In this section the detector effective area for atmospheric muons is calculated from MonteCarlo. This quantity represents the hypothetical detector area with an ideal 100% trigger efficiency for the detection of atmospheric muon events. Such effective area depends from several muon bundle features as the zenith angle, energy and multiplicity. Here the given quantity is integrated over all the variables but the zenith angle.

The definition of the following quantities is given:
- $N_t^{MC}(cos(\theta_t))$: distribution of the generated MonteCarlo events as a function of the generated (true) zenith angle θ_t.

- $N_{trig}^{MC}(cos(\theta_t))$: distribution of the triggered MonteCarlo events as a function of the generated (true) zenith angle θ_t.

The "*trigger efficiency*" can now be defined as

$$\epsilon_{trig}(cos\theta_t) = N_{trig}^{MC}(cos\theta_t)/N_t^{MC}(cos\theta_t) \tag{5.1}$$

It represents the fraction of generated events which survive the trigger as a function of the generated zenith angle. It is shown in Figure 5.1. Using the trigger efficiency it is possible to compute the effective area for the atmospheric muons events as a function of the zenith angle. This quantity is defined as

$$A_{eff}(cos\theta_t) = \epsilon_{trig}(cos\theta_t) \cdot A_{CAN\perp}(cos\theta_t) \tag{5.2}$$

where $A_{CAN\perp}(cos\theta_t)$ is the generation CAN area as seen under zenith angle θ_t:

$$A_{CAN\perp}(cos\theta_t) = |\pi R_{CAN}^2 \cdot cos\theta_t + 2R_{CAN} \cdot H_{CAN} \cdot sin\theta_t| \tag{5.3}$$

R_{CAN} and H_{CAN} are the generation can parameters specified in the tab.4.1.

From MonteCarlo simulation the plot of Figure 5.2 has been obtained.

5.2 Cut selections based on the reconstrution algorithm

The quality parameters of the reconstruction program were defined in the previous chapter. In this section they are studied in order to select well reconstructed events, in particular concerning the zenith angle reconstruction.

5.2.1 Cut selection

The cuts are necessary to improve the purity of the data sample. The definition of purity is given in sec. 5.2.2

The events have been divided into the following two subsets:

- Single Line (SL) events: when the hits used in the reconstruction fit belong to only one line ($Nlines = 1$);

- Multiple Line (ML) events: when the hits used in the reconstruction fit belong to more than one line ($Nlines > 1$);

Figure 5.1: Efficiency at trigger level (see eq. 5.1 for its definition) Vs $cos\theta_t$.
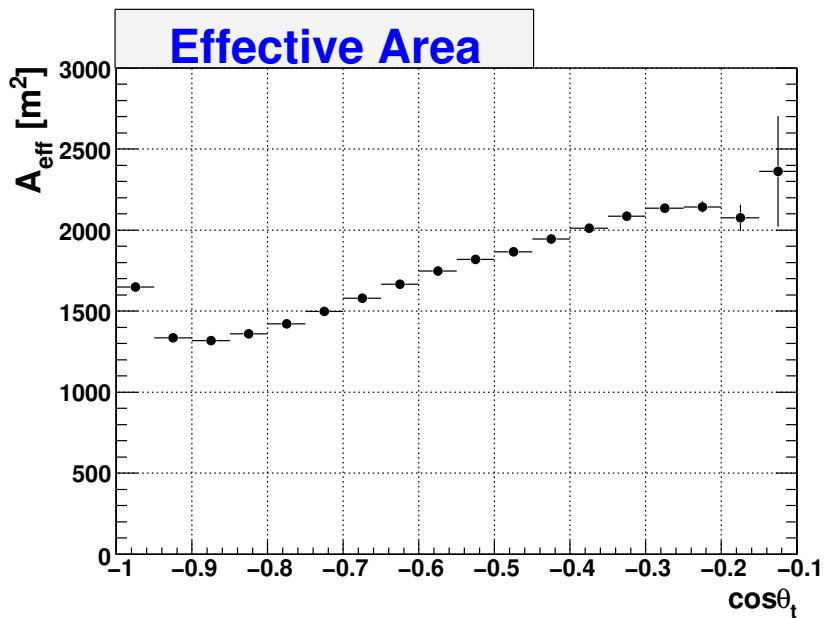
Figure 5.2: Effective area for atmospheric muons events (see eq. 5.2 for its definition) Vs $cos\theta_t$.
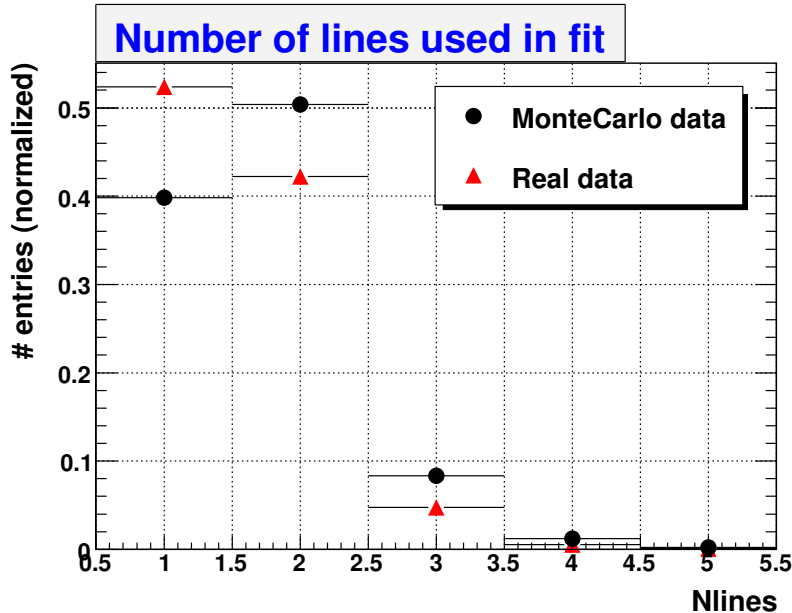
Figure 5.3: Distributions of the reconstruction algorithm quality parameter *Nlines* (defined in 4.7) for both MonteCarlo and Real reconstructed events.

	Real	MonteCarlo
SL	52.41	39.49
ML	47.59	60.51

Table 5.1: Percentages of Single Line (SL) and Multiple Line (ML) events of all reconstructed evetns for MonteCarlo and Real data.

The events detected with a single line usually have a well reconstructed zenith angle and a very bad reconstructed azimuth angle. A pre-selection of events detected with more than a line ($Nlines > 1$) is necessary if a good determination of the spatial angular direction is needed (for instance in the neutrino astronomy studies). The measurement of the Depth Intensity Relation is not strictly related with the azimuth angle and for this reason single line events are considered in this thesis.

In Figure 5.3 the fraction of events versus the number of line *Nlines* is plotted for both MonteCarlo and real data. The simulated data have a larger fraction of ML events with respect to the real ones. This is evident also in Tab. 5.1 where the fraction of ML and SL events are shown.

The reconstruction algorithm does not always converge toward a definite value of

Figure 5.4: SINGLE LINE EVENTS - Distributions of the reconstruction algorithm quality parameter *Nstoreys* (defined in 4.7) of SL events for both MonteCarlo and Real data after cut C1 (see text).

the fitting parameters. In this case the program sets the value of the reconstructed zenith angle cosine ($cos\theta_m$) equal to 1 or -1. These wrongly reconstructed events are removed by the following cut (referred as **C1**) for both ML and SL events:

$$\mathbf{C1} : cos\theta_m \neq \pm 1 \tag{5.4}$$

The second cut, applied to the remaining SL events only, is based on the number of detector storeys interested by the reconstructed event *Nstoreys* (defined in 4.7). The distribution of *Nstoreys* is shown in Figure 5.4 for both MonteCarlo and real data. The discrepancy between MonteCarlo and real data affects mainly the two lowest values (*Nstoreys* = 5 and *Nstoreys* = 6). It is probably due to some not well reproduced features in the background simulation. As described in 4.4, the noise is added to the MonteCarlo events by using the real background measured during a well defined real run. The run is chosen with similar background conditions to those of the real data set considered in the analysis. Despite that the data set covers a time range of two months and during this period some slight change in the noise conditions could be happened,

which can not be perfectly reproduced in the MonteCarlo.

In order to improve the SL data sample the second cut (**C2**) is defined as:

$$\mathbf{C2}: Nstoreys > 5 \quad \text{(only for SL events)} \tag{5.5}$$

The third cut is made, for both SL and ML events, using the parameter χ_t^2 (see sec. 4.7). In Figures 5.5 and 5.6 the distributions of this parameter are given for SL and ML events surviving cut C1 and C2. In order to improve the purity without loosing too many events the following cut is applied:

$$\mathbf{C3}: \chi_t^2 < 3 \tag{5.6}$$

A last cut is performed to the remaining SL and ML events through the parameter χ_b^2 (see sec. 4.7) which is plotted in Figures 5.7 and 5.8 for both SL and ML events. It is defined as in the following:

$$\mathbf{C4}: \chi_b^2 > 2 \tag{5.7}$$

5.2.2 Efficiency and purity

The efficiencies and the purities of the simulated and real data samples after the generic cut selection x are here defined. Consider a measured quantity obtained on a data sample containing N events. x define a fixed value of this quantity and is referred to as a cut on the N data sample. Naming $M(x)$ the number of events which survives the selection x, the $Efficiency(x)$ is defined as:

$$Efficiency(x) = M(x)/N \tag{5.8}$$

i.e. the fraction of events remaining after the cut x with respect to the number of events N. This quantity can be calculated for both MonteCarlo and real data.

The main parameter needed in the analysis presented in the next chapter is the zenith angle. For this reason the cuts are defined in order to increase the precision on the measurement of the zenith angle θ_m in MonteCarlo events. Considering MonteCarlo events, let $T(x, \Delta\theta)$ be a subset of the $M(x)$ sample ($T(x, \Delta\theta) \subseteq M(x)$) containing events with a reconstruction error on the zenith angle less than $\Delta\theta = \theta_m - \theta_t$. θ_m stands for measured (i.e. reconstructed) zenith angle and θ_t for true (i.e. MonteCarlo generated) zenith angle. The $Purity(x, \Delta\theta)$ is defined as

$$Purity(x, \Delta\theta) = T(x, \Delta\theta)/M(x) \tag{5.9}$$

Figure 5.5: **SINGLE LINE EVENTS AFTER C1+C2 CUT** - Distribution of the reconstruction algorithm quality parameter χ^2_t (defined in 4.7) for both MonteCarlo and Real data.
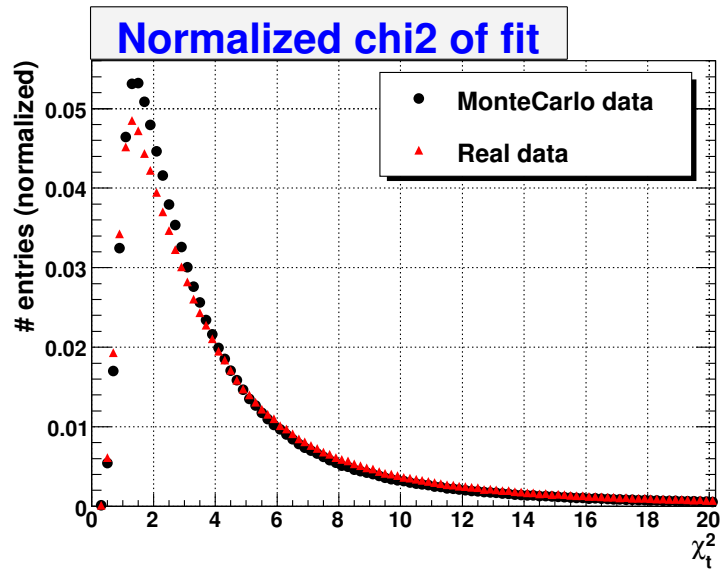
Figure 5.6: **MULTIPLE LINE EVENTS AFTER C1 CUT** - Distribution of the reconstruction algorithm quality parameter χ^2_t (defined in 4.7) for both MonteCarlo and Real data.
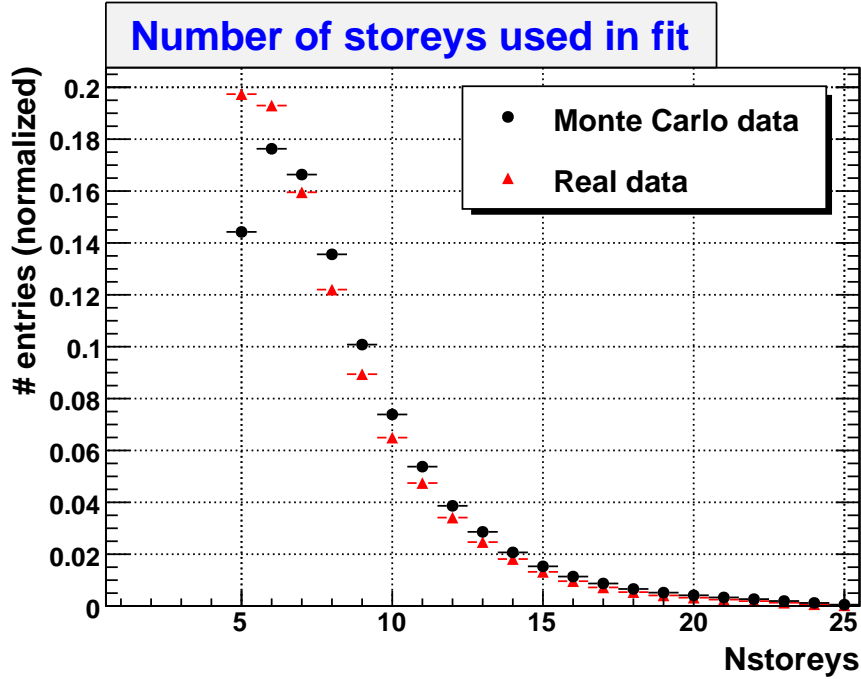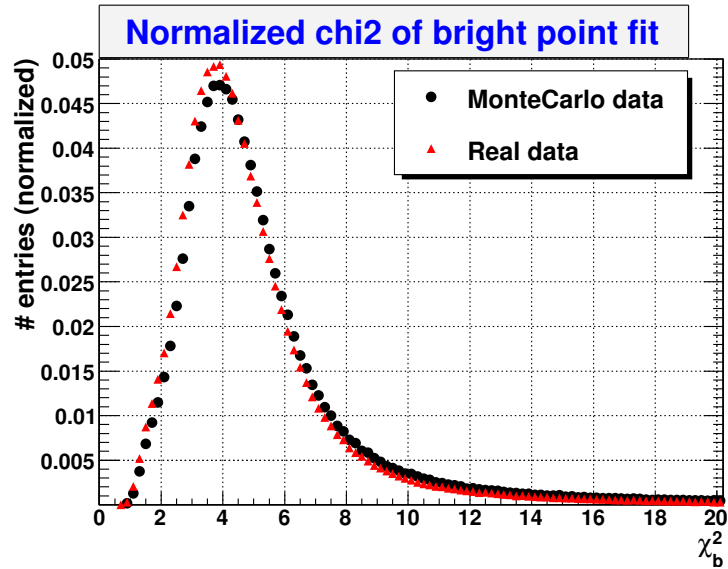
Figure 5.7: **SINGLE LINE EVENTS AFTER C1+C2+C3 cut** - Distribution of the reconstruction algorithm quality parameter χ_b^2 (defined in 4.7) for both MonteCarlo and Real data.
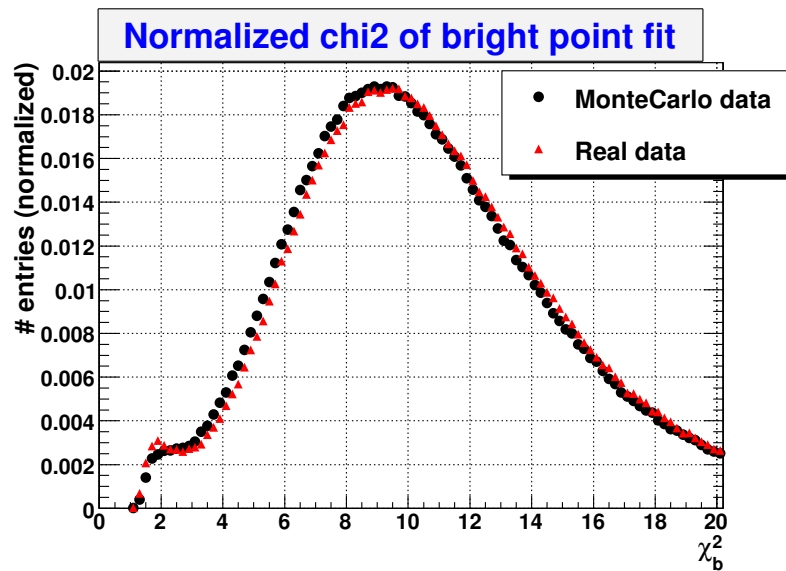
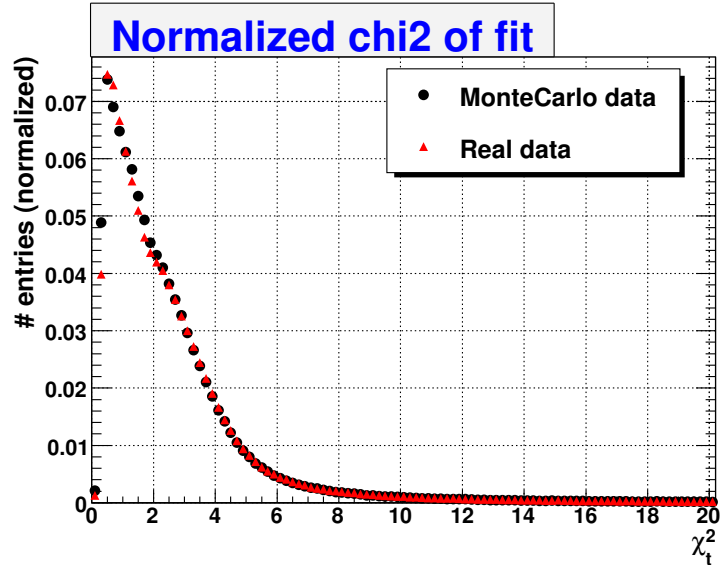**Figure 5.8:** **MULTIPLE LINE EVENTS AFTER C1+C3 cut** - Distribution of the reconstruction algorithm quality parameter χ_b^2 (defined in 4.7) for both MonteCarlo and Real data.

i.e. the fraction of events with a reconstruction error on the zenith angle less than $\Delta\theta$ with respect to the number of events $M(x)$ which survives the cuts. In the followings the value $\Delta\theta = 5^o$ is chosen.

5.2.3   Cut summary

In Tab. 5.2 and 5.3 the $Efficiency$ and the $Purity$ referred respectively to SL and ML events are shown after each performed cut. The $Efficiency$ and the $Purity$ of the whole data sample are reported in Tab. 5.4.

The unfolding procedure of the real data described in the following chapter is sensitive to the ratio of the number of MonteCarlo and real reconstructed events N^{MC}/N^{real}. As can be seen in Tab. 5.4 this ratio changes slightly depending on the applied quality cuts. This will be taken into account in the systematic uncertainties of the final result in §6.3.

In Figures 5.9 and 5.10 the reconstruction rates as a function of $cos\theta_m$ for both MonteCarlo and real data before the cuts defined in sec. 5.2.1 and after the cuts are shown.

The Figures 5.11, 5.12 and 5.13 show the reconstruction error for zenith and azimuth angles.

5.3   The Response Matrix (RM)

The *"response matrix"* and other quantities necessary for the computation of the DIR are derived in this section. The response matrix contains several information inferred by the MonteCarlo simulation as the fraction of events remaining after the quality cut over the number of events generated by the MonteCarlo program and the smearing of the reconstruction program (the physical reconstructed quantities can have some statistics error). The matrix itself is applied to the real data in the deconvolution method described in the next section, in order to retrive the unknown physical quantity from the measured one.

Consider the MonteCarlo simulation of atmospheric muons. The quantity

$$N_t^{MC}(cos(\theta_{tj})) \quad j = 1,...,T \;\; (T = 18) \tag{5.10}$$

(subscript "t" stands for *true*) represents the distribution of the generated (true) zenith angles. The range of this MonteCarlo distribution goes from vertical down-

	Efficiency(%) Real data	Efficiency(%) MonteCarlo data	Purity(%) MonteCarlo data
No cut	100.00	100.00	53.05
$cos\theta_m \neq \pm 1$	98.70	98.62	53.36
$Nstoreys > 5$	79.22	84.39	55.04
$\chi_t^2 < 3$	55.62	60.47	67.69
$\chi_b^2 > 2$	53.30	58.49	69.82

Table 5.2: SINGLE LINE EVENTS. Efficiencies and Purities. The cuts are performed in sequence.

	Efficiency(%) Real data	Efficiency(%) MonteCarlo data	Purity(%) MonteCarlo data
No cut	100.00	100.00	68.52
$cos\theta_m \neq \pm 1$	100.00	100.00	68.52
$\chi_t^2 < 3$	46.08	49.88	84.03
$\chi_b^2 > 2$	45.68	49.55	84.57

Table 5.3: MULTIPLE LINE EVENTS. Efficiencies and Purities. The cuts are performed in sequence.

	Efficiency(%) Real data	Efficiency(%) MonteCarlo data	Purity(%) MonteCarlo data
No cut	100.00	100.00	62.36
$cos\theta_m \neq \pm 1$	99.32	99.45	62.54
$Nstoreys > 5^*$	89.11	93.78	63.69
$\chi_t^2 < 3$	51.08	54.10	76.75
$\chi_b^2 > 2$	49.67	53.11	78.10

Table 5.4: ALL EVENTS. Efficiencies and Purities. The cuts are performed in sequence. *$Nstoreys > 5$ applied only on SL events.
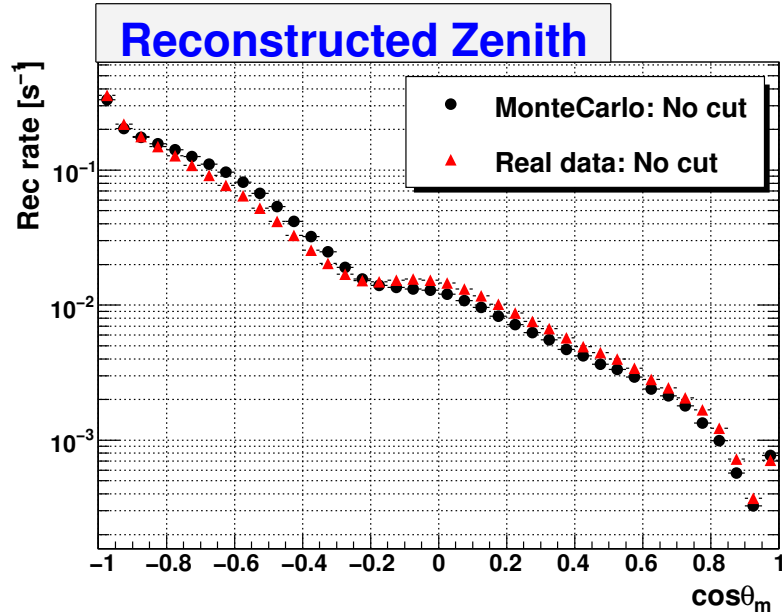
Figure 5.9: Reconstruction rate Vs cosine of reconstructed zenith angle θ_m before cuts. Reconstruction rates - MonteCarlo data: $1.82\,s^{-1}$. Real data: $1.75\,s^{-1}$
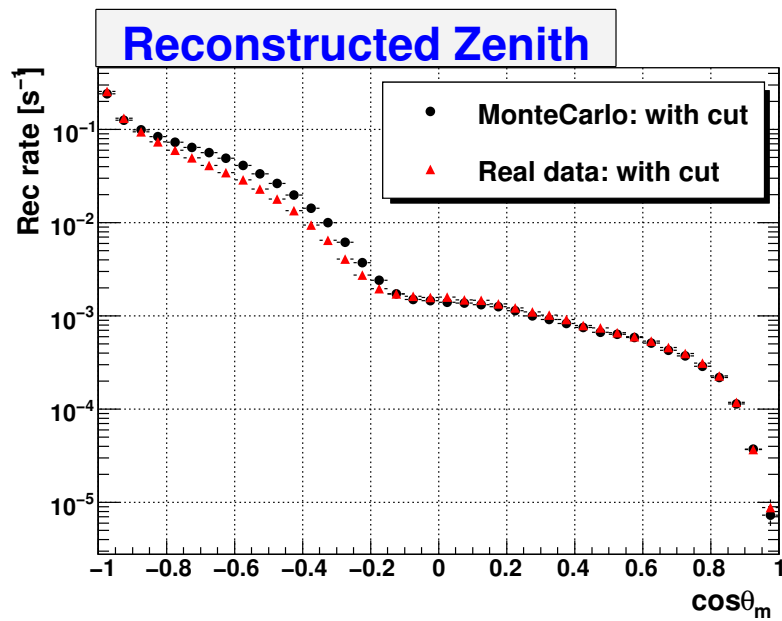
Figure 5.10: Reconstruction rate Vs cosine of reconstructed zenith angle θ_m after the cuts defined in sec. 5.2.1. Reconstruction rates - MonteCarlo data: $0.97\,s^{-1}$. Real data: $0.87\,s^{-1}$
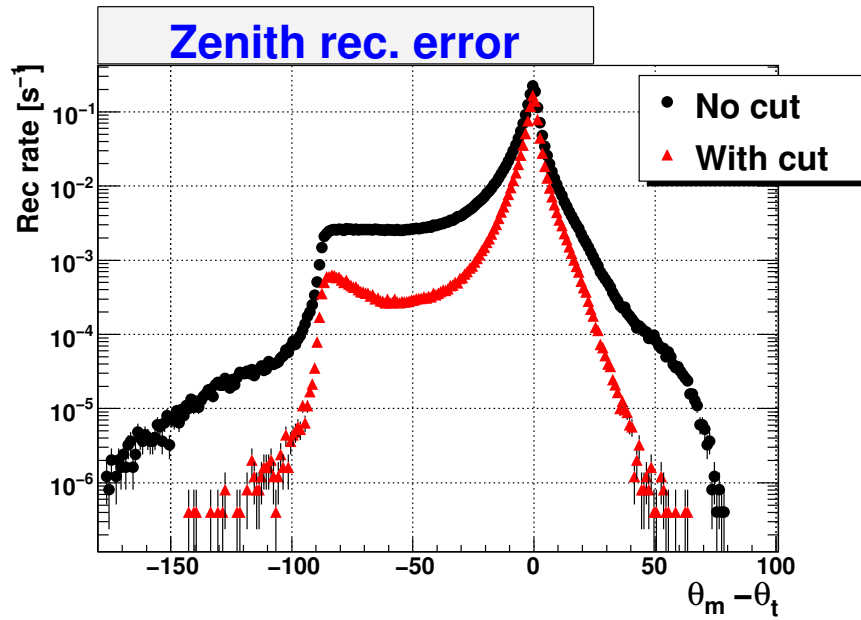
Figure 5.11: Difference between reconstructed and generated (MonteCarlo) zenith angles
before and after cuts.
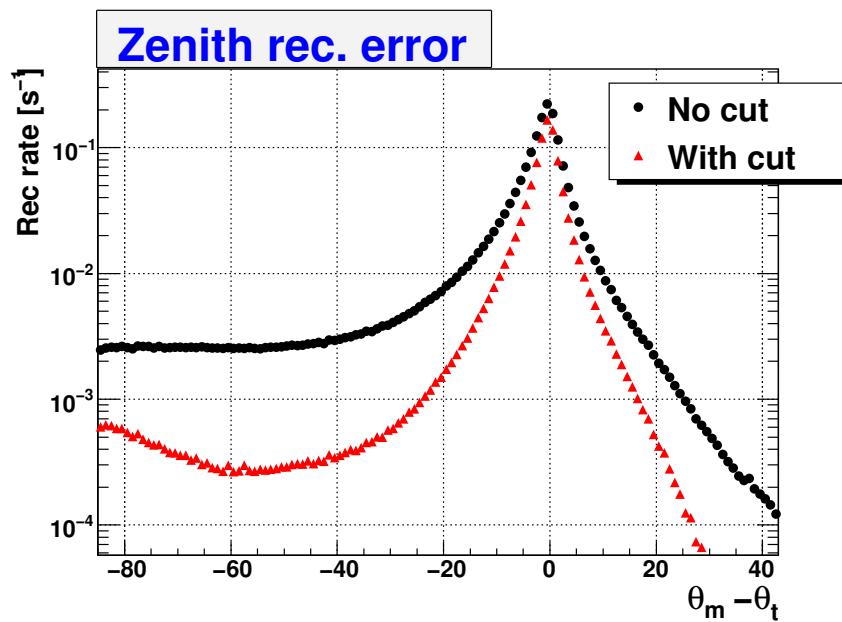
Figure 5.12: Difference between reconstructed and generated (MonteCarlo) zenith angles
before and after cuts. This Figure shows a restricted region of the Figure 5.11
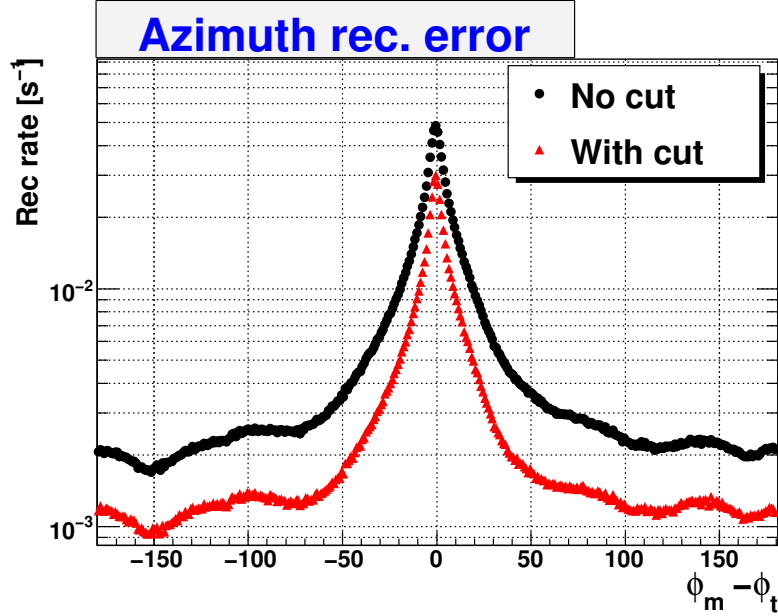
Figure 5.13: Difference between reconstructed and generated (MonteCarlo) azimuth angles before and after cut.

ward going events to almost horizontal events $-1 \leq cos(\theta_t) \leq -0.1$. The quantity $\mathbf{t} \equiv (N_t^{MC}(cos(\theta_{t1})), ..., N_t^{MC}(cos(\theta_{tT})))$ represents the vector containing the T values of this binned distribution.

Figure 5.10 shows the MonteCarlo generated events which were triggered by the software trigger and reconstructed. In addition, they survived also the cuts defined in the previous section. The plot represents the distribution of the reconstructed zenith angles

$$N_m^{MC}(cos(\theta_{mi})) \qquad i = 1, ..., M \ \ (M = 40) \tag{5.11}$$

of survived events, where the subscript "m" stands for *measured*. The quantity $\mathbf{m} \equiv (N_m^{MC}(cos(\theta_{m1})), ..., N_m^{MC}(cos(\theta_{mM})))$ represents the vector containing the M values of this distribution. Due to the smearing effects of the reconstruction algorithm, a wider range can be seen here with respect to the "true distribution" defined in eq. 5.10, going from vertical downward going event to vertical upward going event $-1 \leq cos(\theta_m) \leq 1$ $(M > T)$.

The transformation of a *true* distribution into the *measured* one is called "*data*

convolution":

$$N_t^{MC}(cos(\theta_{ti})) \ \ j = 1, ..., T = 18 \longrightarrow (convolution) \longrightarrow N_m^{MC}(cos(\theta_{mj})) \ \ i = 1, ..., M = 40 \tag{5.12}$$

From the detector simulation instead of $N_t^{MC}(cos(\theta_{ti})) \ j = 1, ..., T$ what is ontained is the binned distribution of measured (i.e. reconstructed) values $N_m^{MC}(cos(\theta_{mj})) \ i = 1, ..., M$. The two vectors **t** and **m** are linked each other by the matrix, denoted as *"response matrix"*, **R** with size $M \times T$:

$$\mathbf{m = Rt} \tag{5.13}$$

$$m_i = \sum_{j=1}^{T} R_{ij} t_j \quad i = 1, ..., M \tag{5.14}$$

The *response matrix R* has the simple interpretation as a conditional probability:

$$R_{ij} = P(observed \ in \ bin \ i \mid true \ value \ in \ bin \ j) \tag{5.15}$$

For example the fourth column

$$R_{i4} = P(observed \ in \ bin \ i \mid true \ value \ in \ bin \ 4) \tag{5.16}$$

gives the probability that an event generated with a value belonging to the fourth bin of the distribution, is measured with a value belonging to the ith bin. In Figure 5.14 it is shown the values of R_{i4} for $i = 1, ..., M = 40$ of the response matrix. As expected the highest value is for the fourth bin whose value represents 51% of the distribution integral.

By summing R_{i4} over all possible bins of the observed values i we get the probability that an event generated in the bin 4 survives both the trigger and the reconstruction level. For each true bin j this probability can be written as in the following

$$\epsilon_j \equiv \sum_{i=1}^{M} R_{ij} = P(observed \ anywhere \mid true \ value \ in \ bin \ j) \tag{5.17}$$

This defines what is called the *"global efficiency"*, $\epsilon_j \equiv \epsilon(cos(\theta_{tj}))$, that is the probability that a true event generated with zenith angle $cos\theta_t \in$ bin j is both triggered and reconstructed:

$$\epsilon(cos\theta_t) = N_m^{MC}(cos\theta_t)/N_t^{MC}(cos\theta_t) \tag{5.18}$$
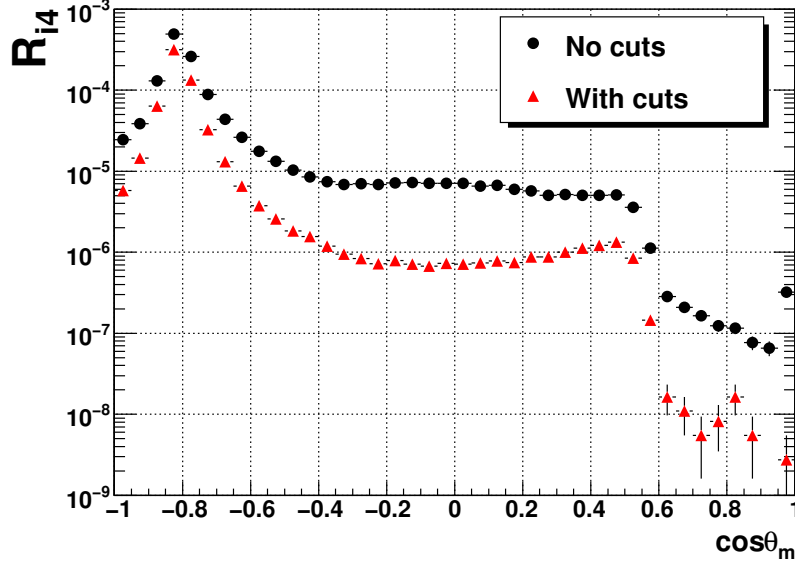
Figure 5.14: Histograms with values of the R_{i4} response matrix with and without cuts. As expected the fourth bin has the highest value which represents 51% of the distribution integral.

The global efficiency can be written as the product of two efficiencies: the "trigger efficiency" (defined in sec. 5.1 and shown in Figure 5.1) and the "reconstruction efficiency". The latter is defined as:

$$\epsilon_{rec}(cos\theta_t) = N_m^{MC}(cos\theta_t)/N_{trig}^{MC}(cos\theta_t) \tag{5.19}$$

The reconstruction efficiency ϵ_{rec} represents the fraction of triggered events which are reconstructed as a function of the generated zenith angle.

In the same way the purity P_j can be defined as

$$P_j \equiv R_{jj}/\epsilon_j \tag{5.20}$$

where $P_j \equiv P(cos\theta_{tj})$ is the fraction of events that have been reconstructed in the right bin j above the reconstructed events generated with $\theta_t \in$ bin j.

As can be seen from the previous formulas, the purity and the efficiencies are only computable from MonteCarlo simulations because they are referred to the true zenith angle, which in the real data is not known. In the Figure 5.15 the reconstruction
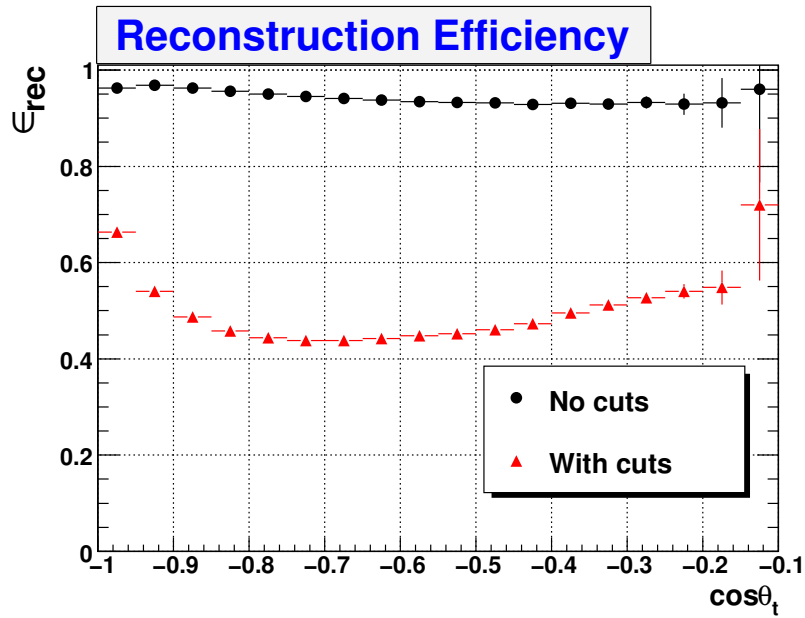
Figure 5.15: Efficiency with and without cuts at reconstruction level (see eq. 5.19 for its definition) Vs $\cos\theta_t$.
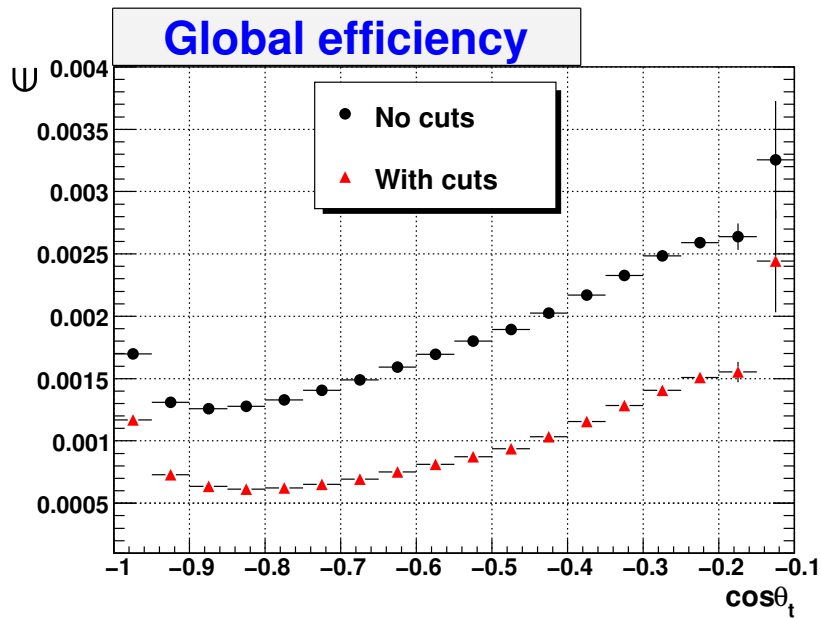
Figure 5.16: Global efficiency with and without cuts (see eq. 5.18 for its definition) Vs $\cos\theta_t$.
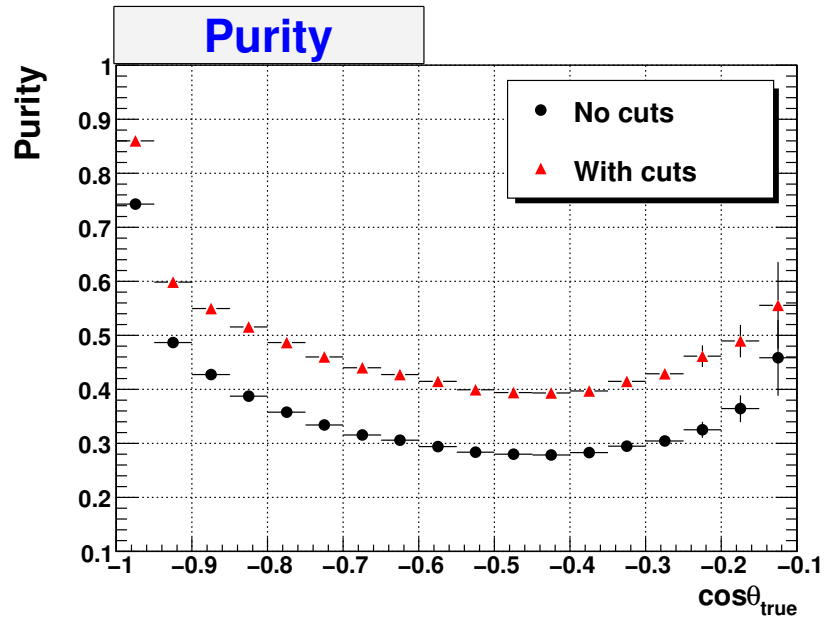
Figure 5.17: Purity with and without cuts (see eq. 5.20 for its definition) Vs $\cos\theta_t$.

efficiency just defined is shown as a function of $\cos\theta_t$. The global efficiency and the purity are plotted in the Figures 5.16 and 5.17.

Chapter 6

Measurement of the Depth Intensity Relation with 5 lines

The study of the Depth Intensity Relation (DIR) corresponds to the measurement of the flux of the vertical atmospheric muons Vs slant depth. Its knowledge would provide informations on the primary cosmic ray flux and on the interaction models. In this chapter the deconvolution procedure used to get the interesting physics quantites from the experimental data is explained. The derivation of the DIR and of the atmospheric muon flux (for $E_\mu > 20\,GeV$) at a fixed sea depth as a function of the zenith angle is shown. Finally the systematic uncertainties are estimated.

6.1 Computation of Depth Intensity Relation

One method to derive the DIR is to compute the muon flux $I_{h_0}(\theta)$ as a function of the zenith angle θ at a fixed vertical depth h_0 in the sea. Once this distribution is known, it can be transformed into the DIR using the relation [116]:

$$I(\theta = 0^o, h) = I_{h_0}(\theta) \cdot cos(\theta) \cdot c_{corr}(\theta) \quad [s^{-1} \cdot cm^{-2} \cdot sr^{-1}] \qquad (6.1)$$

where $h = h_0/cos\theta$ is the *slant depth*, i.e. the distance covered in the sea water by muons to reach the vertical depth h_0 at zenith angle θ. In the following $h_0 = 1890\,m$ is the sea depth of the top ANTARES can area (i.e. the upper ANTARES can surface used in the simulation). The equation 6.1 is referred to *"verticalization of the flux"*: it transforms the muon flux $I_{h_0}(\theta)$ as a function of the zenith angle θ at the fixed depth h_0 into the flux $I(\theta = 0^o, h)$ of the vertical muons ($\theta = 0^o$) as a function of the sea

Figure 6.1: Average muon bundle multiplicity $\overline{m}_{h_0}(\theta)$ ($h_0 = 1890m$). **From Monte-
Carlo**. Only statistical errors.

depth h. The $cos\theta$ and the $c_{corr}(\theta)$ factors are needed in order to take into account the
zenith angle dependence of the atmospheric muon flux at sea level [84; 116]. [1]

Unfortunately the computation of the flux of eq. 6.1 is not simple. Only events
(bundle of muons with multiplicity m) are detected from the real data and no informa-
tions about their multiplicity is available. What can be known from the experimental
data is the event flux $\Phi_{h_0}(\theta)$ at the fixed depth h_0. The only way to derive the muon
flux $I_{h_0}(\theta)$ from the event flux $\Phi_{h_0}(\theta)$ is through the MonteCarlo computation of the
average event multiplicity $\overline{m}_{h_0}(\theta)$ at the depth h_0. This quantity is plotted in Figure
6.1 as a function of the zenith angle. With this quantity the following relation can be
written

$$I_{h_0}(\theta) = \Phi_{h_0}(\theta) \cdot \overline{m}_{h_0}(\theta) \tag{6.2}$$

Also the event flux $\Phi_{h_0}(\theta)$ at the fixed depth h_0 is not directly inferred from the
data deconvolution. What is get by the deconvolution procedure (explained in the

---

[1]The sea level flux has a zenith angle dependence $\propto 1/(cos\theta \cdot c_{corr}(\theta))$ where the corrective factor
is needed to take into consideration the Earth curvature. It can be considered equal to 1 for zenith
angle $\theta < 60^o$. Because in ANTARES the angles are measured with respect to the nadir direction, this
corresponds to zenith angle direction $\theta > 120^o$.
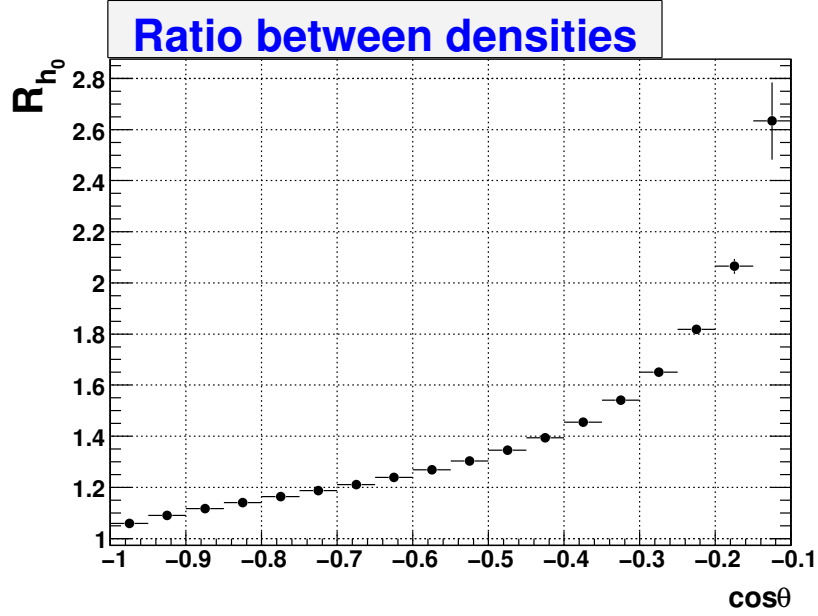
Figure 6.2: $R_{h_0}(\theta)$ (see eq. 6.4 for its definition). **From MonteCarlo**. Only statistical errors.

next section) is the event flux $\Phi(\theta)$ considering the events spread all over the detector surface area which is at variable depth. Lower is the sea depth considered, larger is the flux of the events: the flux calculated in the whole detector surface area is lower with respect to the flux calculated in the same area at the depth of the top surface. A correction factor is needed in order to get the event flux on the top of the can $\Phi_{h_0}(\theta)$ from the event flux on the whole can area $\Phi(\theta)$. This quantity $R_{h_0}(\theta)$ is introduced in the following equation:

$$\Phi_{h_0}(\theta) = \Phi(\theta) \cdot R_{h_0}(\theta). \tag{6.3}$$

$R_{h_0}(\theta)$ is computed from MonteCarlo simulations. It represents the ratio between the density of the generated events on the top of the can $\rho_{h_0}(\theta)$ and the density of all generated events on the whole can area $\rho(\theta)$:

$$R_{h_0}(\theta) = \frac{\rho_{h_0}(\theta)}{\rho(\theta)} = \frac{N_{h_0}(\theta)/A_{top\perp}(\theta)}{N(\theta)/A_{can\perp}(\theta)} \tag{6.4}$$

where:

- $A_{can\perp}(\theta)$: can area as seen under true zenith angle θ (defined in 5.3);

- $A_{top\perp}(\theta) = |\pi R_{can}^2 \cdot cos\theta|$: top can area as seen under true zenith angle θ;

- $N(\theta)$: distribution of the events generated on the whole can as a function of the true zenith angle θ;

- $N_{h_0}(\theta)$: distribution of the events generated on the top of the can ($h = h_0$) as a function of the true zenith angle θ.

In Figure 6.2 the quantity computed from a MUPAGE simulation is shown.

6.2 Data unfolding

The knowledge of the event flux $\Phi(\theta)$ arises from the application of the unfolding algorithm that is presented in this section.

What we know from the real data is the zenith distribution $N_m^{Real}(\theta_m)$ relative to the reconstructed muon events which have been selected after the cuts (see sec. 5.2.1). The deconvolution procedure is a method to derive a true distribution from a measured one. In this particular case the goal is to transform the real data distribution $N_m^{Real}(\theta_m)$ into its parent angular distribution $N^{Real}(\theta)$:

$$N_m^{Real}(\theta_m) \longrightarrow (deconvolution) \longrightarrow N^{Real}(\theta) \tag{6.5}$$

This is possible using the MonteCarlo simulations of the detector response, that is the response matrix.

From relation 5.13 it seems that it would be possible to recover the original true distribution by inverting the response matrix and by applying it to the experimental data. In principle with infinite statistics this would be possible. Unfortunately in the experimental data there are always statistical fluctuations between bins and a simple matrix inversion will keep also the statistical bumps in the true distribution.

It exists several methods to unfold data. In this thesis a Bayesian approach has been chosen, which consists in an iterative method proposed by D'Agostini [117] containing elements of Bayesian statistics. A brief explanation of the algorithm is given. For more details refer to the article mentioned above.

6.2.1 The Bayesian algorithm

The starting point of the algorithm is the definition of a set of initial probabilities $\mathbf{p} = (p_1, ..., p_T)$ for a measured event to be found in each true bin. The vector $\mathbf{w} \equiv$

$(N^{Real}(\theta_1), ..., N^{Real}(\theta_T))$ contains the T values of the unfolded binned distribution. In the absence of further information one can take $p_j = 1/T$ for bins of equal size. Initial estimator for $\mathbf{w}$ is

$$\hat{\mathbf{w}}_0 = n_{tot}\mathbf{p}_0, \tag{6.6}$$

where $n_{tot} = \sum_{i=1}^{M} n_i$, with $n_i \equiv \sum_{i=1}^{M} N_m^{Real}(\theta_{mi})$ is the total observed number of entries. These estimators are updated using the rule

$$\hat{w}_j = \frac{1}{\epsilon_j} \sum_{i=1}^{M} P(true\ value\ in\ bin\ j \mid found\ in\ bin\ i)\, n_i = \frac{1}{\epsilon_j} \sum_{i=1}^{M} \left(\frac{R_{ji}p_j}{\sum_k R_{ik}p_k} \right) n_i \tag{6.7}$$

R_{ji} is the element of the response matrix defined in eq. 5.15. Here Bayes' theorem has been used to write the conditional probability that an event was originated in bin j, given that it was observed in bin i, in terms of the response matrix R and the prior probabilities $\mathbf{p}$.

The updated estimator can then be compared to that of the previous iteration. This is done for example using a χ^2 test. If the χ^2 is too large, the procedure can be iterated with the new prior probabilities taken as the solution at the previous step, i.e. $\mathbf{p}_k = \hat{\mathbf{w}}_k/n_{tot}$. In practice this is found to converge to a reasonable solution in several iterations. The number of iterations should be decided upon before looking at the actual data, for example by using Monte Carlo test data. Continuing to iterate brings increasingly large variances and the estimators eventually approach the oscillating solution from matrix inversion. As the procedure uses Bayes' theorem in an intermediate step it has been called a *"Bayesian method"*.

Once $\hat{\mathbf{w}}$ is calculated, the distribution $N^{Real}(\theta)$ is known. This distribution represents the number of muon events at can level unfolded by the measured real data. It is now possible to compute the muon event flux at can level $\Phi(\theta)$ needed in eq. 6.3 using the relation

$$\Phi(\theta) = \frac{N^{Real}(\theta)}{\Delta T \cdot \Delta\Omega \cdot A_{can\perp}(\theta)} \tag{6.8}$$

where ΔT is the equivalent livetime of the considered real data sample defined in §4.6, $\Delta\Omega$ is the solid angle and $A_{can\perp}(\theta)$ the same defined in eq.5.3.

Finally it is possible to derive the atmospheric muon flux $I_{h_0}(\theta)$ at the fixed depth h_0 of equation 6.2 substituting the quantities defined in the above. Substituting the

expression of the flux into the relation 6.1 the DIR can be finally written as in the following

$$I(\theta = 0^o, h) = \frac{N^{Real}(\theta) \cdot \overline{m}_{h_0}(\theta) \cdot R_{h_0}(\theta)}{\Delta T \cdot \Delta\Omega \cdot A_{can\perp}(\theta)} \cdot |cos(\theta)| \cdot c_{corr}(\theta) \quad [s^{-1} \cdot cm^{-2} \cdot sr^{-1}] \quad (6.9)$$

where the quantities in the equation are the followings:

- $\Delta T = 3.26 \cdot 10^6\, s$ is the livetime of the considered real data sample.

- $\Delta\Omega = 2\pi \cdot 0.05\, sr$ is the solid angle subtended by two adjacent zenith angle bins.

- $A_{can\perp}(\theta)$ is the generation CAN area as seen under zenith angle θ. It is defined in eq. 5.3 and shown in Figure 6.3.

- $N^{Real}(\theta)/\Delta T$, representing the number of muon events reaching the generation CAN surface per second is shown in Figure 6.4 with the MUPAGE simulation curve superimposed.

- $m_{h_0}(\theta)$ is the average muon bundle multiplicity at the fixed sea depth $h_0 = 1890\, m$. This quantity is shown in Figure 6.1.

- $R_{h_0}(\theta)$ is the factor defined in eq. 6.4 and presented in Figure 6.2.

- c_{corr} is the correction factor c_{corr} [84; 116] defined in sec. 6.1. It is shown in Figure 6.5

6.3 Estimation of systematic uncertainties

The sensitivity of the results to the MonteCarlo simulations and to the cut performed to the data set is estimated in this section.

During MC simulation several input parameters are required to define the environmental and geometrical characteristics of the detector. Some of them play a role as sources of systematic uncertainties. In [118] the effect of water absorption length and of PMT efficiency on the muon reconstructed track rate is considered. Arranging by $\pm 10\%$ the reference values of absorption length, an almost negligible effect on the shape of the zenith distributions was noticed, while the absolute flux changed by $+25\%/-20\%$. Decreasing the PMT efficiency by 10%, considering the official Hamamatsu values, a decrease of about 15% was observed in the muon flux. Finally, the effect of the maximum angle between the PMT axis and the Cherenkov photon direction allowing light collection was considered. Summing in quadrature the different contributions, a global systematic effect of about $\pm 30\%$ can be considered as an estimate of the errors produced by uncertainties on environmental and geometrical parameters.

The obtained results is dependent also by the quality cut performed to the data set. The unfolding algorithm in fact is dependent by the relative ratio of MonteCarlo and real data. As seen in the previous chapter, the selection made on the events has different effects on the two data sets. The fraction of events remaining after the defined cuts is lower in real data than in MonteCarlo data. A different choise of the quality cut could give a different result. In order to take into account this source of systematic uncertainty the unfolded DIR $I^*(\theta = 0^o, h)$ has been obtained without considering any cut but the C1 (see sec. 5.2.1) which eliminates only not fitted tracks. The relative difference $K(h)$ between the two final fluxes

$$K(h) = \frac{I^*(\theta = 0^o, h) - I(\theta = 0^o, h)}{I(\theta = 0^o, h)} \tag{6.10}$$

is considered as a systematic uncertainty. This is dependent by the slant depth and is shown in in Figure 6.6.

This uncertainty is summed with the 30% estimated in [118] to get the final systematic estimation.

In Figure 6.7 the muon flux $(E_\mu > 20\,GeV)$ $I_{h_0}(\theta)$ at 1890 m depth is plotted with its systematic uncertainties. In Figure 6.8 the DIR $I(\theta = 0^o, h)$ is shown with systematic uncertainties together with other indipendet analysis of ANTARES data. The MonteCarlo simulation from MUPAGE is also present. The results are in good agreement within the uncertainties.
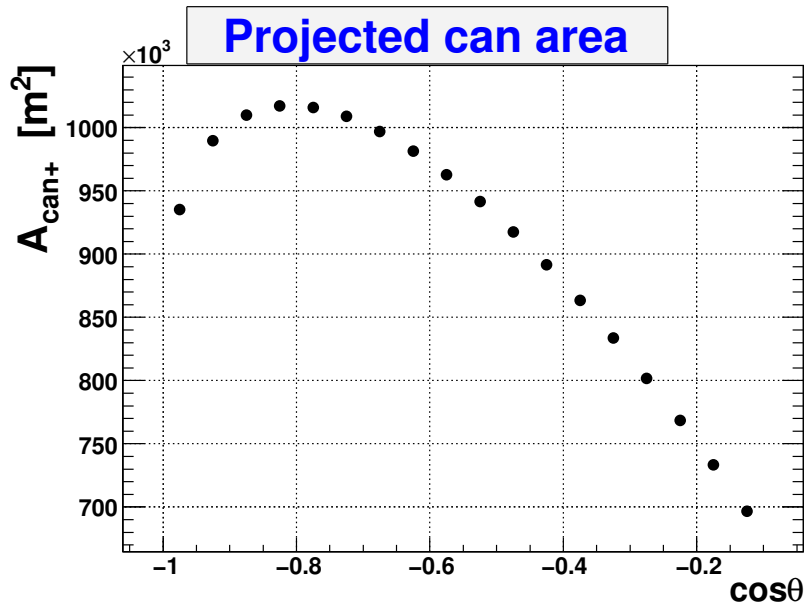
Figure 6.3: Area of the generation CAN (see sec. 4.1) as seen under zenith angle θ. No correlated errors considered. **From MonteCarlo**.
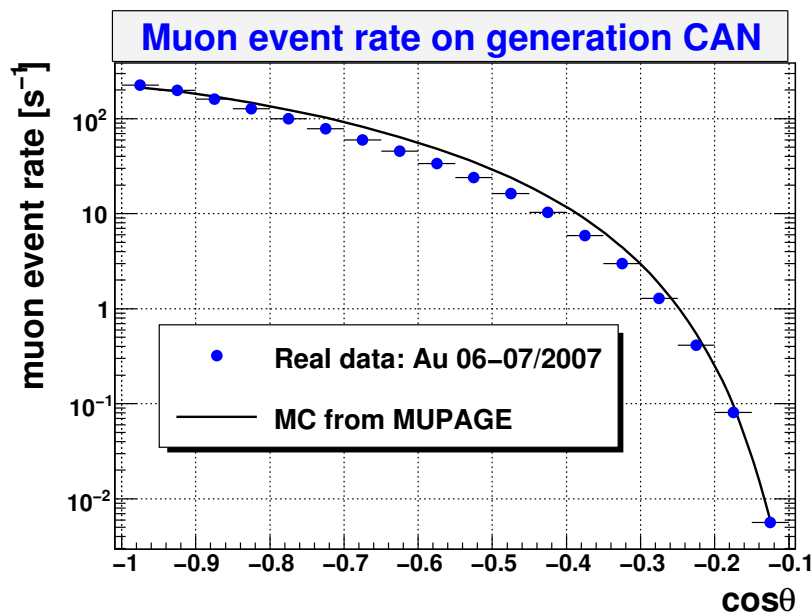
Figure 6.4: Number of muon events reaching the generation CAN surface per second. The MUPAGE simulation curve is superimposed.
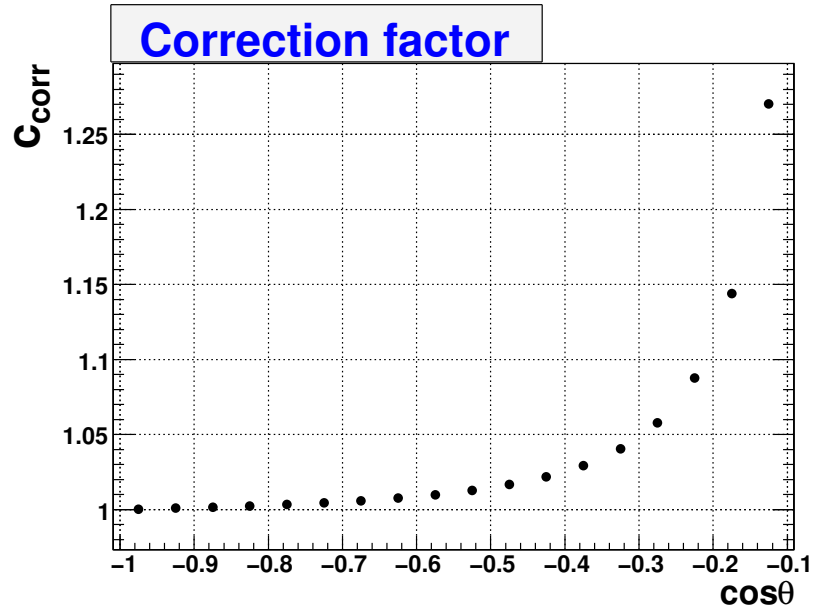
Figure 6.5: Correction factor c_{corr} [84; 116] defined in sec. 6.1. No correlated errors considered.
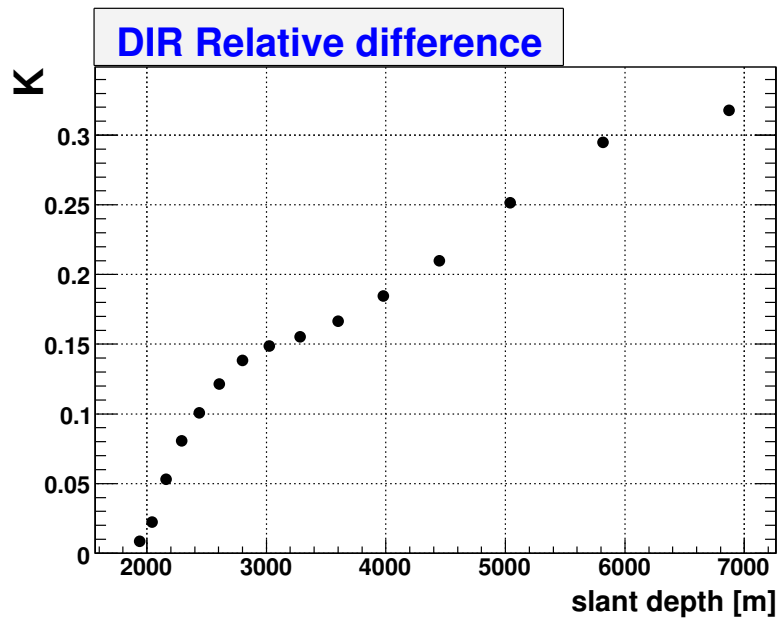
Figure 6.6: Relative difference between the flux obtained with the defined quality cuts and without quality cuts.
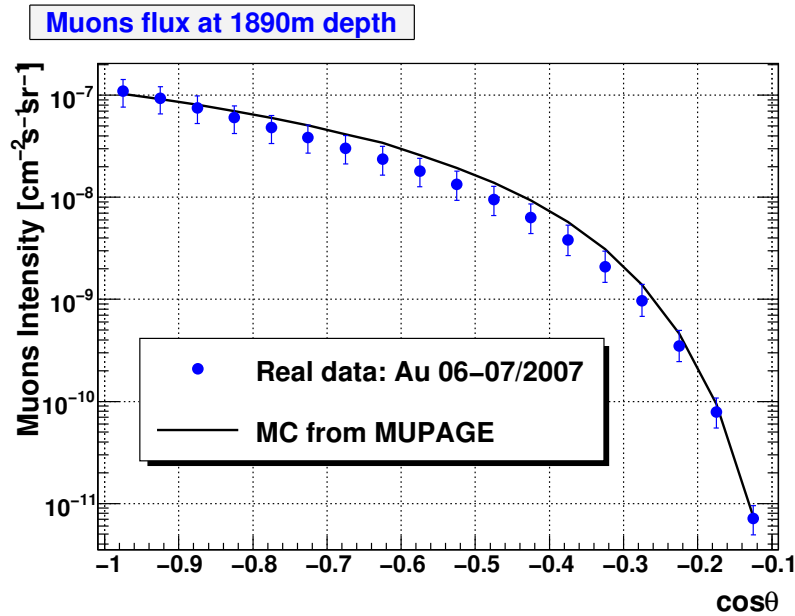
Figure 6.7: Atmospheric muons flux at 1890m of sea depth $(I_{h_0}(\theta))$ with systematic uncertainties. The flux resulting from a MUPAGE simulation is superimposed.
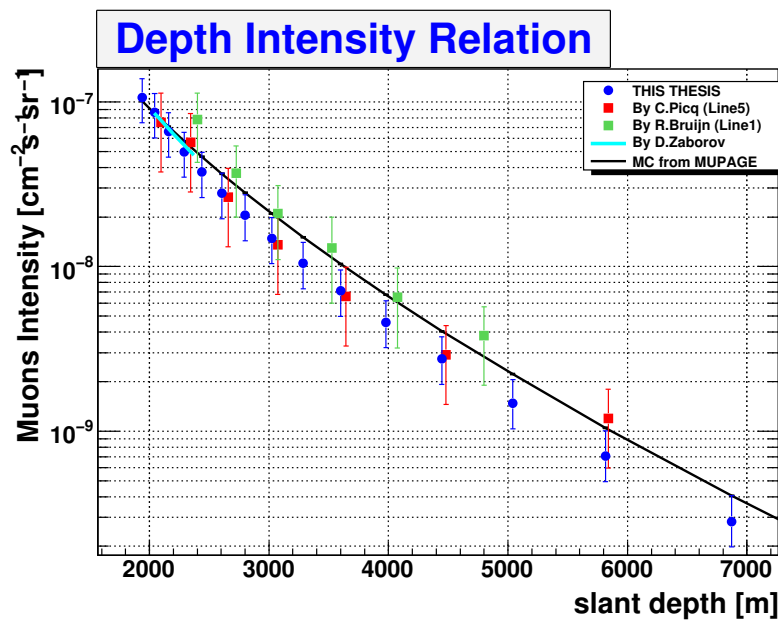
Figure 6.8: Depth Intensity Relation of atmospheric muons. Indipendent analysis from ANTARES data are shown with the MonteCarlo simulation by MUPAGE. R.Bruijn [96],

Chapter 7

Summary and conclusions

ANTARES is at present the largest Cherenkov neutrino observatory in the Northern hemisphere. It was completed on 30th May, 2008 consisting in an array of twelve independent and flexible lines placed into the Maditerranean Sea water. The detector design is optimized to detect high energy neutrinos from $100\,GeV$ to $1\,PeV$. The telescope is able to explore the Southern sky hemisphere, which represents the most interesting area of the sky due to the presence of the Galactic Centre, where neutrino source candidates are expected. The largest backgroud source for the cosmic neutrino detection is represented by *atmospheric muons*, particles created mainly as a consequence of the decay of π and K mesons originated by the interaction of CRs with atmospheric nuclei. In order to reject signals due to downward going atmospheric muons the neutrino telescopes, at the contrary of usual optical telescopes, 'look downward' where only muons created by neutrinos are expected to come. Anyway atmospheric muons represent the most abundant signal in a Cherenkov telescope due to their high flux. They can represent a background source because they can be wrongly reconstructed as upward going particles mimicking muons from neutrino interactions. On the other hand they can be used to calibrate the detector and to check the validity of the theoric models. In this scenario it is very important for any Cherenkov neutrino telescope the knowledge of the underwater μ flux in order to understand the detector response and possible systematic effects.

The aim of the analysis is the computation of the vertical component of the atmospheric muon flux as a function of the sea depth (also referred to as "Depth Intensity Relation", DIR). The analysis presented in this thesis has been performed on the experimental data of June and July 2007 when the ANTARES detector was in its five

7. SUMMARY AND CONCLUSIONS

lines configuration.

A MonteCarlo simulation of the atmospheric muon flux has been performed. Through the MonteCarlo some quantity related to the computation of the DIR have been calculated:

- The fraction of triggered events with respect to the number of MonteCarlo generated events as a function of the MonteCarlo true zenith angle. This quantity depends on the area of the cylinder (CAN) on which the MonteCarlo events are generated and on the sea depth at which the cylinder is placed. With the used CAN (height $H = 585\,m$, ray $R = 511\,m$, depth of sea bed $h_0 = 2475$) this quantity ranges from $1.3 \cdot 10^{-3}$ for almost vertical downward going muons to $3.4 \cdot 10^{-3}$ for almost horizontal muons.

- The 5 lines ANTARES effective area for atmospheric muons as a function of the generated zenith angle. This quantity represents the area of an ideal detector with a 100% probability to detect a muon which crosses it. This quantity is directly related to the mentioned above and it ranges from $1300\,m^2$ for almost vertical downward going muons to $2400\,m^2$ for almost horizontal muons.

The most important physics quantity for the aim of this thesis is the muon zenith angle. In the further analysis information on zenith angle related to the detected events is needed. For such a purpose a tracking program is used which takes as input the hit-time correlation of the triggered events and gives as output several parameters associated to the reconstructed track.

The error of the zenith angle evaluated from the tracking program $\Delta\theta \equiv \theta_m - \theta_t$ (where θ_m is the reconstructed zenith angle and θ_m the generated one) has been calculated with a MonteCarlo simulation. Defining the purity of the MonteCarlo data set as the fraction of events with an error on the zenith reconstruction less than 5°, the purity of the MonteCarlo data set is found to be 62.36%. In order to improve the purity some quality parameters of the tracking program have been studied. These parameters (defined in sec. 4.7) have been used to select a subset of data with a higher purity concerning the zenith angle reconstruction (see sec. 5.2.1). Before applying the selections based on these quality parameters, the data sample has been divided into two subset: single line (SL) events, when the hits used in the track fit belong to only one line and multiple line events (ML), when the hits belong to more than one line. The fraction of SL events is about 52% for real data and 48% for MonteCarlo data. The possible cause of such a difference can be due to some not well reproduced

feature in the background simulation. The noise is added to the MonteCarlo events by using the real background taken by a well defined real run. The run is chosen with similar background conditions to those of the real data set considered in the analysis. Despite that the data set covers a time range of two months and during this period some slight change in the noise conditions could be happened which can not be reproduced in the MonteCarlo. Different quality cuts have been defined for any data subset (SL and ML). The remaining MonteCarlo data set has an improved purity equal to 78.10%. The MonteCarlo events remaining after the selection represents a 53% over the whole reconstructed events, while for the real data the fraction is slightly lower, 49.67%. This discrepancy is mostly due to the quality cut which requires that the number of ANTARES storeys containing hits used in the track fit is greater than five ($Nstoreys > 5$). The possible cause of the difference has still to be determined by the background simulation as mentioned above.

The unfolding procedure of the real data is sensitive to the ratio between the number of MonteCarlo and real reconstructed events N^{MC}/N^{real} considered in the analysis. A change in this ratio will affect also the result. In order to quantify this effect the analysis has been done in parallel both with the selected data sample and with the whole reconstructed events. Although the final result is referred to the analysis performed with the only events selected by the quality cuts, the difference with the result obtained considering all the reconstructed events has been considered as a source of systematic uncertainties.

After the data selection the "response matrix", necessary fot the further analysis have been computed through the MonteCarlo.
The response matrix **R** has the dimension $M \times T$, where $M = 40$ is the number of bins related to the distribution of the reconstructed zenith angle, while $T = 18$ is the number of bins related to the MonteCarlo true zenith angle θ_t. Due to the reconstruction errors the range of the zenith angle evaluated by the tracking program θ_m is wider with respect to that of the generated one ($M > T$). θ_t in fact ranges from -1 to -0.1 while θ_m from -1 to 1. The element R_{ij} of the matrix contains the probability to observe an event, generated with a zenith angle belonging to the bin j, in the zenith bin i.

Such a matrix have been implemented into an unfolding algorithm based on a Bayesian approach which uses an iterative method. With this method it has been possible to retrieve back the flux of atmospheric muons with $E_\mu > 20\,GeV$ at the

fixed sea depth $h_0 = 1890\,m$ from the experimental data sample considered. The flux ranges from $10^{-7}\,cm^{-2} \cdot s^{-1} \cdot sr^{-1}$ for almost vertical downward going muons to $7 \cdot 10^{-12}\,cm^{-2} \cdot s^{-1} \cdot sr^{-1}$ for almost horizontal muons.

Using the relation 6.1 the experimental DIR was finally obtained. The results ranges from $10^{-7}\,cm^{-2} \cdot s^{-1} \cdot sr^{-1}$ at $2000\,m$ depth to $3 \cdot 10^{-10}\,cm^{-2} \cdot s^{-1} \cdot sr^{-1}$ at $6800\,m$ depth.

The systematic errors are finally estimated taking into consideration the uncertainties on several input parameters required to define the environmental and geometrical characteristics of the detector in the MonteCarlo simulation: absorption lenght of sea water, PhotoMultiplayer tube efficiency. From [118] a 30% of systematic uncertainties are stimated. In addition the systematics due to the cuts performed on the data set have been estimated. They range from 1% at $2000\,m$ depth to about 30% at $6800\,m$ depth. This uncertainties are added in quadrature to the 30% mentioned above to get the final systematic uncertainties.

The result is in good agreement with the previous indipendent analysis performed inside the ANTARES collaboration.

Bibliography

[1] E. Fermi. *On the origin of cosmic rays.* Phys. Rev., 75 (1949), 1169.

[2] E. Fermi. *Galactic magnetic fields and the origin of cosmic radiation.* Astrophys.J., 119 (19541), 6.

[3] V. L. Ginzburg and V. S. Ptuskin. *On the origin of cosmic rays: Some problems in high-energy astrophysics.* Rev. Mod. Phys., 48 (1976), 161.

[4] A. M. Hillas. *Can diffusive shock acceleration in supernova remnants account for high-energy galactic cosmic rays.* J. Phys. G: Nucl. Part. Phys., 31 (2005), 39.

[5] V.L. Ginzburg, Y.M. Khazan and V.S. Ptuskin. Astrophysics and Space Science 68 (1980), 295.

[6] J. R. Horandel. *Models of the knee in the energy spectrum of cosmic rays.* Astropart. Phys., 21 (2004), 241. astro-ph/0402356.

[7] A. M. Hillas. *In Cosmology, galaxy formation and astroparticle physics on the pathway to the SKA*, Oxford, United Kingdom, 2006. astro-ph/0607109.

[8] D. Kazanas and A. Nicolaidis. In Proceedings of the 27th International Cosmic Ray Conference, Hamburg, Germany, 2001. astro-ph/0103147.

[9] F. Halzen et al. *The highest energy cosmic ray. Astropart.* Phys., 3 (1995), 151.

[10] B. Peters. *Primary cosmic radiation and extensive air showers.* Nuovo Cimento, 22 (1961), 800.

[11] P. Sokolsky: *Introduction to Ultrahigh Energy Cosmic Ray Physics*, Westview Press Advanced Book Program, 2004.

[12] See the web site of the Pierre Auger observatory: http://www.auger.org/

[13] K. Greisen. *End to the cosmic ray spectrum?*. Phys. Rev. Lett., 16 (1966), 748.

[14] G. T. Zatsepin and V. A. Kuzmin. *Upper limit of the spectrum of cosmic rays.* Sov. Phys. JETP Lett., 4 (1966), 78.

[15] V. Berezinsky et al. *Astrophysics of Cosmic Rays*, North-Holland, Amsterdam (1990).

[16] C. Stegmann , A. Kappes, J. Hinton and F. Aharonian, *Potential neutrino signals in a northern hemisphere neutrino telescope from galactic gamma-ray sources*, Astrophysics and Space Science 309 (2007), 429.

[17] C. E. Fichtel and J. I. Trombka. *Gamma-ray astrophysics: New insight into the Universe.* Technical report, 1997. NASA-RP-1386.

[18] see the web site of the Fermi Gamma-ray Space Telescope: http://fermi.gsfc.nasa.gov/

[19] F. Arqueros et al., Astron. Astrophys. 359 (2000), 682.

[20] J. Holder et al. In Proceedings of the 29th International Cosmic Ray Conference, Pune, India, 2005. astro-ph/0507451.

[21] R. Enomoto et al. *Design study of CANGAROO-III, stereoscopic imaging Cherenkov telescopes for sub-TeV gamma-ray.* Astropart. Phys., 16 (2002), 235.

[22] J. A. Hinton. *The status of the HESS project.* New Astron. Rev., 48 (2004), 331.

[23] J. Albert et al., *Physics and Astrophysics with a ground-based gamma-ray telescope of low energy threshold Astroparticle Physics*, 23 (2005), 493.

[24] M. D. Kistler and J. F. Beacom. *Guaranteed and prospective galactic TeV neutrino sources.* Phys. Rev. D, 74 (2006), 063007. astro-ph/0607082.

[25] D. Horns, F. Aharonian, A. Santangelo, A. I. D. Hoffmann, and C. Masterson. *Nucleonic gamma-ray production in Vela X.* Astron. & Astrophys., 451 (2006), L51.

[26] D. Guetta and E. Amato. *Neutrino flux predictions for galactic plerions.* Astropart. Phys., 19 (2003), 403. astro-ph/0209537.

[27] F. Aharonian et al. (HESS Collaboration). *Very high energy gamma rays from the direction of Sagittarius A**. Astron. & Astrophys., 425 (2004), L13.

[28] F. Aharonian et al. (HESS Collaboration). *Very high energy gamma rays from the composite SNR G0.9+0.1*. Astron. & Astrophys., 432 (2005), L25.

[29] E. Waxman. *Extra galactic sources of high energy neutrinos*. Phys. Scripta, T121 (2005), 147. astro-ph/0502159.

[30] F. Aharonian et al., H.E.S.S. collaboration. Nature, 440 (2006), 1018.

[31] R. White, Proc. 30th International Cosmic Ray Conference, Merida, 2007.

[32] T. J. Galama et al. *Discovery of the peculiar supernova 1998bw in the error box of GRB980425*. Nature, 395 (1998), 670.

[33] K. Z. Stanek et al. *Spectroscopic discovery of the supernova 2003dh associated with GRB030329*. Astrophys. J., 591 (2003.), L17.

[34] J. Hjorth et al. *A very energetic supernova associated with the gamma-ray burst of 29 March 2003*. Nature, 423 (2003), 847.

[35] E. Waxman and J. N. Bahcall. *High energy neutrinos from cosmological gamma-ray burst fireballs*. Phys. Rev. Lett., 78 (1997), 2292.

[36] D. Guetta et al. *Neutrinos from individual gamma-ray bursts in the BATSE catalog*. Astropart. Phys., 20 (2004), 429. astro-ph/0302524.

[37] H. Dannerbauer et al. *Follow-up near-infrared spectroscopy of ultraluminous infrared galaxies observed by ISO*. Astron. & Astrophys., 441 (2005) 999.

[38] V. Springel et al. *Modeling feedback from stars and black holes in galaxy mergers*. Astron. Soc., 361 (2005), 776.

[39] A. Loeb and E. Waxman. *The cumulative background of high-energy neutrinos from starburst galaxies*. JCAP, 0605 (2006), 003. astro-ph/0601695.

[40] Carlo Giunti, *Neutrino Flavor States and the Quantum Theory of Neutrino Oscillations*. J. Phys. G: Nucl. Part. Phys. 34 (2007) R93-R109, arXiv:hep-ph/0608070. See also the very interesting and exhaustive web page on neutrinos: http://www.nu.to.infn.it/

[41] M.A. Markov, Proceedings Int. Conf. on High Energy Physics, Univ. of Rochester, (1960) 183.

[42] J. Pumplin et al. *New generation of parton distributions with uncertainties from global QCD analysis.* JHEP, 07 (2002), 012. hep-ph/0201195.

[43] W.M.Yao et al. (Particle Data Group), J. Phys. G 33, 1 (2006) and 2007 partial update for the 2008 edition.

[44] K. Greisen. Ann. Rev. Nucl. Science, 10 (1960), 63.

[45] V. Agrawal et al., Phys. Rev. D53 (1996), 1314.

[46] P. Bosetti et al., DUMAND collaboration. Harvard, HDC-2-88 (1988). Astropart.Phys., 7 (1997), 263.

[47] The Baikal Collaboration. *The Baikal neutrino project: Status report.* Nucl. Phys. B (Proc. Suppl.), 91 (2001), 438.

[48] M. P. Kowalski. In Proceedings of the 28th International Cosmic Ray Conference, Tsukuba, Japan, 2003.

[49] IceCube Collaboration. In Proceedings of the 29th International Cosmic Ray Conference, Pune, India, 2005. astro-ph/0509330.

[50] E. Andres et al. AMANDA Collaboration. Nature 410 (2001).

[51] The IceCube Collaboration. *IceCube: A kilometer scale neutrino observatory.* NSF Proposal, 2001. http://pheno.physics.wisc.edu/IceCube/proposal.html.

[52] see http://www.km3net.org

[53] P. Piattelli (NEMO collaboration). Nucl.Phys.Proc.Suppl. 143 (2005), 359.

[54] G. Aggouras et al. (NESTOR collaboration). Astropart.Phys. 23 (2005), 377.

[55] J.A. Aguilar et al. (ANTARES Collaboration). Astropart.Phys. 26 (2006), 314.

[56] Y. Becherini, A. Margiotta, M. Sioli and M. Spurio, Astrop. Phys. 25 (2006), 1.

[57] G.Carminati et al., *Atmospheric MUons from PArametric formulas: a fast GEnerator for neutrino telescopes (MUPAGE)*, Comput. Phys. Commun., 179 (2008), 915.

[58] T.S. Sinegevskays, S.I. Sinegovsky, Phys. Rev. D63 (2001), 096004.

[59] C. Forti *et al.*, Phys. Rev. D42 (1990) 3668.

[60] E. Scapparone et al., arXiv: physics/9902043.

[61] J.Ranft, Phys. Rev. D51 (1995), 64; arXiv:hep-ph/0002137.

[62] M. Ambrosio et al. (The MACRO Collaboration), Phys. Rev. D56 (1997), 1407.

[63] B. Wiebel-Soth et al, Astron. Astrophys. 330 (1998), 389.

[64] S.I. Nikolsky et al., Soviet Phys. JETP, 60 (1984), 193.

[65] J.R. Hoerandel, Astropart. Phys. 19 (2003), 193.

[66] S. Muraro, *The calculation of atmospheric muon flux using the FLUKA Monte Carlo code*, PhD. Thesis, Milano University, 2006.

[67] T.K. Gaisser et al., Proc. 27th ICRC (Hamburg, 2001), 1643.

[68] A.D. Panov et al., Bull. Rus. Acad. Sci.: phys. 71 (2007) 494; arXiv:astro-ph/0612374v1.

[69] V.A. Debrina et al., ApJ 628 (2005) L41.

[70] T. Antoni et al., Astropart. Phys. 24 (2005) 1; Roth M. and Ulrich H, Proc. 28 ICRC (Tsukuba 2003) 1, 139.

[71] T. Antoni et al., ApJ 612 (2004) 914.

[72] D.B. Kieda & S.P. Swordy, proc. 26 ICRC (Salt Lake City, 1999) 3, 191; D.B. Kieda & S.P. Swordy, Astropart. Phys. 13 (2000), 137.

[73] J.W. Fowler et al., Astropart. Phys. 15 (2001), 49.

[74] D. Chernov et al., Int. J. Mod. Phys. A20 (2006) 6799; Prosin V.V. 21 ECRS (Kosice, 2008).

[75] N.M. Budnev et al., arXiv:astro-ph/0511215

[76] H. Tanaka et al., Proc. 29 ICRC (Pune, 2005) 6, 209.

[77] S. Ogio et al., Astrophys. J., 612 (2004) 268; Y. Shirasaki et al., Astropart. Phys. 15 (2001), 357.

[78] M. Nagano et al., J. Phys. G: Nucl. Phys. 10 (1984), 1295.

[79] M. Amenomori et al., arXiv:0801,1803v1 [hep-ex]; M. Amenomori et al., Phys. Rev. D62 (2000) 112002.

[80] M. Ambrosio et al., Phys. Rev. D52 (1995), 3793.

[81] Aglietta et al., heo-ph/9806001.

[82] Bakatanov et al., Sov. J. Nucl. Phys. 55 (1992), 1169.

[83] Zatsepin et al., Isv. Ross. Akad. Nauk. Sez. Fiz. 58 (1994), 119.

[84] P. Lipari, Astropart. Phys. 1(2) (1995), 195.

[85] P. Antonioli et al., Astropart. Phys. 7 (1997), 357.

[86] M. Ambrosio et al. (The MACRO Collaboration), Phys. Rev. D60 (1999), 032001.

[87] G. Battistoni et al., Astropart. Phys. 3 (1995), 157. INFN/AE-99/07 (1999).

[88] Stanev T., High Energy Cosmic Rays, (Springer Verlag, Berlin, 2003).

[89] E.V. Bugaev et al., hep-ph/9803488v3.

[90] Bobson J. et al., Phys. Rev. D42 (1990), 3613.

[91] Belolaptikov I.A. et al., Proc.23rd ICRC (Calgary, 1993) vol.4, 573.

[92] Belolaptikov I.A. et al., Astropart. Phys. 7 (1997), 263.

[93] Andres E. et al., Astropart. Phys. 13 (2000), 1.

[94] Anassontzis E.G. et al., Proc.23rd ICRC (Calgary, 1993) vol.4, 554.

[95] P. Desiati et al. for AMANDA Coll., Proc. 28th ICRC (Tsukuba, 2003) 1373.

[96] R. Bruijn, *The Antares Neutrino Telescope: Performance Studies and Analysis of First Data.* PhD thesis, Universiteit van Amsterdam, Netherlands, 2008.

[97] P. A. Cherenkov. Phys. Rev., 52 (1937), 378.

[98] For more informations and for a complete list of the ANTARES members see: http://antares.in2p3.fr

[99] P. Amram et al. *Background light in potential sites for the ANTARES undersea neutrino telescope.*, Astropart. Phys., 13 (2000), 127. astro-ph/9910170.

[100] J. A. Aguilar et al. The ANTARES optical module. Nucl. Instr. and Meth. Phys. Res. A, 555:132141, 2005.

[101] P. Amram et al., Nucl. Instr. and Methods A484 (2002), 369.

[102] J. A. Aguilar. *Study of the performances of several layouts and geometries for the future ANTARES neutrino telescope.* Masters thesis, Universitat de Valencia, Spain, 2004.

[103] J. A. Aguilar et al. *Transmission of light in deep sea water at the site of the ANTARES neutrino telescope.* Astropart. Phys., 23 (2004), 131. astroph/0412126.

[104] G de Vries-Uiterweerd, *Signal and Background in the Underwater Neutrino Telesccope ANTARES.* PhD thesis, Universiteit Utrecht, Netherlands, 2007.

[105] J.A. Aguilar et al. (The ANTARES Coll.), *The data acquisition system for the ANTARES neutrino telescope.* Nucl. Instr. and Methods A570 (2007), 107.

[106] A. Romeyer. *Etude de la sensibilite du detecteur ANTARES a un flux diffus de neutrinos cosmiques de haute energie.* PhD thesis, Universite Denis Diderot - Paris VII, France, 2003.

[107] M. Ageron et al., Nucl. Instr. and Methods A578 (2007), 498.

[108] See The ROOT System Home Page: http://root.cern.ch/

[109] J. Brunner, *Antares simulation tools, Prepared for VLVnT Workshop on Technical Aspects of a Very Large Volume Neutrino Telescope in the Mediterrenean Sea,* Amsterdam, The Netherlands, 5-8 Oct 2003. http://www.vlvnt.nl/proceedings/

BIBLIOGRAPHY

[110] N.N.Kalmykov, S.S.Ostapchenko, A.I.Pavlov, Nucl. Phys. B (Proc. Suppl.) 52B (1997), 17.

[111] *GEANT Detector Description and Simulation Tool*, CERN Program Library.

[112] F. Cassol, *GENDET 1.0: A program to generate detector files*, ANTARES-Soft/1999-007.

[113] M. de Jong, *The ANTARES trigger software*, ANTARES-Soft/2005-005.

[114] http://marwww.in2p3.fr/brunner/BBdisp

[115] J. Carr, D. Dornic, S.Escoffier, F. Jouvenot, G.Maurin, *MRECO: a reconstruction code robust in high levels of light backgrounds. 1) Application to Monte-Carlo*, ANTARES Internal Note ANTARES-SOFT-2007-012.

[116] T. K. Gaisser, *Cosmic Rays and Particle Physics*, Cambridge University Press, (1990).

[117] G. D'Agostini, NIM A **362** (1995) 487; see also G. D'Agostini, Comments on the Bayesian unfolding, Zeus Note 95-166 (1995).

[118] A. Margiotta, *Systematic uncertainties in MonteCarlo simulations of the atmosphericmuon flux in the 5-line ANTARES detector*, arXiv:0809.0268v1 [astro-ph].